POLITECNICO
MILANO 1863

SCUOLA DI INGEGNERIA INDUSTRIALE
E DELL'INFORMAZIONE

Label-Free and High-Speed Biomedical Imaging through Colocalized SHG and Broadband CARS Microscopy

Master's Thesis in
Physics Engineering

Author: **Claudio Cavecchi**

Student ID: 988077
Advisor: Prof. Dario Polli
Co-advisors: Dr. Federico Vernuccio
Academic Year: 2022-2023

Abstract

Coherent Anti-Stokes Raman Scattering (CARS) microscopy is a label-free vibrational imaging technique for delivering chemical maps of cells and tissues. Spontaneous Raman (SR), the gold standard for vibrational spectroscopy, offers high chemical specificity but suffers from low scattering cross-section, hampering imaging speed. CARS overcomes this limitation by exploiting the third-order non-linear optical response of the sample. In its basic form, CARS employs synchronized picosecond laser pulse trains (pump and Stokes) focused on the sample plane. Matching the frequency difference between the two beams to a vibrational mode of the sample coherently excites molecules, and a second interaction with the pump generates a stronger anti-Stokes signal compared to SR. However, this configuration reveals only one vibrational mode at a time. Broadband CARS (BCARS) addresses this by combining narrowband pump pulses with broadband Stokes pulses, enabling the recording of broad vibrational spectra. This combines the acquisition speed of single-frequency CARS with the chemical specificity of SR. Another technique is Second Harmonic Generation (SHG) microscopy, in which two photons are transformed into a frequency exactly twice the incident frequency. This technique is primarily employed for visualizing structures rich in collagen.

The thesis focuses on utilizing and improving a BCARS setup to convert it into a versatile multimodal microscope. Chapter 1 elaborates on CARS and SHG microscopy derivations. Chapter 2 describes the BCARS setup used for my thesis, discussing the improvements that I implemented to transform it into a multimodal microscope capable of simultaneously acquiring BCARS and SHG signals. Chapter 3 examines the acquisition and post-processing pipeline for CARS spectroscopy and imaging. Chapter 4 presents experimental outcomes. I first analyze solvents and subcellular components spectra. Then, I employ PCA on various tumor cell lines and I make BCARS imaging on a NASH liver slice. Lastly, I exhibit microcalcification images in breast tissue, obtained via simultaneous BCARS and SHG acquisition, highlighting the potential of my multimodal microscope.

Keywords: Broadband CARS, microscopy, spectroscopy, label-free, High-speed imaging, SHG, multiphoton microscopy

Abstract in lingua italiana

La microscopia Coherent Anti-Stokes Raman Scattering (CARS) è una tecnica di imaging vibrazionale senza etichettatura per la mappatura chimica di cellule e tessuti. La Spettroscopia Raman Spontaneo (SR), standard per la spettroscopia vibrazionale, ha alta specificità chimica ma bassa sezione d'urto di scattering e bassa velocità di acquisizione. Il CARS sfrutta la risposta ottica non lineare di terzo ordine del campione, superando questa limitazione. Nel caso base, il CARS utilizza impulsi laser al picosecondo sincronizzati (pompa e Stokes) focalizzati sul campione. Quando la differenza di frequenza tra i due fasci coincide con un modo vibrazionale del campione, le molecole vengono eccitate in modo coerente, generando un segnale anti-Stokes più forte rispetto a quello ottenuto con il SR. Tuttavia, questa configurazione rivela solo un modo vibrazionale alla volta. Il CARS a banda larga (BCARS) affronta questo limite combinando impulsi di pompa a banda stretta con impulsi di Stokes a banda larga, permettendo la registrazione di ampi spettri vibrazionali, unendo la velocità di acquisizione del CARS a singola frequenza con la specificità chimica del SR.
Un'altra tecnica è la microscopia SHG, in cui due fotoni si convertono in una frequenza doppia rispetto a quella incidente, utilizzata principalmente per visualizzare strutture ricche di collagene.
La tesi si focalizza sull'utilizzo e sull'ottimizzazione di un setup BCARS per creare un microscopio multimodale. Il Capitolo 1 introduce i principi della microscopia CARS e SHG. Il Capitolo 2 descrive il setup utilizzato, discutendo le modifiche apportate per l'acquisizione simultanea di segnali BCARS e SHG. Il Capitolo 3 esamina il processo di acquisizione e di post-processing per l'analisi dei dati CARS. Il Capitolo 4 presenta i risultati sperimentali, inclusa l'analisi degli spettri dei solventi e dei componenti subcellulari, l'applicazione della PCA a diverse linee cellulari tumorali, immagini BCARS su sezioni di fegato affetto da NASH e immagini di microcalcificazioni nel tessuto mammario ottenute tramite acquisizione simultanea di segnali BCARS e SHG, mettendo in luce il potenziale del microscopio multimodale.
Parole chiave: CARS a banda larga, microscopia, spectroscopia, senza etichetta, Imaging ad alta velocità, SHG, microscopic multifotone

Contents

Introduction

Optical microscopy is a valuable and versatile investigation tool for visualizing morphological details in cells and tissues at the sub-micrometer scale [1]. It offers a much higher spatial resolution compared to magnetic resonance imaging (MRI) and at the same time, it avoids the need for sample fixation, as in electron microscopy. Among optical microscopy techniques, fluorescence microscopy is particularly useful for achieving high sensitivity down to the single molecule limit using either exogenous (dyes or semiconductor quantum dots [2]) or endogenous (GFPs and fluorescent protein [3]) markers. However, this technique presents several problems and limitations that should be considered. For certain types of cells and tissues, adding fluorescent markers can be challenging or even impossible. Furthermore, adding markers can significantly perturb the system under investigation. In the case of small molecules such as signaling peptides, neurotransmitter metabolites, and drugs, the dimension of the marker is comparable to or even bigger than that of the molecule itself, interfering with its biological function. Another problem is that cells are susceptible to phototoxicity which is further enhanced by reactive chemical species generated by the fluorescent molecule under illumination. Moreover, photobleaching may prevent the possibility of imaging many times the same portion of the sample. Finally, staining live tissue with fluorophores may not be feasible or desired in many clinical applications. These limitations call for alternative techniques that are label-free and non-destructive.

Vibrational microscopy is a valuable imaging technique that overcomes some of the limitations of fluorescence microscopy. In vibrational microscopy, every component of a biological sample has a unique vibrational spectrum that reflects its molecular structure and provides a chemically specific signature that can be exploited for its identification [4]. This endogenous property of biological samples makes vibrational microscopy a powerful tool for studying their chemical composition and structure without the need for exogenous markers and in a label-free manner. One type of vibrational microscopy is vibrational absorption microscopy [5], which measures the absorption or reflection of mid-infrared (MIR) light by a sample to generate an image based on its chemical composition. However, long wavelengths of mid-infrared light can limit the spatial resolution, due to diffraction, and

penetration depth, due to water absorption. Therefore, vibrational absorption microscopy is not suitable for imaging small structures in biological samples. Raman microscopy offers a solution to the challenges, as it employs visible or near-infrared (NIR) light, resulting in much higher penetration depth and spatial resolution. This makes Raman techniques particularly suitable for imaging biological samples, such as tissues and cells [6, 7]. One such Raman technique is Spontaneous Raman (SR) [8], which utilizes an incoming quasi-monochromatic laser light at frequency ω_p (pump frequency) to excite the molecule to a virtual state. The molecule relaxes to the ground state, emitting a photon with energy at frequency ω_s (stokes frequency) or ω_{as} (anti-stokes frequency). When the sample is illuminated, the photon can collide with the vibration of the sample, giving rise to an inelastic scatter that can increase or decrease the energy of the photon. The vibrational information is encoded in the spontaneously emitted inelastically scattered Stokes or anti-Stokes components, at frequency $\omega_s = \omega_p + \Omega$ and $\omega_{as} = \omega_p - \Omega$, respectively, with Ω being the vibrational resonance of the sample. In life sciences applications, SR techniques typically acquire the Stokes component, which is more intense than the anti-Stokes one at room temperature. This phenomenon arises from the underpopulated vibrational levels of the sample, thereby reducing the likelihood of anti-Stokes emission. Thanks to its chemical specificity, SR is able to identify selectively many types of biomolecules in human tissue and cells [7, 8], and also it is able to provide a clear distinction between states of a dynamical process. For instance, SR can detect biochemical differences in irradiated cells and discriminate between normal and cancerous states for skin, bladder and gastric tissues, rat fibroblast cells, human bone, and human epithelial cells from a variety of organs. [9, 10].

A typical Raman spectrum displays two main vibrational intervals that are important for identifying specific molecular signatures. An example of this is seen in the figure 1 taken from [11], which shows the SR spectrum of a P22 virus in H_2O buffer obtained by irradiation at 514.5 nm with an Ar-ion laser [12]. The first interval, important for chemical identification, is the fingerprint region, which is located in the low wavenumber portion of the spectrum (600-1800 cm^{-1}). This region contains contributions from lipids, proteins, and nucleic acids, and the vibrations are associated with the stretching or deformation of carbon atoms bonded with nitrogen (C-N stretch), hydrogen (C-H rock, bend or scissoring), or other carbon atoms (C-C stretch). The peaks associated with lipids are those such as those at 1300 cm^{-1} for CH_2 bonds and around 1440-1450 cm^{-1} for CH and CH_2 modes. Double bonds like C=N, C=O, and C=C can be typically monitored in 1500–1800 cm^{-1} frequency interval. The second region of interest is the high wavenumber window (2700-3100 cm^{-1}), where the Raman spectrum is dominated by broad features related to the stretching of hydrogen bonds (C-H, N-H, O-H). This region is often used

to study long-chain hydrocarbons and lipids, such as fats, waxes, sterols, mono-, di-, and triglycerides, phospholipids, and fat-soluble vitamins. Water produces a very broad and intense peak for wavenumber longer than 3100 cm^{-1}. Additionally, there is a region of the spectrum known as the Raman-biological silent region, which spans from 1800 to 2700 cm^{-1} and has no peaks. This region is useful when using Raman-tag molecules that provide specific signals with characteristic peaks in the silent region, which do not interfere with the signals from biological constituents [13, 14]. As evidenced by numerous biomedical applications, SR has proven particularly useful in cancer diagnosis [15, 16]. However, SR microscopy has some limitations. Specifically, its low scattering cross-section necessitates a long integration time for acquiring the spectrum of a single pixel from 100 ms to several seconds, resulting in extended image acquisition times precluding fast imaging. Additionally, distinguishing the weak inelastically scattered SR light from fluorescence is challenging, resulting in a broad baseline that must be subtracted.

The limitations of SR can be surpassed by using coherent Raman scattering (CRS) techniques [17, 18], which are a type of third-order nonlinear optical microscopy. CRS utilizes light pulses to create and detect a vibrational coherence within the molecules in the laser focus. By using a combination of two synchronized pulses, the pump at frequency ω_p and the Stokes at frequency ω_s, collective molecular oscillation is induced resulting in all molecules vibrating in phase when the difference between pump and Stokes frequencies matches a characteristic vibrational frequency gamma, that is, $\omega_p - \omega_s = \Omega$ [19, 20]. This vibrational coherence enhances the Raman response significantly compared to the incoherent SR process. Additionally, the CRS signal is emitted in a coherent beam, propagating in a direction satisfying a phase-matching condition for the CRS process. CRS microscopy, nowadays, is a widely used technique due to its numerous advantages over other methods. Firstly, it is a label-free technique, meaning it does not require the use of fluorophores or staining, allowing for the study of cells and tissues without alteration. Additionally, photobleaching and damage to biological samples are minimized as CRS works out of resonance, without population transfer into electronically excited states of the molecule. Compared to SR microscopy, CRS exploits a coherent superposition of the vibrational responses, providing a considerably stronger signal and allowing for higher imaging speeds. Similar to multi-photon fluorescence microscopy [21], CRS is a nonlinear microscopy technique that generates signal only in the focal volume, exhibiting 3D sectioning capability without the need for any physical confocal apertures [22]. Excitation in the near-infrared range (700-1200 nm) also provides an advantage in reducing light absorption and scattering by turbid media, allowing for high penetration depth through thick tissues. Furthermore, pushing the wavelength of the beams toward the infrared has the additional benefit of reducing phototoxicity and tissue damage, as it could happen,

for example, in DNA via multi-photon absorption (resonant at 260 nm). The two most commonly employed CRS implementations are stimulated Raman scattering (SRS) [23–25] and coherent anti-Stokes Raman scattering (CARS) [26–28].

An important microscopy technique is Second Harmonic Generation (SHG) microscopy. This technique has emerged as a potent nonlinear optical contrast mechanism, finding applications in both biological and biophysical imaging realms [29]. SHG is a coherent process in which two lower-energy photons harmonize to yield a frequency twice that of the incident light (or half the wavelength).

SHG microscopy proves particularly advantageous for in situ tissue imaging. Its endogenous contrast stems solely from intrinsic constituents within the sample, eliminating the need for dyes or fluorophores. Additionally, the reduced susceptibility of SHG to photobleaching and phototoxicity in comparison to fluorescence methods bolsters its appeal. The efficacy of this technique is further underscored by its capacity for high-resolution, deep-tissue imaging to depths of several hundred microns, facilitated by near-infrared laser fundamental wavelengths [30].

The inherent sensitivity of SHG to physical structure, coupled with its remarkable capacity for optical sectioning, equips it to achieve 3D imaging of bulk tissue with heightened sensitivity and specificity [31]. Nevertheless, it's important to note that SHG signal acquisition necessitates a non-centrosymmetric structure at a scale commensurate with the SHG wavelength. This requirement underscores the remarkable sensitivity of SHG to collagen architecture within the sample. While this limitation constrains the range of applicability for SHG, its unique attributes make it an indispensable tool for specific structural investigations.

This thesis presents the significant outcomes I attained during the period spanning February to October 2023 at the VIBRA lab of Politecnico di Milano, under the guidance of Professor Dario Polli.

My primary achievement involves the enhancement of an already existing BCARS setup, transforming it into a multimodal microscope with the capability to concurrently capture both BCARS and SHG signals. Notably, I undertook modifications to the experimental configuration and developed the requisite Matlab code for proficient data acquisition and denoising.

In Chapter 1, a comprehensive exploration of linear and non-linear optics, alongside the coherent Raman scattering processes and Second Harmonic Generation, is presented. Building a strong theoretical foundation, this chapter delves into the core principles underlying these optical phenomena.

Moving forward, Chapter 2 describes the BCARS experimental setup, detailing the modifications I implemented to convert it into a multimodal system. The architectural nuances

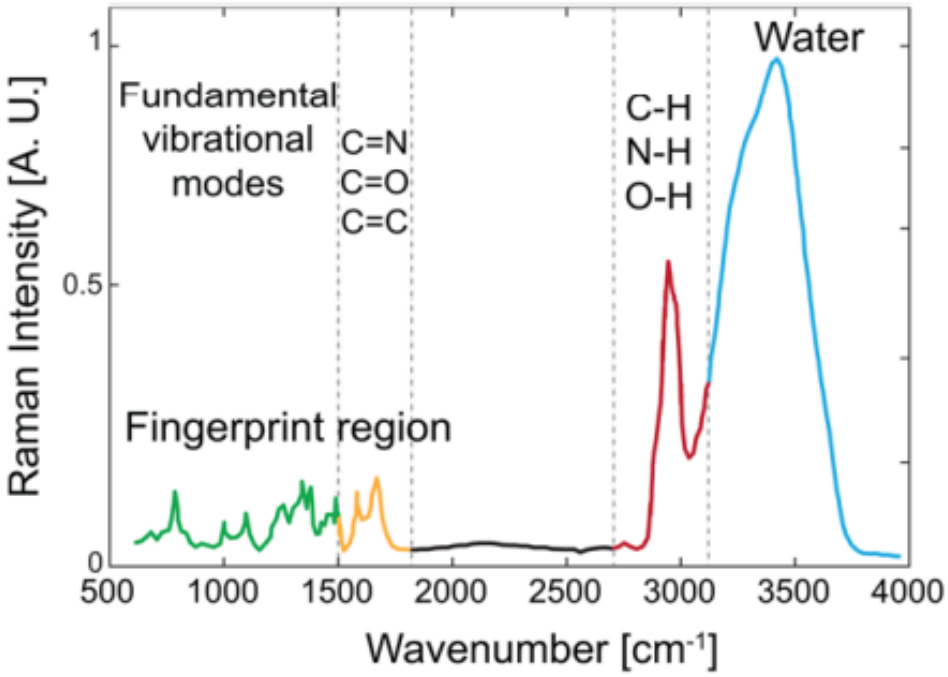

Figure 1: Stimulated Raman spectrum of P22 virus in H_2O buffer, highlighting most relevant vibrational transitions.From [11]

and design alterations are meticulously explained, underscoring the evolution of the capabilities of the setup.

Chapter 3 takes a closer look at the methodologies underpinning the acquisition and subsequent post-processing techniques employed for CARS spectroscopy and imaging. Shifting the focus to Chapter 4, the spotlight is on the empirical outcomes harnessed through the BCARS experimental configuration. This chapter showcases a gamut of results, ranging from BCARS spectra of solvents and subcellular constituents to chemical mappings of biological samples like cells and tissues. Notably, it shows the remarkable potential unlocked through the synergy of BCARS and SHG, underscoring their symbiotic impact.

1 | Theory

This chapter presents the fundamental theory underlying the optical processes under investigation. The exposition starts with the derivation of the Maxwell equations which describe the propagation of pulses in linear media. Subsequently, the focus turns to non-linear optical processes, beginning with the second-order non-linear processes like second harmonic generation and proceeding up to the third-order non-linear optical processes. This includes a detailed discussion of the phenomenon of spontaneous Raman scattering and coherent Raman scattering, with particular emphasis on Coherent Anti-Stokes Raman Scattering (CARS).

1.1. Linear optics

1.1.1. Light propagation equation

Let's consider the Maxwell equations:

$$\begin{cases} \nabla \cdot \boldsymbol{D} = \rho, & \text{(1.1a)} \\ \nabla \times \boldsymbol{E} + \dfrac{\partial \boldsymbol{B}}{\partial t} = 0, & \text{(1.1b)} \\ \nabla \cdot \boldsymbol{B} = 0, & \text{(1.1c)} \\ \nabla \times \boldsymbol{H} - \dfrac{\partial \boldsymbol{D}}{\partial t} = \boldsymbol{J}. & \text{(1.1d)} \end{cases}$$

where $\boldsymbol{E}$ is the electric field, $\boldsymbol{H}$ is the magnetic field, $\boldsymbol{D}$ is the electric displacement field, $\boldsymbol{B}$ is the magnetic induction field, ρ is the net free charge density and $\boldsymbol{J}$ is the conduction current density. These equations couple the electric field and the magnetic field generating time-varying and propagating solutions. These equations, however, have to be completed using constitutive relations, which state a relation between the different fields:

$$\boldsymbol{D} = \epsilon_0 \boldsymbol{E} + \boldsymbol{P} \tag{1.2}$$

$$\boldsymbol{B} = \mu_0[\boldsymbol{H} + \boldsymbol{M}] \tag{1.3}$$

where $\boldsymbol{P}$ is the polarization vector, $\boldsymbol{M}$ is the magnetization vector and μ_0, ϵ_0 are, respectively, the magnetic permeability and electric permittivity in vacuum. The operator $\nabla\times$ can be applied to (1.1b):

$$\nabla \times (\nabla \times \boldsymbol{E} + \frac{\partial \boldsymbol{B}}{\partial t}) = 0 \tag{1.4}$$

Remembering now the following vector identity:

$$\nabla \times (\nabla \times \boldsymbol{E}) = \nabla(\nabla \cdot \boldsymbol{E}) - \nabla^2 \boldsymbol{E} \tag{1.5}$$

by applying (1.2) and the relation of the speed of light $\frac{1}{c^2} = \mu_0\epsilon_0$ to (1.4), we can obtain the propagation equation:

$$\nabla(\nabla \cdot \boldsymbol{E}) - \nabla^2 \boldsymbol{E} = -\mu_0 \frac{\partial(\nabla \times \boldsymbol{M})}{\partial t} - \mu_0 \frac{\partial \boldsymbol{J}}{\partial t} - \frac{1}{c^2}\frac{\partial^2 \boldsymbol{E}}{\partial t^2} - \mu_0 \frac{\partial^2 \boldsymbol{P}}{\partial t^2} \tag{1.6}$$

In optics, it is reasonable to make some assumptions:

1. Non-magnetic material: $\boldsymbol{M} \approx 0$
2. Neutral optical media. It means that we can assume the absence of free charge in the material: $\rho \approx 0$ resulting in $\nabla \cdot \boldsymbol{E} \approx 0$
3. Homogenous medium. So the refractive index does not show discontinuities, thus the polarization is not changing in a stepwise way over "short" distances: $\nabla \cdot \boldsymbol{P} \approx 0$
4. Negligible current density $\boldsymbol{J} \approx 0$

Under these assumptions, the propagation equation becomes:

$$\nabla^2 \boldsymbol{E} - \frac{1}{c^2}\frac{\partial^2 \boldsymbol{E}}{\partial t^2} = \mu_0 \frac{\partial^2 \boldsymbol{P}}{\partial t^2} \tag{1.7}$$

Then, we can consider the case of linear polarized light along the z-axis, $\boldsymbol{E} = E\hat{\boldsymbol{u}}_{\boldsymbol{z}}$, in an isotropic medium,$\boldsymbol{P} = P\hat{\boldsymbol{u}}_{\boldsymbol{z}}$. The scalar propagation equation becomes:

$$\nabla^2 E - \frac{1}{c^2}\frac{\partial^2 E}{\partial t^2} = \mu_0 \frac{\partial^2 P}{\partial t^2} \tag{1.8}$$

In the case of Plane Wave Approximation, the pulse is a plane wave, thus being a transverse wave with the electric field that is constant in a plane perpendicular to the direction of propagation z $E(\boldsymbol{r}, t) = E(z, t)$. We finally get the scalar wave propagation for planar

wave:

$$\frac{\partial^2 E}{\partial z^2} - \frac{1}{c^2}\frac{\partial^2 E}{\partial t^2} = \mu_0 \frac{\partial^2 P}{\partial t^2} \tag{1.9}$$

This equation describes the propagation of light in a medium. If this medium is vacuum, since the polarizability of the vacuum is identically equal to zero $P = 0$ the solution of this equation will be a light wave traveling at the speed of light. In a medium, on the other hand, the electric field of the light drives an electric dipole and this electric dipole will oscillate in time (as the electric field itself does), thus emitting light. This secondary field, emitted by the electric dipole, will interfere with the original incoming one, thus acting as a source term that can modify the temporal profile of the electric field (but not its frequency, in linear optics)

1.1.2. Polarization

By definition, polarization is the volume density of permanent or induced electric dipole moments in a dielectric.

$$\boldsymbol{P} \triangleq \frac{\partial \boldsymbol{p}}{\partial V} \tag{1.10}$$

Polarization is a fundamental property of dielectric materials that describes how they respond to an applied field. It quantifies the degree to which the material's electric charges are displaced from their equilibrium positions when an external electric field is applied. The physical meaning of polarization is crucial in understanding the behavior of dielectric materials. In addition to its response to an external electric field, polarization also plays a critical role in electromagnetic wave propagation. In the wave propagation equations, polarization is included on the right-hand side as a source term. This is because polarization acts as both a receiving and emitting antenna, influencing the behavior of electromagnetic waves passing through the material.
The polarization field $\boldsymbol{P}$ can be expressed as the sum of two terms: one that varies linearly with the applied electric field $\boldsymbol{P^{(l)}}$ and another that varies non-linearly with it $\boldsymbol{P^{(nl)}}$:

$$\boldsymbol{P} = \boldsymbol{P^{(l)}} + \boldsymbol{P^{(nl)}} \tag{1.11}$$

When the peak intensity of the pulse that is propagating in the medium is lower than $10^9 \frac{W}{cm^2}$, $\boldsymbol{P^{(nl)}}$ is negligible $\boldsymbol{P} \approx \boldsymbol{P^{(l)}}$. Then, the i-th component of the polarization can be written as:

$$P_i^{(l)}(\boldsymbol{r}, t) = \epsilon_0 \sum_j \int_{volumespace} d\boldsymbol{r'} \int_{-\infty}^{+\infty} \chi_{i,j}^{(1)}(\boldsymbol{r}, \boldsymbol{r'}, t, t') E_j(\boldsymbol{r'}, t) dt' \tag{1.12}$$

where $i, j = x, y, z$ and χ is the electric susceptibility. For isotropic, homogeneous, and time-invariant media the linear polarization can be written as:

$$\boldsymbol{P^{(l)}(r,t)} = \epsilon_0 \int_{-\infty}^{+\infty} \chi(t-t')\boldsymbol{E(r',}t)dt' = \epsilon_0 \int_{-\infty}^{+\infty} \chi(t')\boldsymbol{E(r',}t-t')dt' \tag{1.13}$$

When the peak intensity of the pulse that is propagating in the medium has a value between $10^9 \frac{W}{cm^2}$ and $10^{12} \frac{W}{cm^2}$, $\boldsymbol{P^{(nl)}}$ is not negligible anymore. In this case, the non-linear polarization can be written in power series:

$$\boldsymbol{P^{(nl)}} = \boldsymbol{P^{(2)}} + \boldsymbol{P^{(3)}} + ... + \boldsymbol{P^{(N)}} \tag{1.14}$$

where the i-th components of the second and third order of non-linear polarization are:

$$P_i^{(2)}(\boldsymbol{r},t) = \epsilon_0 \sum_{j,k} \int_{-\infty}^{+\infty} \int_{-\infty}^{+\infty} {\chi_{i,j,k}}^{(2)}(t',t'')E_j(t-t')E_k(t-t'-t'')dt'dt'' \tag{1.15}$$

$$\begin{aligned} P_i^{(3)}(\boldsymbol{r},t) = \epsilon_0 \sum_{j,k,l} \int_{-\infty}^{+\infty} \int_{-\infty}^{+\infty} \int_{-\infty}^{+\infty} {\chi_{i,j,k,l}}^{(3)}(t',t'',t''')E_j(t-t')E_k(t-t'-t'') \\ E_l(t-t'-t''-t''')dt'dt''dt''' \end{aligned} \tag{1.16}$$

In general, the importance of these higher-order terms is smaller and smaller as the order grows; however, when the electric field is strong enough they might become relevant. When the electric field starts to generate a nonlinear polarization in a material, we enter the field that is called nonlinear optics.

Further, additional assumptions can be made:

1. The non-linear response is instantaneous.
2. The non-linear material is isotropic.

Thus, the linear polarization and the second and third-order non-linear polarization can be written as:

$$P^{(l)}(t) = \epsilon_0 \chi^{(1)} E(t) \tag{1.17}$$

$$P^{(2)}(t) = \epsilon_0 \chi^{(2)} E^2(t) \tag{1.18}$$

$$P^{(3)}(t) = \epsilon_0 \chi^{(3)} E^3(t) \tag{1.19}$$

Finally, the polarization can be written as:

$$P = P^{(l)} + P^{(nl)} = \epsilon_0 \chi^{(1)} E(t) + \epsilon_0 \chi^{(2)} E^2(t) + \epsilon_0 \chi^{(3)} E^3(t) \tag{1.20}$$

1.1.3. Helmholtz equation

Considering the propagation equation again (1.9), we can immediately see that it is a partial differential equation therefore, to solve it, we have to move to the frequency domain by applying a Fourier transform. The Fourier transform of a generic function f is defined as:

$$\tilde{F}(\omega) = \mathscr{F}\{f\} = \int_{-\infty}^{+\infty} f(t) \exp^{-i\omega t}\, dt \tag{1.21}$$

The anti-Fourier transform is defined as:

$$f(t) = \mathscr{F}^{-1}\{\tilde{F}\} = \int_{-\infty}^{+\infty} \tilde{F}(\omega) \exp^{i\omega t} \frac{d\omega}{2\pi} \tag{1.22}$$

The following properties hold:

$$\mathscr{F}\left\{\frac{\partial^n f}{\partial t^n}\right\} = (i\omega)^n \tilde{F}(\omega) \tag{1.23}$$

$$\mathscr{F}\{f * g\} = \tilde{F}(\omega)\tilde{G}(\omega) \tag{1.24}$$

By assuming that only the linear polarization (1.17) is present and considering the properties (1.1.3) and (1.1.3) of the Fourier transform, we have by applying both sides the Fourier transform :

$$\frac{\partial^2 \tilde{E}}{\partial z^2} + \frac{\omega^2}{c^2}\tilde{E} = -\frac{\omega^2}{c^2}\tilde{\chi}\tilde{E} \tag{1.25}$$

Let's now define $\tilde{k}^2(\omega) = \frac{\omega^2}{c^2}(1 + \tilde{\chi})$, thus we derive the Helmholtz equation in the Fourier domain:

$$\frac{\partial^2 \tilde{E}}{\partial z^2} + \tilde{k}(\omega)^2 \tilde{E} = 0 \tag{1.26}$$

The solutions of this equation are two: light propagating in the forward direction and light propagating in the backward direction. We select only one possible solution, the forward propagation light:

$$\tilde{E}(z, \omega) = \tilde{E}(z = 0; \omega) \exp^{-i\tilde{k}(\omega)z} \tag{1.27}$$

By using the anti-Fourier transform we get the following:

$$E(z,t) = \int_{-\infty}^{+\infty} \tilde{E}(z=0;\omega)\exp^{i[\omega t - \tilde{k}(\omega)z]}\frac{d\omega}{2\pi} \tag{1.28}$$

The electric field of a pulse can be seen as the sum of different plane waves that propagate with different frequencies ω and different amplitudes $\tilde{E}(0,\omega)$.

1.1.4. Propagation of pulses

In the previous calculations, we applied the Plane Wave Approximation. However, in the following, the propagation of pulses in media will be considered. A pulse can be represented as follows:

$$E(z,t) = A(z,t)cos[\omega_0 t - k_0 z + \phi(z,t)] \tag{1.29}$$

This is called envelope representation of a pulse, where $A(z,t)$ is the envelope, $\cos[\omega_0 t - k_0 z + \phi(z,t)]$ is the optical carrier, ω_0 is the central frequency, k_0 is the central wavenumber, defined as $k_0 = \frac{\omega_0 n(\omega)}{c}$, and $\phi(z,t)$ is the phase. The resulting shape is depicted in 1.1. If we assume $\phi(z=0,t) = 0$ and (1.29) for $z = 0$, then we get:

$$E(z=0,t) = A(z=0,t)cos[\omega_0 t] \tag{1.30}$$

The electric field of the pulse can be rewritten as:

$$E(z=0,t) = A(z=0,t)\frac{e^{i\omega_0 t} + e^{-i\omega_0 t}}{2} \tag{1.31}$$

The Fourier transform can be applied to (1.30) and, by remembering the following property (1.1.3), the following result can be obtained:

$$\mathscr{F}\{E(z=0,t)\} = \tilde{E}(0,\omega) = \mathscr{F}\{A(0,t)\} * \frac{\delta(\omega-\omega_0)}{2} + \mathscr{F}\{A(0,t)\} * \frac{\delta(\omega+\omega_0)}{2} \tag{1.32}$$

Where δ is the delta of Dirac with the property that

$$f(x) * \delta(x - x_0) = f(x - x_0) \tag{1.33}$$

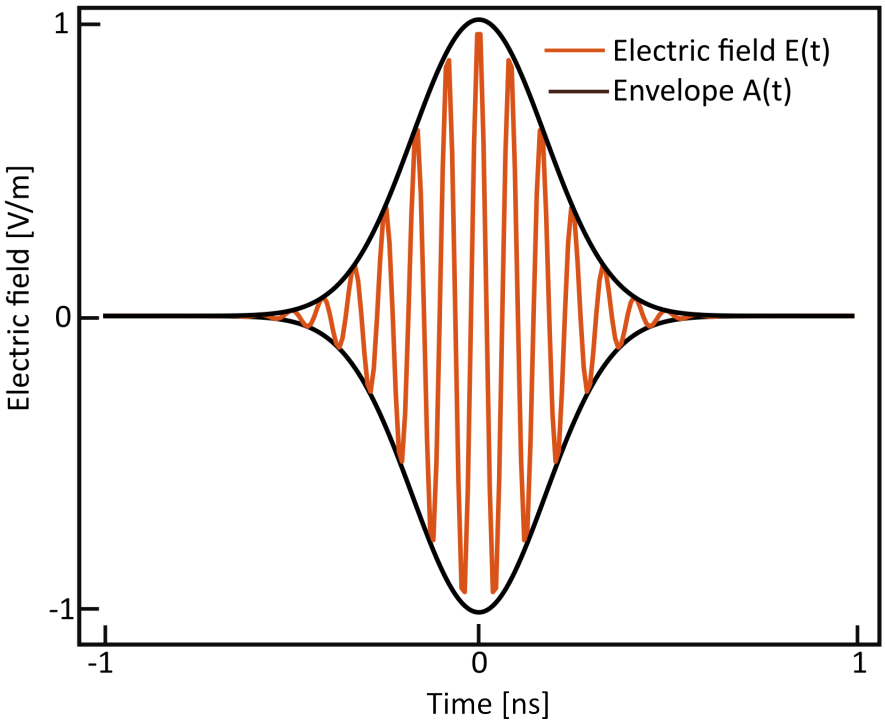

Figure 1.1: Envelope representation of a gaussian pulse.

Let's call $\tilde{A}(0,\omega) = \mathscr{F}\{A\}$, so the Fourier transform of the electric field becomes:

$$\tilde{E}(0,\omega) = \frac{\tilde{A}(0,\omega-\omega_0)}{2} + \frac{\tilde{A}(0,\omega+\omega_0)}{2} \tag{1.34}$$

Since the electric field $E(0,t)$ is a real function such that $\tilde{E}(-\omega) = \tilde{E}^*(\omega)$, we can consider only the positive frequencies because the negative frequencies will carry the same amount of information. Assuming that we consider only pulses in which the optical bandwidth of $\tilde{A}(0,\omega)$ is much smaller than the frequency of the optical carrier ω_0, the electric field of the pulse can be rewritten as:

$$E(z,t) = \int_{-\infty}^{+\infty} \tilde{E}(0,\omega) e^{i[\omega t - \tilde{k}z]} \frac{d\omega}{2\pi} = \int_0^{+\infty} \frac{\tilde{A}(\omega-\omega_0)}{2} e^{i[\omega t - \tilde{k}z]} \frac{d\omega}{2\pi} + c.c. \tag{1.35}$$

where c.c. indicates the complex conjugate. Finally, by remembering that $\tilde{E}(\omega)$ is real, the final expression for the electric field is:

$$E(z,t) = \mathbb{R}e\Big\{ \int_0^{+\infty} \tilde{A}(\omega-\omega_0) e^{i[\omega t - \tilde{k}z]} \frac{d\omega}{2\pi} \Big\} \tag{1.36}$$

Where $\mathbb{R}e$ identifies the real part. Let's now expand in series of power the wavenumber

$k(\omega)$ around ω_0 since $\tilde{E}(0,\omega)$ is defined only near $\pm\omega_0$:

$$\tilde{k}(\omega) = \tilde{k}(\omega_0) + \sum_{n=1}^{+\infty} \frac{d^n\tilde{k}}{d\omega^n}\bigg|_{\omega_0} \frac{(\omega-\omega_0)^n}{n!} \tag{1.37}$$

where $\tilde{k}(\omega_0) = \frac{\omega_0\tilde{n}(\omega_0)}{c}$. Now, let's assume that the refractive index $\tilde{n}(\omega)$ is real, meaning that $n(\omega) = \tilde{n}(\omega)$, thus $k(\omega_0) = \frac{\omega_0 n(\omega_0)}{c}$. At this point, we can define the following quantities:

- the phase velocity v_{ph} at ω_0 is defined as $v_{ph} \triangleq \frac{c}{n(\omega_0)}$
- the group velocity v_g at ω_0 is defined as $\frac{1}{v_g} \triangleq \frac{d\omega}{dk(\omega)}\Big|_{\omega_0}$
- the group velocity dispersion GVD at ω_0 is defined as $GVD \triangleq \frac{d^2k}{d\omega^2}\Big|_{\omega_0}$
- the third order dispersion TOD at ω_0 is defined as $TOD \triangleq \frac{d^3k}{d\omega^3}\Big|_{\omega_0}$

Therefore, we can develop (1.78) as:

$$k(\omega) = \frac{\omega_0}{v_{ph}} + \frac{\omega-\omega_0}{v_g} + \frac{1}{2}GVD(\omega-\omega_0)^2 + \frac{1}{6}TOD(\omega-\omega_0)^3 + ... \tag{1.38}$$

Let's consider only the first order expansion of (1.38) $k(\omega) = \frac{\omega_0}{v_{ph}} + \frac{\omega-\omega_0}{v_g}$, and let's plugs it inside (1.1.4):

$$E(z,t) = \mathbb{R}e\Big\{ \int_0^{+\infty} \tilde{A}(\omega-\omega_0) e^{i[\omega t - \frac{\omega_0}{v_{ph}}z + \frac{\omega-\omega_0}{v_g}z]} \frac{d\omega}{2\pi} \Big\} \tag{1.39}$$

Then, we can sum and subtract $\omega_0 t$ in the exponential in (1.1.4), and subsequently, take out of the integral the terms which do not depend on ω:

$$\begin{aligned}
E(z,t) &= \mathbb{R}e\Big\{ \int_0^{+\infty} \tilde{A}(\omega-\omega_0) e^{i[\omega t - \omega_0 t + \omega_0 t - \frac{\omega_0}{v_{ph}}z + \frac{\omega-\omega_0}{v_g}z]} \frac{d\omega}{2\pi} \Big\} \\
&= \mathbb{R}e\Big\{ \int_0^{+\infty} \tilde{A}(\omega-\omega_0) e^{i[(\omega-\omega_0)t + (t-\frac{z}{v_{ph}})\omega_0 + \frac{\omega-\omega_0}{v_g}z]} \frac{d\omega}{2\pi} \Big\} \\
&= \mathbb{R}e\Big\{ \int_0^{+\infty} \tilde{A}(\omega-\omega_0) e^{i[(\omega-\omega_0)(t-\frac{z}{v_g}) + \omega_0(t-\frac{z}{v_{ph}})]} \frac{d\omega}{2\pi} \Big\} \\
&= \mathbb{R}e\Big\{ e^{i\omega_0[(t-\frac{z}{v_{ph}})} \int_0^{+\infty} \tilde{A}(\omega-\omega_0) e^{i[(\omega-\omega_0)(t-\frac{z}{v_g})]} \frac{d\omega}{2\pi} \Big\}
\end{aligned} \tag{1.40}$$

Let us define $\omega' = \omega - \omega_0$. so $d\omega' = d\omega$. We can rewrite (1.40) as:

$$E(z,t) = \mathbb{R}e\Big\{e^{i\omega_0[(t-\frac{z}{v_{ph}})} \int_{-\omega_0}^{+\infty} \tilde{A}(\omega')e^{i[\omega'(t-\frac{z}{v_g})]}\frac{d\omega}{2\pi}\Big\} \tag{1.41}$$

If we assume that $\omega' << \omega_0$, it is safe imposing that $\int_{-\omega_0}^{+\infty} = \int_{-\infty}^{+\infty}$, then equation (1.41) becomes:

$$\begin{aligned} E(z,t) &= \mathbb{R}e\Big\{e^{i\omega_0[(t-\frac{z}{v_{ph}})}\mathscr{F}^{-1}\{\tilde{A}\}_{t-\frac{z}{v_g}}\Big\} \\ &\mathbb{R}e\Big\{e^{i\omega_0[(t-\frac{z}{v_{ph}})}A(t-\frac{z}{v_g})\Big\} \\ &= A(t-\frac{z}{v_g})\cos\big[\omega_0(t-\frac{z}{v_{ph}})\big] \end{aligned} \tag{1.42}$$

Let's now define the phase delay $\tau_{ph} \triangleq \frac{z}{v_{ph}}$ and the group delay $\tau_g \triangleq \frac{z}{v_g}$, equation (1.42) can be rewritten as:

$$E(z,t) = A(t-\tau_g)\cos\big[\omega_0(t-\tau_{ph})\big] \tag{1.43}$$

In general $\tau_g \neq \tau_{ph}$, so the envelope and the optical carrier propagate with different speeds, thus different delays. So during propagation the optical carrier shifts inside the envelope. Consequently, as the pulse propagates, the optical carrier experiences a shift within the envelope. This phenomenon gives rise to the frequency chirp of the pulse, which will be elaborated upon in the forthcoming paragraph 1.1.5. To precisely quantify this mismatch, we introduce the concept of Carrier-Envelope Phase Offset (CEP):

$$CEP : \psi \triangleq \omega_0\big[\tau_g - \tau_{ph}\big] \tag{1.44}$$

The CEP serves as a quantifiable measure of the misalignment between the optical carrier and the pulse envelope.

1.1.5. Group velocity dispersion

In this section, we will study the effect of the group velocity dispersion GVD on a Gaussian pulse during propagation in a medium. Let's consider a Gaussian pulse given by:

$$E(0,t) = E_0 e^{-\frac{t^2}{2\tau_p^2}}\cos(\omega_0 t) \tag{1.45}$$

where τ_p is the duration of the pulse which is related to the full width at half maximum (FWHM) of the pulse according to this relation $FWHM = \tau_p\sqrt{2\ln 2}$. A representation

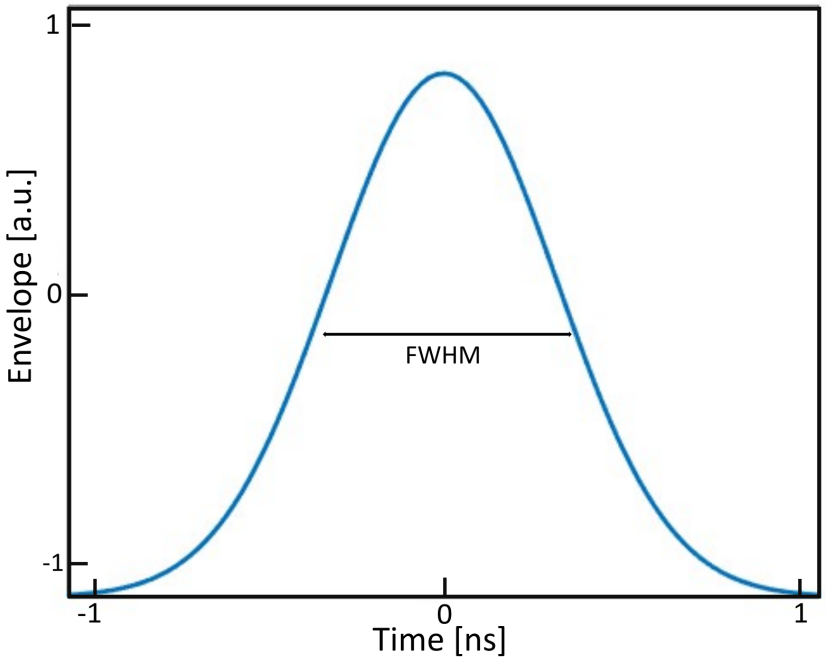

Figure 1.2: Gaussian pulse and its full width at half maximum in time.

of the Gaussian pulse is shown in figure 1.2. The intensity of the pulse is:

$$I(0,t) \propto E^2(0,t) = I_0 e^{-\frac{t^2}{\tau_p^2}} \tag{1.46}$$

By applying the Fourier transform to (1.45), we get:

$$\mathscr{F}\Big\{E(0,t)\Big\} = \sqrt{2\pi} E_0 \tau_p e^{-\frac{\omega^2 \tau_p^2}{2}} \tag{1.47}$$

and the Fourier transform of the envelope is:

$$\tilde{A}(\omega - \omega_0) = \sqrt{2\pi} E_0 \tau_p e^{-\frac{(\omega.\omega_0)^2 \tau_p^2}{2}} \tag{1.48}$$

In order to study the effect of the GVD, we can expand the wavevector k up to the second order $k(\omega) = \frac{\omega_0}{v_{ph}} + \frac{\omega - \omega_0}{v_g} + \frac{1}{2} GVD(\omega - \omega_0)^2$ and we can plug it inside (1.1.4):

$$
\begin{aligned}
E(z,t) &= \mathbb{R}e\Big\{ \int_0^{+\infty} \tilde{A}(\omega-\omega_0) e^{i[(\omega-\omega_0)(t-\frac{z}{v_g})+\omega_0(t-\frac{z}{v_{ph}})+\frac{1}{2}GVD(\omega-\omega_0)^2 z]} \frac{d\omega}{2\pi} \Big\} \\
&= \mathbb{R}e\Big\{ \int_0^{+\infty} E_0\sqrt{2\pi}\tau_p e^{-\frac{(\omega-\omega_0)^2\tau_p^2}{2}} e^{i[(\omega-\omega_0)(t-\frac{z}{v_g})+\omega_0(t-\frac{z}{v_{ph}})+\frac{1}{2}GVD(\omega-\omega_0)^2 z]} \frac{d\omega}{2\pi} \Big\} \\
&= \mathbb{R}e\Big\{ \int_0^{+\infty} E_0\sqrt{2\pi}\tau_p e^{-\frac{(\omega-\omega_0)^2}{2}(\tau_p^2+iGVDz)} e^{i[(\omega-\omega_0)(t-\frac{z}{v_g})+\omega_0(t-\frac{z}{v_{ph}})]} \frac{d\omega}{2\pi} \Big\}
\end{aligned} \tag{1.49}
$$

We can now define a new quantity: $\tilde{\tau}_p^2 \triangleq \tau_p^2 + iGVDz$. Therefore, (1.50) becomes:

$$
\begin{aligned}
E(z,t) &= \mathbb{R}e\Big\{ e^{i\omega_0(t-\frac{z}{v_{ph}})} e^{-\frac{(t-\frac{z}{v_g})^2}{2\tilde{\tau}_p^2}} E_0 \frac{\tau_p}{\tilde{\tau}_p} \Big\} \\
&= \mathbb{R}e\Big\{ e^{i\omega_0(t-\frac{z}{v_{ph}})} e^{-\frac{(t-\frac{z}{v_g})^2}{2(\tau_p^2+iGVDz)}} E_0 \frac{\tau_p}{\tilde{\tau}_p} \Big\} \\
&= \mathbb{R}e\Big\{ e^{i\omega_0(t-\frac{z}{v_{ph}})} e^{-\frac{\tau_p^2(t-\frac{z}{v_g})^2}{2(\tau_p^4+GVD^2z^2)}} e^{-\frac{uiGVD(t-\frac{z}{v_g})^2}{2(\tau_p^4+GVD^2z^2)}} E_0 \frac{\tau_p}{\tilde{\tau}_p} \Big\}
\end{aligned} \tag{1.50}
$$

Now, let's introduce the dispersion length L_D, defined as $L_D \triangleq \frac{\tau_p^2}{GVD}$, and let's define the pulse duration depending on the position z $\tau_p(z)$ define as $\tau_p^2(z) \triangleq \tau_p^2\Big[1+\Big(\frac{z}{L_D}\Big)^2\Big]$. The final form of the electric field of a pulse after the propagation for a length z in a medium is:

$$
E(z,t) \propto e^{-\frac{(t-\tau_g)^2}{2\tau_p^2(z)}} \cos\Big[\omega_0(t-\tau_{ph}) + \frac{z(t-\tau_g)^2}{2L_D\tau_p^2(z)}\Big] \tag{1.51}
$$

We can distinguish two extreme cases in (1.51):

1. if z«L_D $\qquad\qquad$ $\tau_p(z) \approx \tau_p$
2. if z»L_D $\qquad\qquad$ $\tau_p^2(z) \approx \tau_p^2 \frac{z^2}{L_D^2}$

In the first case, the Gaussian beam does not change its duration. In the second case, when the propagation distance is much higher than the dispersion length, the pulse duration in the position z can be written as $\tau_p(z) \approx \tau_p \frac{z}{|L_D|} = \frac{z|GVD|}{\tau_p}$. As a pulse propagates through a dispersive medium, its duration gradually increases. This elongation effect is more pronounced for longer distances and in media with higher group velocity dispersion (GVD). Also, $\tau_p(z) \propto \frac{1}{\tau_p}$ means that shorter initial pulse duration results in larger propagated pulses. Figure 1.3 demonstrates the impact of pulse duration broadening on a Gaussian pulse as it propagates through a dispersive medium.

Let's now consider the phase term that appears in the optical carrier. A generic function $f(t)$, defined as $f(t) = \cos\phi(t)$, has an instantaneous frequency $\omega(t)$ that is defined as

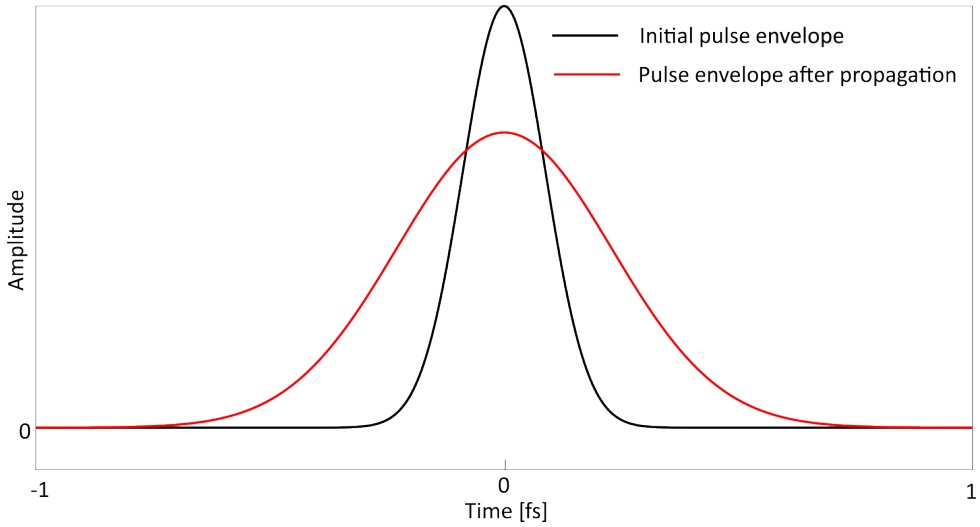

Figure 1.3: The initial Gaussian pulse envelope is represented in black, while the red line depicts the Gaussian pulse envelope after propagation through a dispersive medium.

follow:

$$\omega(t) \triangleq \frac{d\phi}{dt} \tag{1.52}$$

For the propagated Gaussian beam defined by (1.51), the phase term $\phi(t)$ is:

$$\phi(t) = \omega_0(t - \tau_{ph}) + \frac{z(t-\tau_g)^2}{2L_D\tau_p^2(z)} \tag{1.53}$$

The instantaneous frequency is:

$$\omega(t) = \omega_0 + \frac{z(t-\tau_g)}{L_D\tau_p^2(z)} \tag{1.54}$$

After propagation, the instantaneous frequency $\omega(t)$ is not constant along the pulse like at the beginning, now it changes linearly in time along the pulse. In the assumption that $GVD > 0, \quad L_D > 0$, we have that:

- if $t > \tau_g$ $\qquad \omega(t) > \omega_0$
- if $t < \tau_g$ $\qquad \omega(t) < \omega_0$

In the pulse front ($t < \tau_g$) we have the red part of the spectrum ($\omega(t) < \omega_0$) and in the back of the pulse ($t > \tau_g$) we have the blue part of the spectrum ($\omega(t) > \omega_0$). So, thanks to the additional phase term, the pulse is chirped, this means that the red part of the spectrum arrives before the blue part. Such kinds of pulses are called chirped pulses. The frequency chirp is represented in figure 1.4. When the second-order dispersion parameter GVD, holds

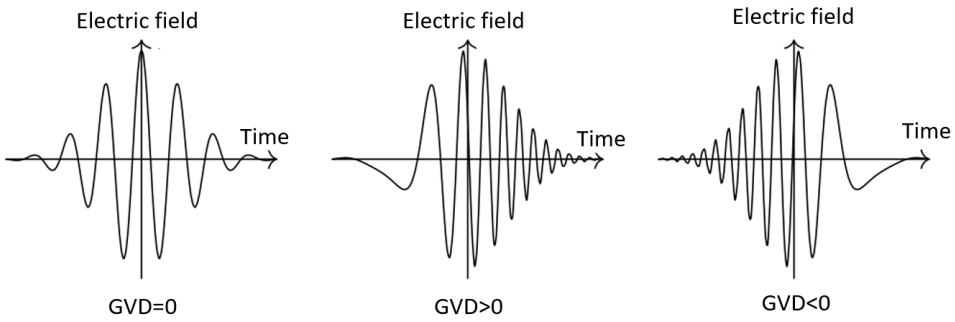

Figure 1.4: Non-chirped pulse (GVD = 0), positively-chirped pulse (GVD > 0), negatively-chirped pulse (GVD < 0).

a positive value, the resultant pulse exhibits an up-chirp characteristic. This phenomenon is termed "normal dispersion." Conversely, if the GVD takes on a negative value, the pulse exhibits a down-chirp behavior, which is referred to as "anomalous dispersion". Considering the spectrum of a pulse, in fact, the frequencies composing the pulse will be traveling at different speeds: if the low-frequencies arrive earlier with respect to the negative ones, the pulse is up-chirped; on the contrary, if the high-frequencies components arrive earlier, we are dealing with a down-chirped pulse. Every “normal” material in the visible range always introduces a positive chirp, making red light travel faster than blue one. This is why, in this range, an up-chirped pulse will be called positive chirped and a down-chirped pulse will be called negative chirped. On the contrary, in the infrared range (for example at $1.5\mu m$, in the third communication window), the blue components will travel faster than the red ones, thus making this convention reversed.

1.1.6. Management of dispersion and optical compressors

As noted in the section 1.1.5, the propagation of a pulse through a dispersive medium results in an elongation of its temporal duration. This outcome is frequently undesirable in applications involving ultrafast optics. In this subsequent paragraph, we shall examine several experimental methodologies that offer the potential to counteract the influence of dispersion and restore the pulse’s initial duration. In the Fourier domain, the electric field of a pulse propagating in a medium can be written as:

$$\tilde{E}(z,\omega) = \tilde{E}(0,\omega)e^{-izk(\omega)} \tag{1.55}$$

where $\tilde{E}(0,\omega)$ is the initial electric field of the pulse in the spectral domain. We can define the following quantity $\phi(z,\omega) \triangleq zk(\omega)$. Thus, equation (1.1.6) becomes:

$$\tilde{E}(z,\omega) = \tilde{E}(0,\omega)e^{-i\phi(\omega)} \tag{1.56}$$

We can expand $k(\omega)$ around ω_0 in (1.1.6) as we did in (1.38), finding:

$$\phi(z,\omega) = \omega_0\tau_{ph} + (\omega-\omega_0)\tau_g + z\sum_{n=2}^{+\infty}\left.\frac{d^nk}{d\omega^n}\right|_{\omega_0}\frac{(\omega-\omega_0)^n}{n!} \tag{1.57}$$

We may define new quantities denoted by D_n, given by $D_n \triangleq \left.\frac{d^nk}{d\omega^n}\right|_{\omega_0} z$. Of particular interest is the group delay dispersion (GDD), which can be expressed as $D_2 \triangleq \left.\frac{d^2k}{d\omega^2}\right|_{\omega_0} z$. Thus, the manifestation of dispersion is the introduction of the phase term $\phi(z,\omega)$. To mitigate the effects of material dispersion, it is necessary to incorporate an optical element, commonly referred to as an optical compressor, which introduces an additional phase term ϕ_c. The electric field at the compressor output $\tilde{E}_c$ is:

$$\tilde{E}_c(z,\omega) = \tilde{E}(0,\omega)e^{-i(\phi(\omega)+\phi_c(\omega))} \tag{1.58}$$

To restore the initial pulse duration and eliminate the impact of dispersion, it is necessary to impose a condition whereby the compensated phase ϕ_c is equal in magnitude but opposite in sign to the original phase term, ϕ. In the ideal scenario, this results in the perfect restoration of the pulse, such that $\tilde{E}_c(\omega) = E(0,\omega)$.However, in practical situations, achieving effective compensation often involves addressing the second- and third-order dispersion components alone, represented by $D_{2c} = -D_2$ and $D_{3c} = -D_3$ respectively. Nevertheless, it's important to note that achieving such compensation may not always be feasible in every circumstance. Figure 1.5 illustrates the operational principles of an optical compressor.

There are different types of optical compressors, such as those based on diffraction grating pairs, prism pairs, active elements, and chirped mirrors. In this discussion, we will focus on the prism pair optical compressor as it is the method that will be used in our experiment.

In a prism pair compressor, the laser beam enters the first prism, which deflects different frequencies in different directions, with the blue component being deflected more than the red components. Next, each spectral component is directed towards a second prism that brings the deflected components parallel to each other, causing the pulse to become spatially chirped. Consequently, different components of the pulse experience different

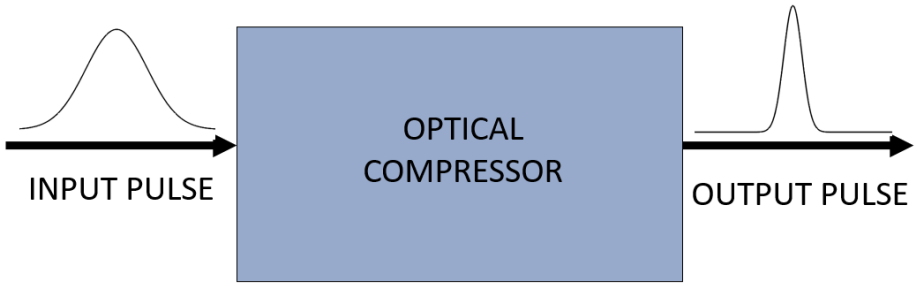

Figure 1.5: Schematic representation that illustrates the operational principles of an optical compressor.

delays. Finally, a mirror or a specular system of prisms is used to recombine the various components, generating a shorter pulse than the original one. Figure 1.6 shows the scheme of a prism compressor. The prisms are typically cut to be in the minimum deviation condition, where the light is less deviated. This corresponds also to the maximum deviation condition, where the different components are more dispersed. To achieve this condition, the correct apex angle is chosen for the prism. Moreover, the prism is cut so that the incident light arrives at the Brewster angle, where the p-polarized light is not reflected and has 100% transmission. In this way, for p-polarized radiation, the losses of the pulse compressor will ideally be zero. The beam experiences normal dispersion as it passes through the prism material. However, the angular dispersion between the prisms introduces anomalous dispersion, which can be greater than the positive dispersion introduced by the material, allowing for a negative group delay dispersion (GDD) to be introduced [32]. The distance between the prisms can be adjusted to increase the anomalous dispersion, and the insertion of one of the two prisms can be changed to tune the D_2 of the prisms while retaining the propagation of the colors.
The GDD introduced by the prism compressor at Brewster angle is [33]:

$$D_{2c} = -\frac{\lambda_0^3}{\pi c^2}\left\{4L\cos(\theta)\left(\frac{dn}{d\lambda}\right)^2_{\lambda_0} - 2L'\sin(\theta)\left[\left(\frac{d^2n}{d\lambda^2}\right)_{\lambda_0} + \left(2n_0 - \frac{1}{n_0^3}\right)\left(\frac{dn}{d\lambda}\right)^2_{\lambda_0}\right]\right\} \quad (1.59)$$

The quantity L denotes the distance between the apices of the prisms, whereas L' refers to the geometric path traversed by the light beam within the prisms. The angle $\theta(\lambda)$ is the angle formed by the path of light of various wavelengths and the reference ray, which corresponds to the path of the central wavelength λ_0. The refractive index of the prism material is represented by n. Usually, the angle θ is small, therefore we can show that $D_{2c} < 0$ and $D_{2c} \propto L$.

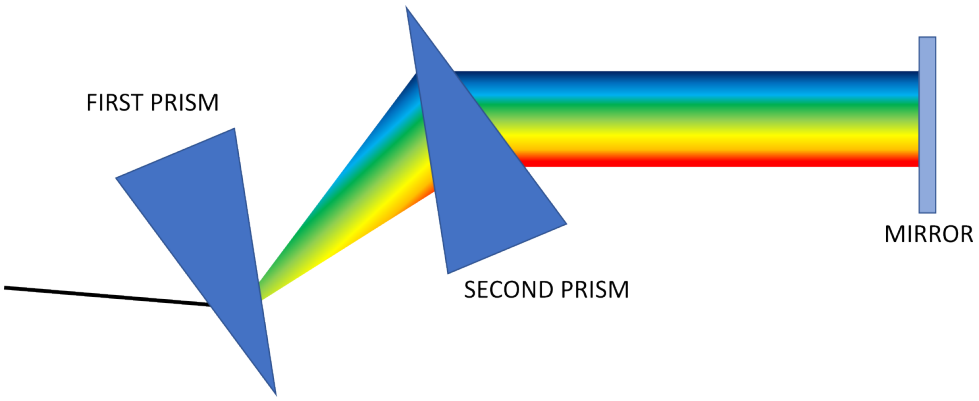

Figure 1.6: Scheme of a prism compressor.

According to [33] also D_{3c} can be obtained:

$$D_{3c} \approx -\frac{2\lambda_0^4}{\pi^2 c^3}\left\{6L\cos(\theta)\left(\frac{dn}{d\lambda}\right)^2_{\lambda_0} - \frac{1}{2}L'\sin(\theta)\left[\left(\frac{d^2n}{d\lambda^2}\right)_{\lambda_0}\right]\right\} \tag{1.60}$$

Since θ is small, we have that $D_{3c} < 0$.
To conclude, we can say that it is possible to select the distance between the two prisms, L, such that the second-order dispersion parameter is nullified. Additionally, the second prism may be positioned on a translation stage, allowing the light to pass through a greater or lesser thickness of glass, thereby providing fine control over the value of the second-order dispersion parameter D2. Specifically, by increasing the thickness of the glass layer, a positive dispersion is added to the inherent material dispersion, thus enabling precise adjustment of the second-order dispersion parameter to zero. However, by choosing:

$$D_{2c} + D_2 = 0 \tag{1.61}$$

we will always have:

$$D_{3c} + D_3 \neq 0 \tag{1.62}$$

Due to the dependence of the third-order dispersion parameter on the distance between the prisms, L, it cannot be independently chosen and controlled alongside the second-order dispersion parameter. Therefore, we lack the necessary degrees of freedom to simultaneously control both parameters. However, one solution to overcome this problem is to use both a grating pair compressor and a prism compressor in succession.

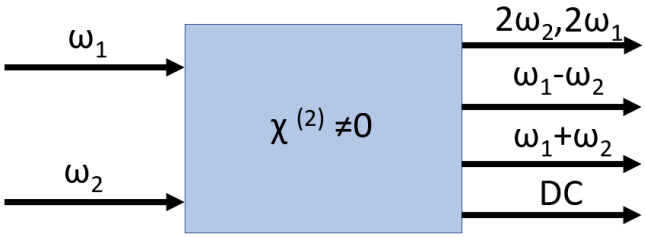

Figure 1.7: This conceptual diagram illustrates the interaction between light and matter through second-order non-linear processes.

1.2. Second-order nonlinear processes

The first type of nonlinear effect encountered during the propagation of pulses is known as the second-order nonlinear effect. These effects occur due to the nonlinear polarization response of materials with non-centrosymmetric properties, which exhibit a nonzero susceptibility of the second order $\chi^{(2)} \neq 0$. In other words, the second-order nonlinear effects arise from the fact that certain materials do not exhibit inversion symmetry, and as a result, they produce a polarization response that is proportional to the square of the electric field. Let's now consider two continuous electromagnetic waves with frequencies ω_1 and ω_2 propagating in a nonlinear material with nonzero susceptibility of the second order. The overall electric field can be written as:

$$E(t) = E_1 cos(\omega_1 t + \phi_1) + E_2 cos(\omega_2 t + \phi_2) \tag{1.63}$$

In this case, the second-order polarization will consist of many different terms:

$$P^{(2)}(t) = \epsilon_0 \chi^{(2)} E^2(t) = \frac{\epsilon_0 \chi^{(2)}}{2} \{E_1^2 + E_2^2 + E_1^2 cos(2\omega_1 t + 2\phi_1) + E_2^2 cos(2\omega_2 t + 2\phi_2) + 2E_1 E_2 cos[(\omega_1 + \omega_2)t + \phi_1 + \phi_2] + 2E_1 E_2 cos[(\omega_1 - \omega_2)t + \phi_1 - \phi_2]\} \tag{1.64}$$

Since polarization is a source of electromagnetic waves, we have the generation of other fields oscillating at different frequencies with respect to the frequencies of the incoming fields. In figure 1.7, a scheme of the light-matter interaction with a material with $\chi^{(2)} \neq 0$ is reported. First of all, the first two terms of (1.64) represent constant fields, this effect is called optical rectification (OR). In principle, this field is expected to be a continuous electric field; however, an ultrashort pulse will have a certain bandwidth of frequencies and

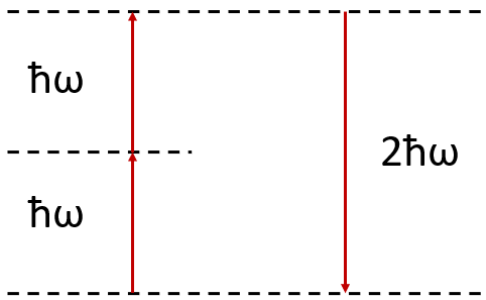

(a) Second harmonic generation (SHG).

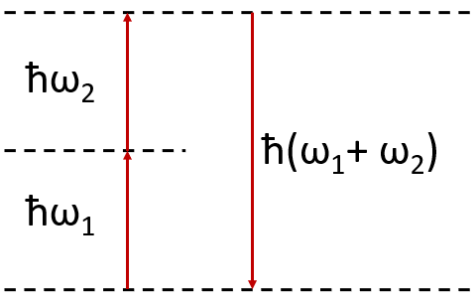

(b) Sum frequency generation (SFG).

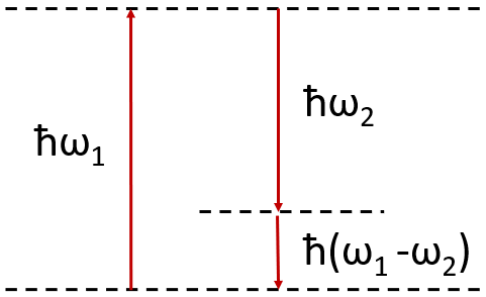

(c) Difference frequency generation (DFG)

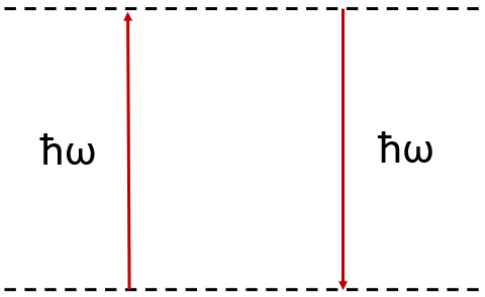

(d) Optical rectification (OR).

Figure 1.8: Jablonsky diagram of second order non-linear processes, respectively:(a) second harmonic generation, (b) difference frequency generation, (c) sum frequency generation, (d) optical rectification.

thus the result of the optical rectification will be a signal whose frequency is proportional to the width of the bandwidth of the pulse. This signal, therefore, will be oscillating in the THz regime, giving a long wavelength in order of the millimeter. The third and the fourth terms are two fields that are oscillating, respectively, at a frequency equal to $2\omega_1$ and $2\omega_2$. This effect is called second harmonic generation (SHG). The fifth term represents a field oscillating at $\omega_1+\omega_2$, this effect is called sum frequency generation (SFG). The last term is a field oscillating at $\omega_1-\omega_2$, this effect is called difference frequency generation (DFG). A DFG process can lead to the occurrence of two complementary effects: Optical Parametric Amplification (OPA) and Spontaneous Down Conversion (SPD). In OPA, the pulse at ω_1 is significantly more intense than those at ω_2. During the interaction, the energy from the most intense pulse is transferred to the weaker one, resulting in the depletion of the former and the generation of a third component at frequency $\omega_1-\omega_2$ is generated. On the other hand, during SPD, only the pulse at ω_1 is presented at the point where it interacts with the crystal. However, the interaction with the crystal leads to the creation of two components at frequencies ω_2 and $\omega_1-\omega_2$. The Jablonsky diagrams corresponding to these second-order linear processes are shown in Figure 3.2.

1.2.1. Envelope propagation equation in a non-linear media

As shown in section 1.1.1, the propagation equation for a linear medium takes the form of (1.9). In this section, we will derive the envelope propagation equation for ultrafast pulses in a nonlinear medium, using the slowly varying envelope approximation (SVEA). In the plane wave scalar approximation in a non-linear media, the propagation equation (1.9) can be rewritten as:

$$\frac{\partial^2 E}{\partial z^2} - \frac{1}{c^2}\frac{\partial^2 E}{\partial t^2} = \mu_0 \frac{\partial^2 P^{(l)}}{\partial t^2} + \mu_0 \frac{\partial^2 P^{(nl)}}{\partial t^2} \tag{1.65}$$

Let's now define the double Fourier transform applied to both the temporal and spatial domains:

$$\hat{E}(\omega, k) = \mathscr{F}_{t,z}\Big\{E(t,z)\Big\} = \int_{-\infty}^{+\infty}\int_{-\infty}^{+\infty} E(t,z)\exp^{i(kz-\omega t)}\, dtdz \tag{1.66}$$

While the two-dimensional Fourier anti-transform is defined as:

$$E(t,z) = \mathscr{F}^{-1}_{\omega,k}\Big\{\hat{E}(\omega,k)\Big\} = \int_{-\infty}^{+\infty}\int_{-\infty}^{+\infty} \hat{E}(\omega,k)\exp^{i(\omega t-kz)}\, \frac{d\omega}{2\pi}\frac{dk}{2\pi} \tag{1.67}$$

Then, we can apply (1.66) and the properties (1.1.3) and (1.1.3) to (1.65). The result is:

$$\left[\frac{\omega^2\epsilon_r(\omega)}{c^2} - k^2\right]\hat{E}(\omega,k) = -\omega^2\mu_0\hat{P}^{(nl)}(\omega,k) \tag{1.68}$$

where $\hat{P}^{(l)}(\omega,k) = \epsilon_0\Big[\epsilon_r(\omega)-1\Big]\hat{E}(\omega,k)$ For a linear medium, we can set $P^{(nl)} = 0$ and obtain two propagation equations: one for the forward-propagating wave and the other for the backward-propagating wave. However, when the medium is nonlinear, we have to express both the polarization and the electric field in terms of their envelopes and optical carriers:

$$E(t,z) = \mathbb{R}e\Big\{A(t,z)e^{i[\omega_0 t - k_0 z]}\Big\} \tag{1.69}$$

$$P^{(nl)}(t,z) = \mathbb{R}e\Big\{B(t,z)e^{i[\omega_0 t - k_p z]}\Big\} \tag{1.70}$$

where the central wavenumber of the non-linear polarization k_p is different from k_0 in general. Let us now apply the Fourier bidimensional transform to (1.69) and (1.70):

$$\mathscr{F}_{t,z}\Big\{E(t,z)\Big\} = \hat{A}(\omega-\omega_0, k-k_0) \tag{1.71}$$

$$\mathscr{F}_{t,z}\Big\{P^{(nl)}(t,z)\Big\} = \hat{B}(\omega-\omega_0, k-k_p) \tag{1.72}$$

The propagation equation (1.68) can be split into two parts, the backward propagation and the forward propagation:

$$\left[\frac{\omega n(\omega)}{c} - k\right]\left[\frac{\omega n(\omega)}{c} + k\right]\hat{E}(\omega, k) = -\omega^2\mu_0\hat{P}^{(nl)}(\omega, k) \tag{1.73}$$

Under the SVEA approximation, we can neglect the backward-propagating term by assuming that:

$$\frac{\omega}{c}n(\omega) + k \approx \frac{\omega_0}{c}n(\omega_0) + k_0 = 2k_0 \tag{1.74}$$

Thus, equation (1.73) becomes:

$$2k_0\left[\frac{\omega n(\omega)}{c} - k\right]\hat{E}(\omega, k) = -\omega^2\mu_0\hat{P}^{(nl)}(\omega, k) \tag{1.75}$$

Next, we can suppose that the non-linear polarization $P^{(nl)}$ has a narrow spectral bandwidth compared to ω_0, which implies that $\omega^2 \approx \omega_0^2$. In this approximation, the envelopes vary slowly in time and space. Thus, we get:

$$\left[\frac{\omega n(\omega)}{c} - k\right]\hat{E}(\omega, k) = -\frac{\omega_0^2\mu_0}{2k_0}\hat{P}^{(nl)}(\omega, k) \tag{1.76}$$

Then, we can substitute (1.71) and (1.72) in (1.76):

$$\left[\frac{\omega n(\omega)}{c} - k\right]\hat{A}(\omega - \omega_0, k - k_0) = -\frac{\omega_0\mu_0 c}{2n(\omega_0)}\hat{B}(\omega - \omega_0, k - k_p) \tag{1.77}$$

Since the pulse is centered in k_0, we can expand $k(\omega)$ in (1.2.1) as:

$$k(\omega) = k_0 + \frac{\omega - \omega_0}{v_g} + \sum_{n=2}^{+\infty}\beta_n\frac{(\omega - \omega_0)^n}{n!} \tag{1.78}$$

We can now apply the two-dimensional Fourier anti-transform (1.67) to both sides of and we can make the following substitution: $\omega' = \omega - \omega_0$, $k' = k - k_0$. and $k'' = k - k_p$. Thus, we obtain:

$$\begin{aligned}\int_{-\infty}^{+\infty}\int_{-\infty}^{+\infty}\left\{\frac{\omega'}{v_g} + \sum_{n=2}^{+\infty}\beta_n\frac{(\omega')^n}{n!} - k'\right\}\hat{A}(\omega', k')e^{i[(\omega'+\omega_0)t-(k_0+k')z]}\frac{d\omega'}{2\pi}\frac{dk'}{2\pi} = \\ = \int_{-\infty}^{+\infty}\int_{-\infty}^{+\infty}\left\{\frac{-\omega_0\mu_0 c}{2n(\omega_0)}\hat{B}(\omega', k'')e^{i[(\omega'+\omega_0)t-(k_p+k'')z]}\frac{d\omega'}{2\pi}\frac{dk'}{2\pi}\right.\end{aligned} \tag{1.79}$$

Let's now multiply by the imaginary unit i:

$$\int_{-\infty}^{+\infty}\int_{-\infty}^{+\infty}\left\{\frac{i\omega'}{v_g}+\sum_{n=2}^{+\infty}\beta_n\frac{(i\omega')^n(-1)^{n-1}}{n!}-ik'\right\}\hat{A}(\omega',k')e^{i[\omega' t-k' z]}\frac{d\omega'}{2\pi}\frac{dk'}{2\pi}= \\ =e^{i(k_0-k_p)}\int_{-\infty}^{+\infty}\int_{-\infty}^{+\infty}\left\{\frac{-i\omega_0\mu_0 c}{2n(\omega_0)}\hat{B}(\omega',k'')e^{i[(\omega' t-k'' z]}\frac{d\omega'}{2\pi}\frac{dk'}{2\pi}\right. \tag{1.80}$$

Let us now apply the Fourier two-dimensional transform, considering the properties of the Fourier transform, and rearrange the term:

$$\frac{1}{v_g}+\frac{\partial A}{\partial t}+\frac{\partial A}{\partial z}+\sum_{n=2}^{+\infty}\frac{\beta_n(-i)^{n-1}}{n!}\frac{\partial^n A}{\partial t^n}=e^{-i\Delta k z}\frac{-i\mu_0\omega_0 c}{2n(\omega_0)}B \tag{1.81}$$

where $\Delta k \triangleq k_p - k_0$. This is the equation for the envelope propagation of ultrafast pulses in a nonlinear medium, using the SVEA approximation. The term B represents the envelope of the nonlinear polarization, which accounts for the nonlinearity of the medium.

1.2.2. Three-Wave Mixing

Let's assume to have a non-linear medium of the second order and three pulses that are impinging on it. We assume that the frequencies of the three pulses are such that $\omega_3 = \omega_2 + \omega_1$. Each of these pulses can be written as:

$$E_1=\frac{1}{2}\Big[A_1(z,t)e^{i(\omega_1 t-k_1 z)}+cc\Big] \tag{1.82}$$

$$E_2=\frac{1}{2}\Big[A_2(z,t)e^{i(\omega_2 t-k_2 z)}+cc\Big] \tag{1.83}$$

$$E_3=\frac{1}{2}\Big[A_3(z,t)e^{i(\omega_3 t-k_3 z)}+cc\Big] \tag{1.84}$$

where $k_1=\frac{\omega_1}{c}n(\omega_1)$, $k_2=\frac{\omega_2}{c}n(\omega_2)$ and $k_3=\frac{\omega_3}{c}n(\omega_3)$.

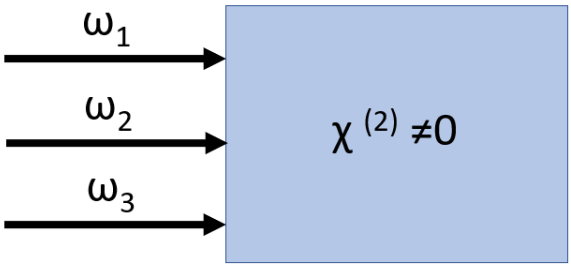

Figure 1.9: Conceptual scheme of the interaction between light and matter considering second-order non-linear processes in the three-wave mixing frame.

The total electric field is $E = E_1 + E_2 + E_3$. The nonlinear polarization acts as a source term for the pulses, so we have to find the components of the polarization at the frequencies that we are interested in. In general, the polarization of the second order can be written as:

$$P^{(2)} = \epsilon_0 \chi^{(2)} E^2 = \frac{\epsilon_0 \chi^{(2)}}{4} \left[A_1(z,t) e^{i(\omega_1 t - k_1 z)} + A_2(z,t) e^{i(\omega_2 t - k_2 z)} + A_3(z,t) e^{i(\omega_3 t - k_3 z)} + cc \right] \tag{1.85}$$

To find the propagation equation for the envelope A_1 we need to look at the terms of the polarization oscillating at $\omega_1 = \omega_3 - \omega_2$:

$$P^{(2)}_{\omega_1} = \frac{\epsilon_0 \chi^{(2)}}{4} \left[2 A_3 A_2^* e^{i[(\omega_3 - \omega_2)t - (k_3 - k_2)z]} + cc \right] \tag{1.86}$$

The non-linear polarization is written as:

$$P^{(2)}(z,t) = \frac{1}{2} \left[B(z,t) e^{i(\omega_0 t - k_p z)} + cc \right] \tag{1.87}$$

So, we can define the following quantities:

$$B_{\omega_1} = \epsilon_0 \chi^{(2)} A_3 A_2^* \tag{1.88}$$

$$k_{p1} = k_3 - k_2 \tag{1.89}$$

We can substitute (1.88) and (1.89) in (1.81) and we can neglect all the dispersion terms $\beta_n = 0$ for $n > 1$. This procedure can be repeated also for the terms oscillating at ω_2 and

ω_3. Then, we get:

$$\begin{cases} \frac{1}{v_g(\omega_1)}\frac{\partial A_1}{\partial t} + \frac{\partial A_1}{\partial z} = -\frac{i\mu_0 c\omega_1}{2n(\omega_1)}\epsilon_0\chi^{(2)}A_2^* A_3 e^{-i\Delta kz} & (1.90a) \\ \frac{1}{v_g(\omega_2)}\frac{\partial A_2}{\partial t} + \frac{\partial A_2}{\partial z} = -\frac{i\mu_0 c\omega_2}{2n(\omega_2)}\epsilon_0\chi^{(2)}A_1^* A_3 e^{-i\Delta kz} & (1.90b) \\ \frac{1}{v_g(\omega_3)}\frac{\partial A_3}{\partial t} + \frac{\partial A_3}{\partial z} = -\frac{i\mu_0 c\omega_3}{2n(\omega_3)}\epsilon_0\chi^{(2)}A_1 A_2 e^{i\Delta kz} & (1.90c) \\ & (1.90d) \end{cases}$$

where $\Delta k = k_3 - k_2 - k_1$. Then, we can define $d_i \triangleq \frac{\mu_0 c\omega_i}{2n(\omega_i)}\epsilon_0\chi^{(2)}$:

$$\begin{cases} \frac{1}{v_g(\omega_1)}\frac{\partial A_1}{\partial t} + \frac{\partial A_1}{\partial z} = -id_1 A_2^* A_3 e^{-i\Delta kz} & (1.91a) \\ \frac{1}{v_g(\omega_2)}\frac{\partial A_2}{\partial t} + \frac{\partial A_2}{\partial z} = -id_2 A_1^* A_3 e^{-i\Delta kz} & (1.91b) \\ \frac{1}{v_g(\omega_3)}\frac{\partial A_3}{\partial t} + \frac{\partial A_3}{\partial z} = -id_3 A_1 A_2 e^{i\Delta kz} & (1.91c) \\ & (1.91d) \end{cases}$$

We are currently in the laboratory frame of reference, so we can switch to the local time frame of reference. However, since there are three pulses with different group velocities, I choose the third pulse as the fixed one. Let's express (1.91) in the local time frame for the pulse A_3 by using the variable change $T = t - \frac{z}{v_g(\omega_3)}$:

$$\begin{cases} \frac{\partial A_1}{\partial z} + \delta_{13}\frac{\partial A_1}{\partial T} = -id_1 A_2^* A_3 e^{-i\Delta kz} & (1.92a) \\ \frac{\partial A_2}{\partial z} + \delta_{23}\frac{\partial A_2}{\partial T} = -id_2 A_1^* A_3 e^{-i\Delta kz} & (1.92b) \\ \frac{\partial A_3}{\partial z} = -id_3 A_1 A_2 e^{i\Delta kz} & (1.92c) \end{cases}$$

where δ_{ij} is the group velocity mismatch defined as $\delta_{ij} \triangleq \frac{1}{v_{gi}} - \frac{1}{v_{gj}}$. In the continuous wave approximation in which the envelope is constant over time $\frac{\partial A_i}{\partial z} \approx 0$, the system (1.92) becomes:

$$\begin{cases} \frac{\partial A_1}{\partial z} = -id_1 A_2^* A_3 e^{-i\Delta kz} & (1.93a) \\ \frac{\partial A_2}{\partial z} = -id_2 A_1^* A_3 e^{-i\Delta kz} & (1.93b) \\ \frac{\partial A_3}{\partial z} = -id_3 A_1 A_2 e^{i\Delta kz} & (1.93c) \end{cases}$$

We can use equations (1.93) to obtain the signal generated by the second harmonic gen-

eration. In this case, we have a single wave with intensity I_ω that splits into two waves oscillating at ω with envelope $\frac{A_\omega}{\sqrt{2}}$. The interaction of these two waves produces a wave with intensity $I_{2\omega}$ at frequency 2ω. Therefore, we set $\omega_1 = \omega_2 = \omega$ and $\omega_3 = 2\omega$. Then, (1.93) becomes:

$$\begin{cases} \dfrac{\partial A_\omega}{\partial z} = -id_\omega A_\omega^* A_{2\omega} e^{-i\Delta kz} & \text{(1.94a)} \\ \dfrac{\partial A_{2\omega}}{\partial z} = -id_{2\omega}\dfrac{A_\omega^2}{2} e^{i\Delta kz} & \text{(1.94b)} \\ & \text{(1.94c)} \end{cases}$$

Next, we apply the no depletion approximation, which assumes that the fundamental wave is so intense that its amplitude does not change after the interaction: $A_\omega(z) \approx A_\omega$:

$$\frac{\partial A_{2\omega}}{\partial z} = -id_{2\omega}\frac{A_\omega^2}{2} e^{i\Delta kz} \tag{1.95}$$

We can integrate (1.95) assuming that the z coordinate is describing the propagation of the wave through the medium and that the following initial condition is valid: $A_{2\omega}(0) = 0$:

$$A_{2\omega} = \int_o^z -id_{2\omega}\frac{A_\omega^2}{2} e^{i\Delta kz} dz \tag{1.96}$$

$$A_{2\omega}(z) = id_{2\omega}A_\omega^2 e^{i\Delta k\frac{z}{2}}\frac{z}{2} sinc\Big(\frac{\Delta kz}{2}\Big) \tag{1.97}$$

The intensity of the second harmonic generation signal is:

$$I_{2\omega}(z) \approx |A_{2\omega}|^2 = \frac{d_{2\omega}^2 I_\omega^2 z^2}{4} sinc^2\Big(\frac{\Delta kz}{2}\Big) \tag{1.98}$$

The perfect phase matching condition occurs when $\Delta k = 0$, which means that there is constructive interference between all the partial second harmonic contributions generated inside the crystal by the nonlinear polarization. In this case, the second harmonic intensity is proportional to $I_{2\omega} \propto d_{2\omega}^2 I_\omega^2 z^2$. The phase mismatch occurs when $\Delta k \neq 0$, in this case, the second harmonic intensity is proportional to $I_{2\omega} \propto d_{2\omega}^2 I_\omega^2 \sin^2(\frac{\Delta kz}{2})$.
The SHG signal will be analyzed in more depth in the following section, where we will also discuss its potential practical applications.

1.2.3. Second Harmonic Generation Microscopy

In this section, we introduce a type of microscopy that utilizes Second Harmonic Generation (SHG) for imaging, which I employ in conjunction with CARS microscopy to obtain more specific chemical information about the sample.

In recent years, SHG has emerged as a powerful nonlinear optical contrast mechanism for biological and biophysical imaging applications [34]. This coherent process involves the up-conversion of two lower energy photons to exactly twice the incident frequency or half the wavelength, as depicted in Figure 1.10. Numerous studies have demonstrated the potential of SHG in tissue imaging, particularly in visualizing collagen fibers in various connective tissues such as skin, bone, tendon, blood vessels, and cornea, as well as fibrotic collagen in internal organs like lung, liver, and kidney [35–37]. In our experimental setup, SHG microscopy is primarily employed to visualize collagen, a group of proteins present in most connective tissues. At the molecular level, collagen comprises three α chains, known as tropocollagen, which are held together by hydrogen bonds [38]. In certain types of collagen, particularly types I and II, these triple helices spontaneously self-organize into well-structured collagen fibrils [39], leading to robust SHG signals [40]. Conversely, non-fibrillar collagen (e.g., type IV), which forms sheets in basal laminae, cannot be imaged with SHG microscopy [41].

SHG microscopy is an ideal approach for in situ tissue imaging due to its endogenous contrast, which arises purely from endogenous species in the sample, as well as its reduced photobleaching and phototoxicity relative to fluorescence methods [42]. So no dyes or fluorophores are needed. This contrast mechanism is also sensitive to the physical structure, and high-resolution, deep-tissue imaging to depths of several hundred microns can be achieved using near-infrared laser fundamental wavelengths [30]. So SHG provides high sensitivity and specificity and optical sectioning capability for imaging bulk tissue in $3D$. As discussed in earlier sections, SHG is a second-order nonlinear optical mechanism that arises from a polarization of the second order. This implies that the environment must possess a non-centrosymmetric structure on the scale of the SHG wavelength, thereby making SHG highly sensitive to filamentous proteins in biological samples [43]. Although this requirement limits the applicability of SHG to a few structures, it is also a key strength of the technique as the resulting signals are highly specific and yield sharp contrast images.

At the molecular level, second harmonic generation arises from the hyperpolarizability of peptide bonds in collagen (chemical bonds that link amino acids together to form a protein chain) and tubulin, which are typically considered single SHG emitters [44]. When an electric field oscillates at a high frequency and reaches a collagen structure, it repeatedly pulls the electrons back and forth, leading to the induction of a molecular dipole. This can be mathematically expressed as:

$$p = p^{(0)} + \alpha E + \beta E^2 + \gamma E^3 + ... \tag{1.99}$$

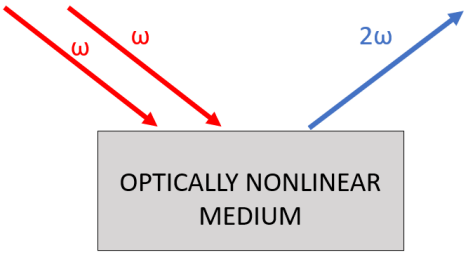

Figure 1.10: . Second-harmonic generation (SHG) is a nonlinear optical process, in which two photons of lower energy combine to create a new photon at exactly twice the incident frequency or half the wavelength.

where α is the polarizability of electrons of the peptide bond, E is the incident electric field, and β and γ are the hyperpolarizabilities of the first and second order, respectively. The first term, $p^{(0)}$, represents the permanent dipole of the molecule. The second term corresponds to the linear response, the third one defines second-order non-linear interactions. SHG arises from the third term in Equation (1.99). Molecules capable of emitting SHG are characterized by a high hyperpolarizability β, which strongly depends on their symmetry. In the case of a molecule having a center of symmetry, elements contributing to the molecule's hyperpolarizability cancel each other, preventing SHG formation. More generally, the generation of even harmonics is only possible in non-centrosymmetric materials. The coherent nature of SHG implies that the signal results from interferences of individual contributions of collagen structures. For example, when the electric fields emitted by two dipole moments are in phase and constructively interfere, the resulting SHG is coherently added. However, there is destructive interference when the dipole moments have opposite directions, and the SHG signal vanishes.

At the macroscopic scale, SHG is described by the non-linear susceptibility of the second order, which results from the coherent summation of the individual hyperpolarizabilities of all pharmacophores within a volume. This phenomenon gives rise to the polarization of the second order (1.18). The relation between the molecular and macro-molecular non-linear response is given by $\chi^{(2)} = N_S < \beta >$, where N_S is the density of molecule S and $< \beta >$ is the orientational average of the first hyperpolarizability. For SHG to occur at this scale, the medium should exhibit a $\chi^{(2)} \neq 0$, which only happens for a non-centrosymmetric macro-molecular organization. Consequently, to perform SHG microscopy in biological samples, the tissue must present a non-centrosymmetric structure both at the molecular scale ($\beta \neq 0$) and at the macro-molecular level ($< \beta > \neq 0$) as well as a high density of pharmacophores. SHG can thus act as a unique probe of the multiscale distribution of molecules within the sample, as for collagen.

The SHG signal possesses several fundamental properties. In the present study, we focus on collagen fibrils, which exhibit cylindrical symmetry. The first property is that SHG is polarization sensitive. In general, it can be assumed that the Kleinman symmetry is valid, and the chiral components of the non-linear susceptibility tensor can be neglected due to the in-focus orientation of the fibrils [45]. Under these conditions, the non-linear susceptibility tensor only has two independent components, namely χ_{xxx} and χ_{xyy}, where x represents the fibrillar axis. When the input laser is linearly polarized and propagates along the z-axis, the SHG intensity in each pixel of an image can be expressed as follows:

$$I_{SHG}(\theta, \mu) = A + B\cos(2\mu - 2\theta) + C\cos(4\mu - 4\theta) \tag{1.100}$$

where μ is the polarization angle with respect to the x-axis, θ is the azimuthal angle of the fibril with the x-axis, and A, B, and C are coefficients dependent on the pharmacophore concentration and arrangement [31]. Hence, the SHG intensity from a collagen sample is strongly influenced by the incident polarization of the laser excitation light with respect to the fiber axis. This means that the polarization dependence of the SHG signal can be measured to study the orientation of the collagen fibrils within the tissue. If the light is polarized along the fiber axis, the maximum SHG signal will be observed. On the other hand, if it is polarized perpendicular to the fiber axis, the weakest SHG signal will be observed. Also, the intensity of the SHG signal depends on the angle between the collagen fiber and the imaging plane. The intensity of the SHG is maximized when the collagen fiber is in the imaging plane and very low when the fiber is perpendicular to the imaging plane. Furthermore, since SHG is a coherent process, the phase of the incoming field also affects the SHG signal. Assuming a fixed polarization and propagation direction of the incident laser beam and utilizing the slowly varying envelope approximation, the SHG intensity can be expressed as:

$$I_{SHG} \propto I_{in}^2 L^2 sinc^2\Big(\frac{\Delta k L}{2}\Big) \tag{1.101}$$

where I_{in} is the intensity of the incident laser beam, L is the length over which SHG occurs in the medium, and $\Delta k = 2k_\omega - k_{2\omega}$ represents the phase mismatch between the excitation and the emitted light wavenumber. When the phase-matching condition $\Delta k = 0$ is satisfied, the SHG intensity scales directly with the square of the input laser intensity and the square of L. The SHG signal can be obtained only if the induced dipoles radiate in phase. This phase matching ensures that the contributions add up constructively from all positions in the focal volume. The coherent length L_C can be defined as $L_C = \frac{\pi}{\Delta k}$. However, if $\Delta k \neq 0$, the SHG intensity reaches a maximum value after propagation

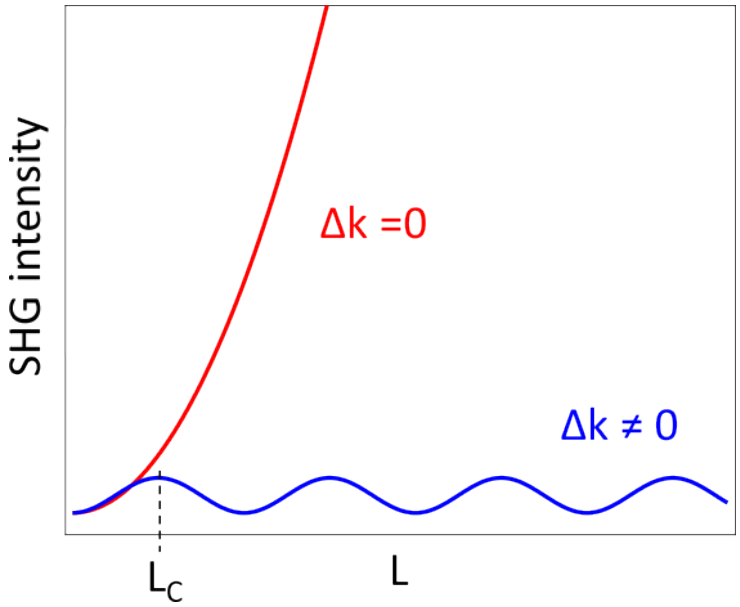

Figure 1.11: This plot illustrates the behavior of SHG intensity as a function of the medium length over which SHG occurs (L) under perfect phase matching conditions ($\Delta k = 0$ in red) and in the case of phase mismatching ($\Delta k \neq 0$ in blue). Also, the coherent length L_C is highlighted.

of L_C. In that case, if the interaction length L exceeds this value, the SHG intensity oscillates between zero and the maximum value. The two cases are depicted in Figure 1.11. In biological samples, the phase-matching condition is rarely fulfilled, leading to the directionality of the SHG signal. However, in the forward direction, ΔkL is approximately zero since the length of interaction is small compared to L_C (few microns) due to tight focusing. In the backward direction, however, Δk is much larger, and the coherence length is much shorter (a few tens of nanometers)[29]. This is why pure backward second-harmonic generation is consistently very weak. Typically, between 80% and 90% of the SHG signal from collagen in a tissue sample will propagate in the forward direction, depending on how much the sample scatters light [30].

1.3. Light matter interaction

1.3.1. Harmonic oscillator

In light-matter interaction, the interaction between a monochromatic electromagnetic wave and a molecule can be modeled as a driven harmonic oscillator. The molecule can be seen as a mass-spring system, as depicted in figure 1.12, where x_0 is the equilibrium

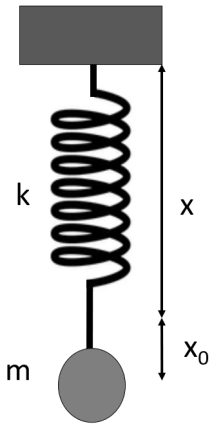

Figure 1.12: A mass-spring system where x is the displacement from the equilibrium position x_0, m the mass and K is the stiffness,

position, m is the mass, and k is the stiffness. The displacement x from the equilibrium position x_0 of the harmonic oscillator is described by the following equation:

$$\frac{d^2x}{dt^2} + \omega_0^2 x = 0 \tag{1.102}$$

where $\omega_0 = \frac{k}{m}$ is the system resonant frequency.
To improve the model, we can consider a damped harmonic oscillator in which the mass experiences a friction force $F = -2\gamma m\frac{dx}{dt}$ where γ is the damping factor. In this case, equation (1.102) becomes:

$$\frac{d^2x}{dt^2} + 2\gamma\frac{dx}{dt} + \omega_0^2 x = 0 \tag{1.103}$$

Since we would like to model the interaction with the electromagnetic field, we need to introduce a driving force oscillating periodically. Hence we define $F(t) = F_0 cos(\omega t)$, where F_0 represents the amplitude, while ω is the angular frequency. Introducing the driving force $F(t)$, equation before becomes:

$$\frac{d^2x}{dt^2} + 2\gamma\frac{dx}{dt} + \omega_0^2 x = \frac{F(t)}{m} \tag{1.104}$$

Normally, the complex representation of the force is used $F(t) = F_0 e^{-i\omega t}$. We look for a solution of the kind $x(t,\omega) = x(\omega)e^{-i\omega t}$ and inserting this kind of solution in (1.104), we get:

$$\Big(-\omega^2 - 2i\gamma\omega + \omega_0^2 \Big) x(\omega)e^{-i\omega t} = \frac{F_0 e^{-i\omega t}}{m} \tag{1.105}$$

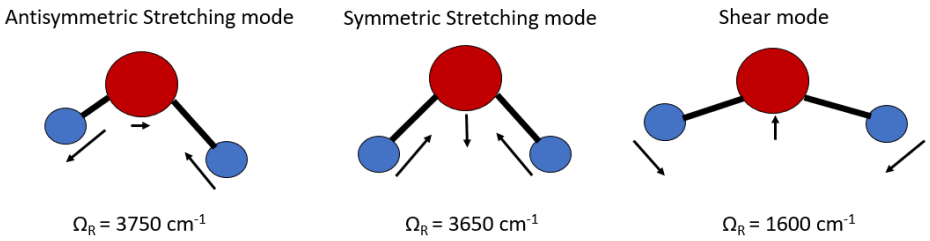

Figure 1.13: Antysimmetric stretching mode, symmetric stretching mode, and shear mode of a water molecule.

where $x(\omega)$ can be expressed as:

$$x(\omega) = \frac{F_0/m}{\omega_0^2 - \omega^2 - 2i\gamma\omega} \tag{1.106}$$

Close to resonance ($\omega \approx \omega_0$), and for a small damping coefficient ($\gamma \ll \omega_0$), the harmonic oscillator solution (1.107) can be simplified to [46]:

$$x(\omega) = \frac{-F_0/(2m\omega_0)}{(\omega - \omega_0) + i\gamma} \tag{1.107}$$

1.3.2. Vibrational modes

In the preceding section, it was demonstrated that a molecule can be conceptualized as a harmonic oscillator. Generally, a molecule sustains numerous intramolecular vibrations, referred to as normal modes, which can be rotational or vibrational in nature. A vibrational mode is defined as a periodic movement of the atoms of a molecule relative to one another, with the center of mass remaining stationary. Each normal mode is characterized by a unique resonance frequency Ω_R. For a molecule that consists of n atoms and has a non-linear geometry, there will be $3n - 6$ normal vibration modes, whereas, for a linear geometry, there will be 3n-5 normal vibration modes as the molecule remains unaltered due to any rotation along its molecular axis. For example, the water molecule has three modes of vibrations that are shown in 1.13. Hence, diatomic molecules ($n = 2$) will have only one normal vibration mode.

The present discussion is centered on a single, isolated diatomic molecule consisting of two point-like nuclei with masses m_1 and m_2, separated by a distance of x_0. This system can be accurately represented as a harmonic oscillator, with its vibrational mode possessing a distinct resonant frequency Ω_R. Moreover, we shall consider the diatomic molecule to be polar, with an uneven distribution of charges. Specifically, the atom m_1 will bear a

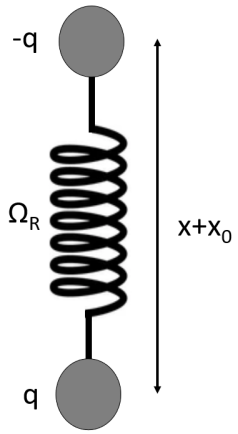

Figure 1.14: Model of a diatomic molecule: two masses, with charges $\pm q$ and resonant frequency Ω_R, attached to a spring.

charge of +q, while the atom m_2 will have a charge of -q, as illustrated in figure 1.14.

Let us now examine an electric field with an angular frequency ω that is linearly polarized along the molecule axis. This electric field generates a force on the molecule, denoted by $F_{lorentz}(t) = qE_o e^{-i\omega t}$. The elongation of the harmonic oscillator in response to this force is described by the following differential equation:

$$\frac{d^2x}{dt^2} + 2\gamma\frac{dx}{dt} + \Omega_R^2 x = \frac{F_{lorentz}(t)}{\mu} \tag{1.108}$$

Here, μ represents the reduced mass, defined as $\mu = m_1 m_2/(m_1 + m_2)$. The damping term γ describes the radiation loss of the oscillating dipole. By solving Equation (1.108), the solution is given by:

$$x(\omega) = \frac{-F_{lorentz/(2\mu\Omega)}}{(\omega - \Omega_R) + i\gamma} \tag{1.109}$$

Now, let us consider a macroscopic medium consisting of N of these molecules. Under the influence of the electric field, the displacement of the electronic cloud of each molecule induces a total polarization of the medium, which can be .calculated as the sum of all the individual dipole moments:

$$P(\omega) = Nqx(\omega) \tag{1.110}$$

The linear electronic susceptibility χ is defined as:

$$P(\omega) = \epsilon_0 \chi(\omega) E(\omega) \tag{1.111}$$

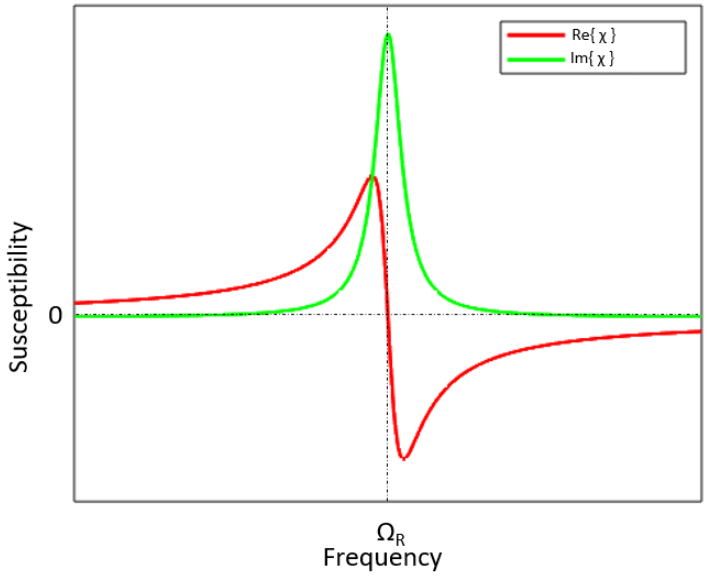

Figure 1.15: Graph of the real (red curve) and imaginary (green curve) parts of the linear susceptibility.

Substituting Equation (1.109) into Equation (1.110), we obtain the expression for the linear susceptibility:

$$\chi(\omega) = \frac{-\frac{Nq^2}{2\epsilon_0 m\Omega_R}}{(\omega - \Omega_R) + i\gamma} \tag{1.112}$$

In the context of diluted media, the real part of the susceptibility χ is closely linked to the dispersion of refractive index, which can be expressed as:

$$n(\omega) = n_0 - \frac{\mathbb{R}e\Big[\chi(\omega)\Big]}{2n_0} \tag{1.113}$$

Here, n_0 represents the mean refractive index of the medium. Conversely, the imaginary part of χ is linked to the absorption coefficient of the medium, as expressed by the following equation:

$$\alpha(\omega) = \frac{2\pi}{\lambda_0 n_0}\mathbb{I}m\Big[\chi(\omega)\Big] \tag{1.114}$$

The real and imaginary parts of the linear susceptibility are schematically depicted in Figure 1.15

The absorption coefficient is an important parameter in the Lambert-Beer law, which describes the attenuation of light intensity from I_0 to $I(L)$ as it passes through a distance L in a given medium.

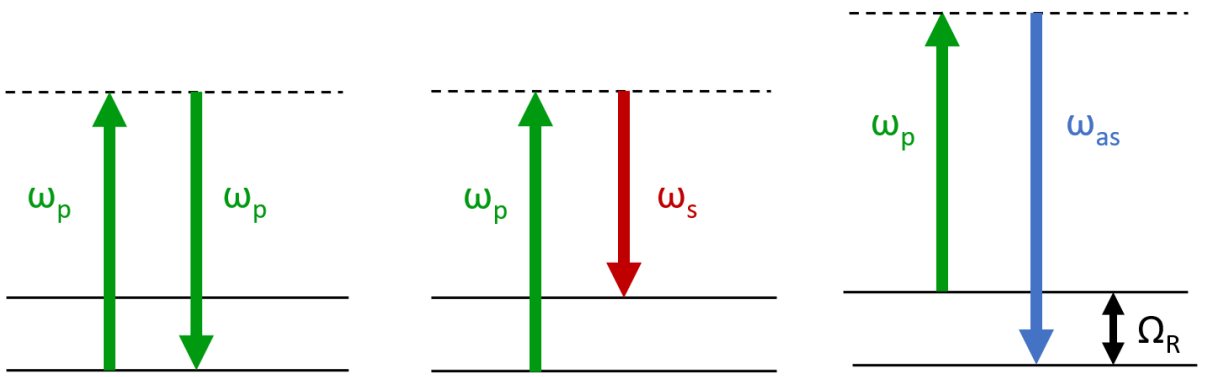

(a) Rayleigh Scattering. (b) Stokes Raman Scattering. (c) anti-Stokes Raman Scattering

Figure 1.16: Jablonsky diagram of Spontaneous Raman scattering mechanisms, respectively:(a) Rayleigh Scattering, (b) Stokes Raman Scattering, (c) anti-Stokes Raman Scattering.

1.3.3. Spontaneous Raman scattering

When light interacts with matter, two main mechanisms are observed: absorption and scattering. During absorption, a molecule retains energy for a certain period of time. On the other hand, during scattering, the molecule instantaneously scatters the incoming light in a different direction. When a molecule scatters light, most of the scattered photons retain their original frequencies, which is a phenomenon known as elastic scattering or "Rayleigh scattering". However, a small fraction of the incident light is scattered in an inelastic way meaning scattered with a frequency different from the original incoming light, a phenomenon known as the "Raman effect". The Raman effect is divided into two main effects: Stokes Raman scattering, in which the light is scattered with a red-shifted frequency with respect to the impinging one, and anti-Stokes Raman scattering, in which the scattered light is blue-shifted. These processes are depicted in Figure 1.16.

Consider a diatomic molecule, which is not necessarily polar, but its polarizability depends on the intramolecular distance x. This distance fluctuates at the resonant molecular bond frequency $x(t) = x_f \cos(\Omega_R t)$, where x_f is the amplitude fluctuation. For small displacements, it is possible to perform a Taylor expansion of the polarizability $\alpha(t)$ near its initial value α_0:

$$\alpha(t) = \alpha_0 + \left(\frac{\partial \alpha}{\partial x}\right)_0 x(t) \tag{1.115}$$

The dipole moment induced by an oscillating electric field $E(t) = E_0 \cos(\omega_p t)$:

$$p(t) = \epsilon_0 \alpha(t) E(t) \tag{1.116}$$

By substituting equation (1.115) into(1.116), we obtain:

$$p(t) = \epsilon_0 \Big[\alpha_0 + \Big(\frac{\partial \alpha}{\partial x}\Big)_0 x_f \cos(\Omega_R t)\Big] E_0 \cos(\omega_p t) \tag{1.117}$$

By developing (1.117):

$$p(t) = \epsilon_0 \alpha_0 E_0 \cos(\omega_p t) + \frac{\epsilon_0 \Big(\frac{\partial \alpha}{\partial x}\Big)_0 E_0 x_f}{2} \cos[(\omega_p - \Omega_R)t] + \frac{\epsilon_0 \Big(\frac{\partial \alpha}{\partial x}\Big)_0 E_0 x_f}{2} \cos[(\omega_p + \Omega_R)t] \tag{1.118}$$

In equation (1.118), we can identify three terms. The first term, with frequency ω_p, describes Rayleigh scattering. The second term, with frequency $\omega_s = \omega_p - \Omega_R$, describes Raman Stokes scattering, in which the molecule moves from its ground state to an excited vibrational state, while the incoming field loses energy. The third term, with frequency $\omega_{as} = \omega_p + \Omega_R$, describes anti-Stokes Raman scattering, where the molecule goes from the excited vibrational state towards its ground state, giving energy to the incoming photon. Experimentally, the anti-Stokes scattered intensity is lower than the Stokes scattered intensity. The reason why the excited vibrational level has a lower population than the ground state level at thermal equilibrium is due to the Boltzmann distribution governing atomic level populations. In order for a vibrational mode to be Raman active, it must affect the polarizability, and thus the selection rule is given by $(\frac{\partial \alpha}{\partial x})_0 \neq 0$. Raman spectroscopy, similar to IR absorption spectroscopy, can be used to identify vibrational levels and measure their energy by analyzing the spectral distance of Raman peaks in relation to the Rayleigh scattering peak (see Figure 1.17). If a molecule possesses inversion symmetry, its modes may be Raman active but not IR active or vice versa. Symmetric modes with respect to inversion symmetry are exclusively Raman active, whereas anti-symmetric modes are only IR active.

So, Raman spectroscopy is a technique that detects molecular vibrations reflecting the structures and chemical conditions of molecules in a sample and was originally used to directly visualize the chemical responses of endogenous molecules. It is now increasingly popular among biologists because it provides an overall molecular vibrational profile, containing Raman bands for major cellular building blocks, such as proteins, nucleic acids, lipids, and carbohydrates. A Raman spectrum can be regarded as a phenotype of a bio-

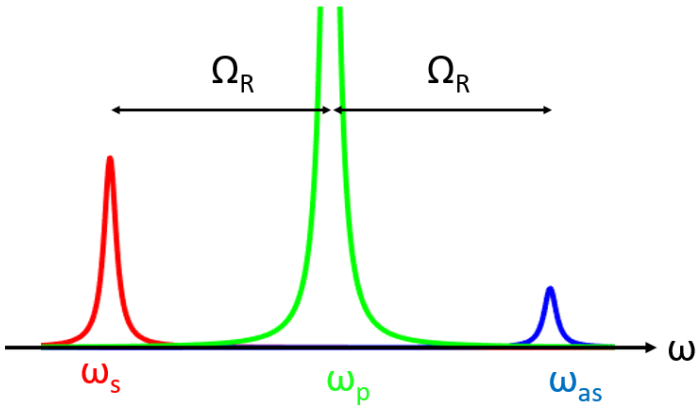

Figure 1.17: Scattered light from a molecule with a single vibrational mode at frequency Ω_R. From the left, the Stokes, Rayleigh, and anti-Stokes scattering can be seen in which the anti-Stokes scattered line is less intense than the Stokes one.

logical system.

A biological Raman spectrum can be divided into three regions: the 'fingerprint' region that contains essential bio-information and can be seen as a fingerprint of a cell (400-1800 cm^{-1}); the 'silent' region that usually does not involve vibrational modes contributed by biomolecules formed of naturally occurring isotopes and can involve bands contributed by stable isotopes or triple bonds (1800–2700 cm^{-1}); the high-wavenumber region that is specifically contributed by the stretching vibrations of CH groups, predominantly from lipids and proteins (2700–3200 cm^{-1}). Figure 1.18 illustrates a Raman spectrum of a single glioblastoma cell with Raman bands marked with assignments of major biological macromolecules.

The advantages of using Raman micro-spectroscopy in biological studies are high spatial resolution; the ability to detect aqueous samples; intrinsic and label-free characterization; non-contacting and non-destructive analysis; and easy preparation and small sample volume. By combining the power of optical magnification and direct visualization, Raman micro-spectroscopy can probe biological systems at a subcellular resolution. For large biological systems like tissues, it can collectively produce label-free Raman images with subcellular structural and chemical information. The disadvantages of Raman spectroscopy is intrinsically weak Raman scattering as approximately only 1 in 10^7 photons experiences inelastic scattering, therefore the cross-section of Raman scattering is relatively low, with a magnitude of around $10^{-30} cm^2$, compared to the cross-section of single photon absorption fluorescence which can reach $10^{-16} cm^2$. Another Raman-based approach that has emerged in recent decades to obtain much stronger vibrational signals is coherent Raman scattering (CRS), which employs multiple light sources to produce coherent Raman sig-

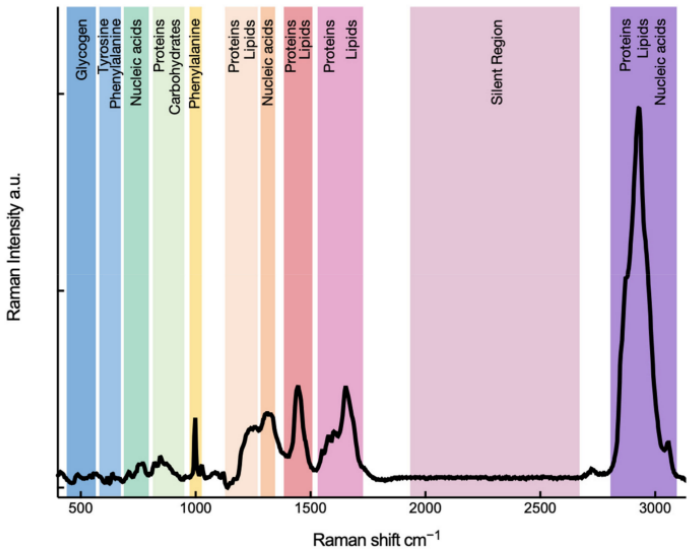

Figure 1.18: The Raman spectrum of a single cell of human primary glioblastoma U87 cell line highlighting various bands that represent cellular constituents. Taken from [65].

nals.

1.3.4. Coherent Raman Scattering

The preceding section emphasized that the primary drawback of Raman spectroscopy is its limited cross-section. Consequently, acquiring a vibrational spectrum necessitates a substantial investment of time to achieve a satisfactory signal-to-noise ratio. However, coherent Raman scattering (CRS) offers a solution to this limitation by providing a 10^7 fold enhancement in efficiency compared to spontaneous Raman scattering.
Assuming the presence of a medium with roto-vibrational vibrations Ω_R, we can examine the interaction of two incoming plane waves, referred to as pump and Stokes, which have frequencies ω_p and ω_s, respectively. The composite field can be expressed as:

$$E(z,t) = A_p e^{i(k_p z - \omega_p t)} + A_s e^{i(k_s z - \omega_s t)} + c.c. \tag{1.119}$$

where c.c. is the complex conjugate.
When the two fields interact, their interference produces a beat signal with a frequency of $\Omega = \omega_p - \omega_s$. If this frequency matches the roto-vibrational mode's frequency Ω_R the system enters into resonance with the wave beating.
Let us now focus on the driven harmonic oscillator model that describes a diatomic molecule, similar to what was discussed in the previous section. The energy required

to create a dipole moment $\boldsymbol{p}(t) = \epsilon_0 \alpha(t) \boldsymbol{E}(t)$ is denoted by W, and can be expressed as:

$$W = \frac{1}{2}\Big\langle \boldsymbol{p}(z,t)\boldsymbol{E}(z,t)\Big\rangle = \frac{1}{2}\epsilon_0 \alpha(t)\Big\langle E^2(z,t)\Big\rangle, \tag{1.120}$$

where the time average over one optical period is represented by the brackets <>. We can then derive the excitation force on the molecule produced by the two incoming fields as the derivative of energy with respect to the intermolecular distance, resulting in:

$$F(t) = \frac{dW}{dx} = \epsilon_0 \Big(\frac{\partial \alpha}{\partial x}\Big)\Big[A_p A_s^* e^{i(\Omega t - kz)} + c.c\Big] \tag{1.121}$$

where the intensity term is given by:$\Big\langle E^2(z,t)\Big\rangle = A_p A_s^* e^{i(\Omega t - kz)} + c.c.$ We can solve equation (1.104) by substituting the form of (1.121) into it and looking for a solution of the following type:

$$x(z,t) = x(\Omega) e^{i(\Omega t - kz)} + c.c. \tag{1.122}$$

Close to the resonance, the molecular vibration amplitude can be described by:

$$x(\Omega) = \frac{-\Big(\frac{\epsilon_0}{2\mu\Omega_R}\Big)(\frac{\partial \alpha}{\partial x}) A_p A_s^*}{(\Omega - \Omega_R) + i\gamma}. \tag{1.123}$$

When the beat frequency is equal to the roto-vibrational mode frequency, i.e., $\Omega = \Omega_R$, the molecular vibration amplitude becomes significant, resulting in the excitation fields inducing nonlinear polarization that is specific to the molecular resonance.
Let's calculate the total induced polarization in the medium by summing the induced dipole moments. The polarization can be expressed as:

$$P(z,t) = Np(z,t) = N\epsilon_0 \Big[\alpha_0 + \Big(\frac{\partial \alpha}{\partial x}\Big) x(z,t)\Big] E(z,t) \tag{1.124}$$

Here, N represents the molecular density. We observe that the polarization consists of a linear polarization term $P^L(z,t) = N\epsilon_0 \alpha_0 E(z,t)$ and a non-linear polarization term, which can be expressed as:

$$P^{NL}(z,t) = P(\omega_{as}) e^{-i\omega_{as} t} + P(\omega_{cs}) e^{-i\omega_{cs} t} + P(\omega_p) e^{-i\omega_p t} + P(\omega_s) e^{-i\omega_s t} + c.c. \tag{1.125}$$

where $\omega_{as} = 2\omega_p - \omega_s$, $\omega_{cs} = 2\omega_s - \omega_p$, ω_p, and ω_s. The non-linear polarization is the sum of four terms that represent the sources of different processes. The terms $P(\omega_{as})$ and $P(\omega_{cs})$ give rise to Coherent anti-Stokes Raman scattering (CARS) and Coherent Stokes Raman scattering (CSRS), respectively, while the terms $P(\omega_p)$ and $P(\omega_s)$ are the sources

of Stimulated Raman scattering. The expressions for the four polarization terms are given by:

$$\begin{aligned} P(\omega_{as}) &= N\epsilon_0\Big(\frac{\partial\alpha}{\partial x}\Big)x(\Omega)A_p e^{i(2k_p-k_s)z} \\ P(\omega_{cs}) &= N\epsilon_0\Big(\frac{\partial\alpha}{\partial x}\Big)x(\Omega)A_s e^{i(2k_s-k_p)z} \\ P(\omega_p) &= N\epsilon_0\Big(\frac{\partial\alpha}{\partial x}\Big)x(\Omega)A_s e^{ik_p z} \\ P(\omega_s) &= N\epsilon_0\Big(\frac{\partial\alpha}{\partial x}\Big)x(\Omega)A_p e^{ik_s z} \end{aligned} \tag{1.126}$$

1.4. Third-order nonlinear processes

In the previous section, we discussed another type of nonlinear effect that impacts the propagation of pulses, known as the third-order nonlinear effect. To explain this phenomenon, we need to consider the third-order polarization, as given by equation (1.19). Let us now introduce three incoming electric fields, impinging on a $\chi^{(3)}$ medium, defined as:

$$E_i(t) = A_i(t)\cos(\omega_i t + \phi_i) \qquad i = 1, 2, 3 \tag{1.127}$$

The total electric field is:

$$E(t) = A_1(t)\cos(\omega_1 t + \phi_1) + A_2(t)\cos(\omega_2 t + \phi_2) + A_3(t)\cos(\omega_3 t + \phi_3) \tag{1.128}$$

So, the third-order polarization can be calculated by substituting (1.128) in (1.19), finding:

$$P^{(3)}(t) = \epsilon_0\chi^{(3)}\Big[A_1(t)\cos(\omega_1 t + \phi_1) + A_2(t)\cos(\omega_2 t + \phi_2) + A_3(t)\cos(\omega_3 t + \phi_3)\Big]^3 \tag{1.129}$$

Performing the calculations, 22 different terms can be found oscillating at different frequencies. Oscillating, the polarization acts as a source giving rise to radiation at the same frequency. The 22 terms can be classified in the following way:

- 3 terms oscillating at ω_1, ω_2, ω_3 which give rise to the Optical Kerr effect (self-phase modulation and self-focusing).
- 3 terms oscillating at $3\omega_1$, $3\omega_2$, $3\omega_3$ which give rise to the third harmonic generation (THG) effect.
- 6 terms oscillating at $2\omega_i - \omega_j \qquad i \neq j$.
- 6 terms oscillating at $2\omega_i + \omega_j \qquad i \neq j$.

- one term oscillating at $\omega_1 + \omega_2 + \omega_3$.
- 3 terms oscillating at $\omega_i + \omega_j - \omega_k \qquad i \neq j \neq k$.

As a result, the output is a wave with a different frequency. This can be understood as a four-wave interaction. That is why third-order phenomena are also known as Four-Wave Mixing (FWM) processes.

1.4.1. Four-Wave Mixing

Let's assume four waves interacting in a $\chi^{(3)}$ medium such that $\omega_1 + \omega_3 = \omega_2 + \omega_4$. The total electric field can be written as:

$$E = \frac{1}{2}\Big[A_1(z,t)e^{i(\omega_1 t - k_1 z)} + A_2(z,t)e^{i(\omega_2 t - k_2 z)} + A_3(z,t)e^{i(\omega_3 t - k_3 z)} + A_4(z,t)e^{i(\omega_4 t - k_4 z)} + c.c.\Big] \tag{1.130}$$

where c.c. denotes the complex conjugated. The interaction of the four waves is shown in figure 1.19. In general, the polarization of the third order can be written as:

$$P^{(3)}(z,t) = \epsilon_0 \chi^{(3)} E^3 = \frac{1}{2}\Big[B(z,t)e^{i(\omega t - k_p z)} + c.c.\Big] \tag{1.131}$$

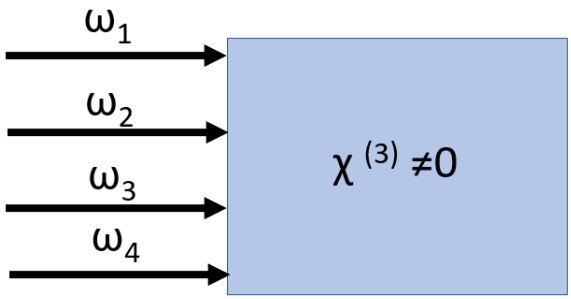

Figure 1.19: Conceptual scheme of the interaction between light and matter considering third-order non-linear processes in the four-wave mixing frame.

To find the propagation equation for the envelope A_1 we need to look at the terms of the polarization oscillating at $\omega_1 = \omega_2 + \omega_4 - \omega_3$. Substituting 1.131 in 1.4.1 we find, after some calculations, that the third-order polarization term oscillating at frequency ω_1,

namely $P^{(3)}_{\omega_1}$ reads:

$$P^{(3)}_{\omega_1}(z,t) = \frac{\epsilon_0 \chi^{(3)} 6}{8} A_2 A_4 A_3^* e^{\left[(\omega_2+\omega_4-\omega_3)t-(k_2+k_4-k_3)z\right]} + c.c. \tag{1.132}$$

We can define:

$$B_{\omega_1} = \frac{3\epsilon_0 \chi^{(3)}}{2} A_2 A_4 A_3^* \tag{1.133}$$

$$k_{p\omega_1} = k_2 + k_4 - k_3 \tag{1.134}$$

We can plug (1.133) and (1.134) in (1.81) neglecting the dispersion terms. Then, we get:

$$\frac{\partial A_1}{\partial z} + \frac{1}{v_{g1}} \frac{\partial A_1}{\partial t} = -i f_1 A_2 A_4 A_3^* e^{i\Delta k z} \tag{1.135}$$

where $f_1 \triangleq \frac{3\omega_1 \chi^{(3)}}{4cn(\omega_1)}$ and $\Delta k \triangleq k_3 + k_1 - k_2 - k_4$. The same reasoning could be applied to all the other terms oscillating at the original frequencies, obtaining:

$$\begin{cases} \dfrac{\partial A_1}{\partial z} + \dfrac{1}{v_{g1}} \dfrac{\partial A_1}{\partial t} = -i f_1 A_2 A_4 A_3^* e^{i\Delta k z} & \text{(1.136a)} \\ \dfrac{\partial A_2}{\partial z} + \dfrac{1}{v_{g2}} \dfrac{\partial A_2}{\partial t} = -i f_2 A_1 A_3 A_4^* e^{-i\Delta k z} & \text{(1.136b)} \\ \dfrac{\partial A_3}{\partial z} + \dfrac{1}{v_{g3}} \dfrac{\partial A_3}{\partial t} = -i f_3 A_2 A_4 A_1^* e^{i\Delta k z} & \text{(1.136c)} \\ \dfrac{\partial A_4}{\partial z} + \dfrac{1}{v_{g4}} \dfrac{\partial A_4}{\partial t} = -i f_4 A_1 A_3 A_2^* e^{-i\Delta k z} & \text{(1.136d)} \end{cases}$$

where $f_i \triangleq \frac{3\omega_i \chi^{(3)}}{4cn(\omega_i)}$. It is possible to observe that the set of equations (1.136) represents the propagation equation for four-wave mixing phenomena (neglecting dispersion for simplicity), which are characterized by the direct dependence on the term $\chi^{(3)}$), which will be analyzed in detail in the following.

1.4.2. The CARS process

Coherent Anti-Stokes Raman Scattering (CARS) is a powerful technique commonly used in Raman spectroscopy. This technique takes advantage of the third-order non-linearity, where two synchronized trains of laser pulses at frequency ω_s (Stokes) and ω_p (pump) resonantly excite the Raman transition at frequency $\Omega = \omega_p - \omega_s$. When the frequency mismatch matches a resonance frequency Ω_R of the scrutinized sample, all the molecules in the focal spot are resonantly excited. The vibrational mode is read by means of the

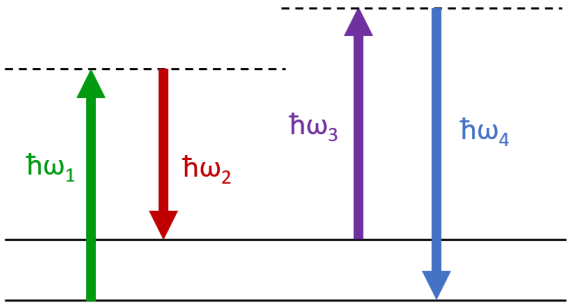

Figure 1.20: Jablonsky diagram of four-wave mixing processes.

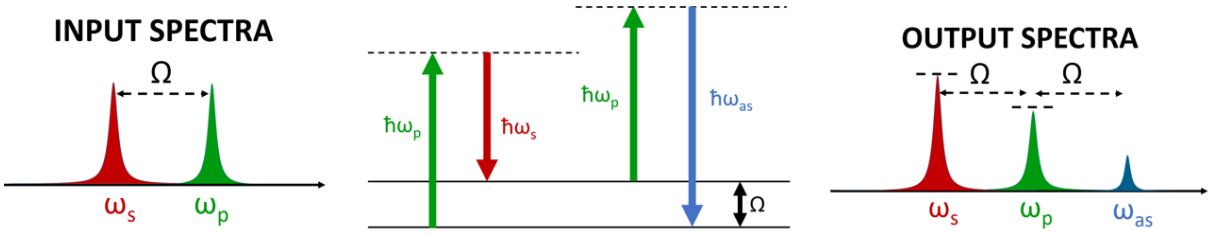

Figure 1.21: Jablonsky diagram of CARS process and the representation of the Stokes, Pump, and Anti-Stokes pulses before and after the CARS process.

interaction with a third beam, called probe beam at frequency ω_{pr}. In this configuration, the CARS signal will be emitted at the anti-Stokes frequency $\omega_{as} = \omega_p - \omega_s + \omega_{pr}$. Typically, one chooses to work with $\omega_{pr} = \omega_p$, thus working in the degenerate CARS configuration, where $\omega_{as} = 2\omega_p - \omega_s$, as depicted in figure 1.21.

We can obtain the expression of the CARS signal by applying the continuous wave approximation $\frac{\partial A_i}{\partial t} \approx 0$ to the four-wave mixing expression (1.136) which can be rewritten as:

$$\begin{cases} \dfrac{\partial A_1}{\partial z} = -i\alpha_1 \chi^{(3)} A_2 A_4 A_3^* \exp\{-i\Delta k z\} & \text{(1.137a)} \\ \dfrac{\partial A_2}{\partial z} = -i\alpha_2 \chi^{(3)} A_1 A_4 A_3^* \exp\{+i\Delta k z\} & \text{(1.137b)} \\ \dfrac{\partial A_3}{\partial z} = -i\alpha_3 \chi^{(3)} A_2 A_4 A_1^* \exp\{-i\Delta k z\} & \text{(1.137c)} \\ \dfrac{\partial A_4}{\partial z} = -i\alpha_4 \chi^{(3)} A_1 A_3 A_2^* \exp\{+i\Delta k z\} & \text{(1.137d)} \end{cases}$$

with $\alpha_i = \frac{3\omega_i}{4n(\omega_i)c_0} \quad i = 1, 2, 3, 4$. Let's now impose in (1.137) $\omega_p = \omega_1 = \omega_3$, $\omega_s = \omega_2$, $\omega_{as} = \omega_4$ and let's remember the resonant condition $\omega_1 - \omega_2 = \Omega$ that is equivalent to $\omega_{as} = \omega_p + \Omega$. Then, we can make two assumptions:

- Small signals: constant pump envelope $A_p \approx cost$ in z and constant stokes envelope

$A_s \approx cost$ in z.

- No anti-stokes signal at the sample input: $A_{as}(z=0)=0$.

Then, we have only one equation in the four-wave mixing system:

$$\frac{\partial A_{as}}{\partial z} = -i\alpha_{as}\chi^{(3)}A_p^2 A_s^* e^{i\Delta kz} \tag{1.138}$$

Now, we can integrate (1.138):

$$A_{as}(z=L) = -i\alpha_{as}\chi^{(3)}A_p^2 A_s^* + e^{i\frac{\Delta kL}{2}} sinc\Big(\frac{\Delta kL}{2}\Big)L \tag{1.139}$$

At the detector, we measure the intensity of the signal:

$$I_{CARS} \propto |A_{as}(z=L)|^2 = -\alpha_{as}^2|\chi^{(3)}|^2 I_p^2 I_s L^2 sinc^2\Big(\frac{\Delta kL}{2}\Big) \tag{1.140}$$

Equation (1.140) represents the expression of the CARS signal coming out of a medium with length L. From this expression, we can point out that:

- The signal scales quadratically on the pump intensity and linearly on the Stokes one. Therefore, increasing the pump intensity is more beneficial to enhance the signal.
- The signal scales quadratically on the width of the medium L. Thus, it is hard to extract signals from thin samples.
- Another factor that affects the CARS intensity is the square of $|\chi^{(3)}|$. In the next section, we will explain how $\chi^{(3)}$ is connected to the number of scatterers. This means that when this number is very low, the samples are barely visible because of the quadratic dependence.

A high intensity requires that the phase matching condition ΔkL is nearly zero. This can be achieved either when Δk is nearly zero or when L is nearly zero. The first case implies that: $\Delta k = 2k_p - k_s - k_{as} \approx 0$, where the wave vectors are given by: $k_p = \frac{n(\omega_p)\omega_p}{c}$, $k_s = \frac{n(\omega_s)\omega_s}{c}$, $k_{as} = \frac{n(\omega_{as})\omega_{as}}{c}$. Because of the material dispersion, the refractive index at different frequencies will be different, which means that the phase-matching condition is not met. However, under tight-focusing conditions, which are common in microscopy where high numerical aperture objectives are used, Δk is almost zero. The other case where the phase matching condition can be met is for small and thin scatterers, where $L < \lambda_p$. This is especially useful in epi-detection CARS where the anti-Stokes component is collected in reflection and where $\Delta k = 2k_p - k_s + k_{as} = 2k_{as} \neq 0$ so that only small scatterers can generate the signal. When the phase matching condition is met, we can

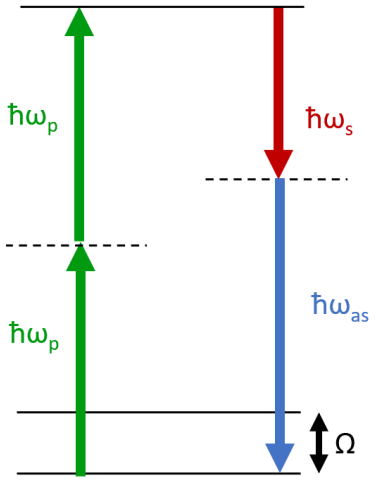

Figure 1.22: Jablonsky diagram of the non-resonant four-wave mixing.

simplify the CARS intensity expression as:

$$I_{CARS} \approx \alpha_{as}^2 |\chi^{(3)}|^2 I_p^2 I_s L^2 \tag{1.141}$$

Despite arising in a region of the spectrum different from the pump and Stokes frequency, the CARS signal suffers from an undesired non-resonant background (NRB). We can consider the generation of the anti-stokes component through the Jablonsky diagrams shown in Figure 1.22 to comprehend this phenomenon. As we can see, a signal with a frequency of $\omega_{as} = 2\omega_p - \omega_s$ is produced from a pump beam and a Stokes beam by an additional process that is distinct from the CARS process. In the CARS scenario, the electric field generated by the pump excites a molecule to a virtual level. Then, the interaction with the Stokes field excites the vibrational coherence. A second interaction with the pump field that acts as a probe brings the molecules to a virtual level, from which the molecules relax emitting an electromagnetic wave at frequency ω_{as}. This contribution is called Resonant CARS. In the second scenario, the molecules interact twice with the pump field, and then the interaction with the Stokes field will bring the molecule to a virtual level from which it relaxes emitting the anti-Stokes component. This interaction does not involve any vibrational resonance of the sample, therefore the corresponding anti-Stokes component is known as Non-Resonant CARS. Instead, it results from the immediate electronic response of the medium. This reflects on the expression of the third-order susceptibility that can be written as:

$$\chi^{(3)} = \chi_{NR}^{(3)} + \chi_R^{(3)} \tag{1.142}$$

where $\chi_R^{(3)}$ is the resonant nonlinear susceptibility given by the molecules under study and $\chi_{NR}^{(3)}$ is the nonresonant non-linear susceptibility generated both by the same molecules and by the surrounding medium through the non-resonant four-wave mixing process. $\chi_R^{(3)}$ is a complex number with an imaginary part that has a Lorentazian lineshape and a real part that has a dispersive line shape. It is the superposition of several complex Lorentzian responses related to the different vibrational transitions of the molecules, so it can be written as:

$$\chi_R^{(3)}(\omega) = \sum_i \frac{N_i \sigma_i}{\omega - \Omega_i - i\Gamma_i} \tag{1.143}$$

where N_i is the density of vibrational oscillators, σ_i is the cross-section, Ω_i the resonance frequency, and Γ_i the homogenous linewidth of the vibrational transition. While the nonresonant susceptibility $\chi_{NR}^{(3)}$ is pure real and constant.
Let's now consider the CARS signal intensity and its dependence on the square modulus of $\chi^{(3)}$:

$$I_{CARS} \propto |\chi^{(3)}|^2 = |\chi_R^{(3)} + \chi_{NR}^{(3)}|^2 = |\chi_R^{(3)}|^2 + |\chi_{NR}^{(3)}|^2 + 2\chi_{NR}^{(3)} \mathbb{R}e\left\{\chi_R^{(3)}\right\} \tag{1.144}$$

Analyzing equation (3.3), it is possible to observe that the CARS intensity is the sum of three different contributions:

- The resonant term, $|\chi_R^{(3)}|^2$, is the first term in the expression of the third-order nonlinear susceptibility. It contains the vibrational information of the molecular system. Due to this term, the CARS signal exhibits a quadratic dependence on the molecular concentration $I_{CARS} \propto N^2 + N$, which limits the detection of low molecular concentration (low sensitivity to low concentration).
- The non-resonant term corresponds to $|\chi_{NR}^{(3)}|^2$. This term is a frequency-independent contribution to the signal unless it is close to electronic resonances.
- The last term, $2\chi_{NR}^{(3)} \mathbb{R}e\left\{\chi_R^{(3)}\right\}$, arises from the interference between the resonant and non-resonant contribution giving rise to the dispersive signal distorting line shape

The interference term between the resonant and the non-resonant components causes the CARS spectrum to deviate from the Spontaneous Raman spectrum. In fact, the second and third terms of the equation (3.3) generate the so-called non-resonant background (NRB). The NRB has a dual effect on the signal: it enhances the signal intensity by providing a nearly constant offset (the second term), but it also alters the Lorentzian shape of the peaks by introducing a dispersive component (due to $\mathbb{R}e\left\{\chi_R^{(3)}\right\}$ in the third term), which shifts the peak maxima to lower frequencies and creates a dip at higher frequencies of the Raman peak. Figure 1.23 illustrates the different contributions of the

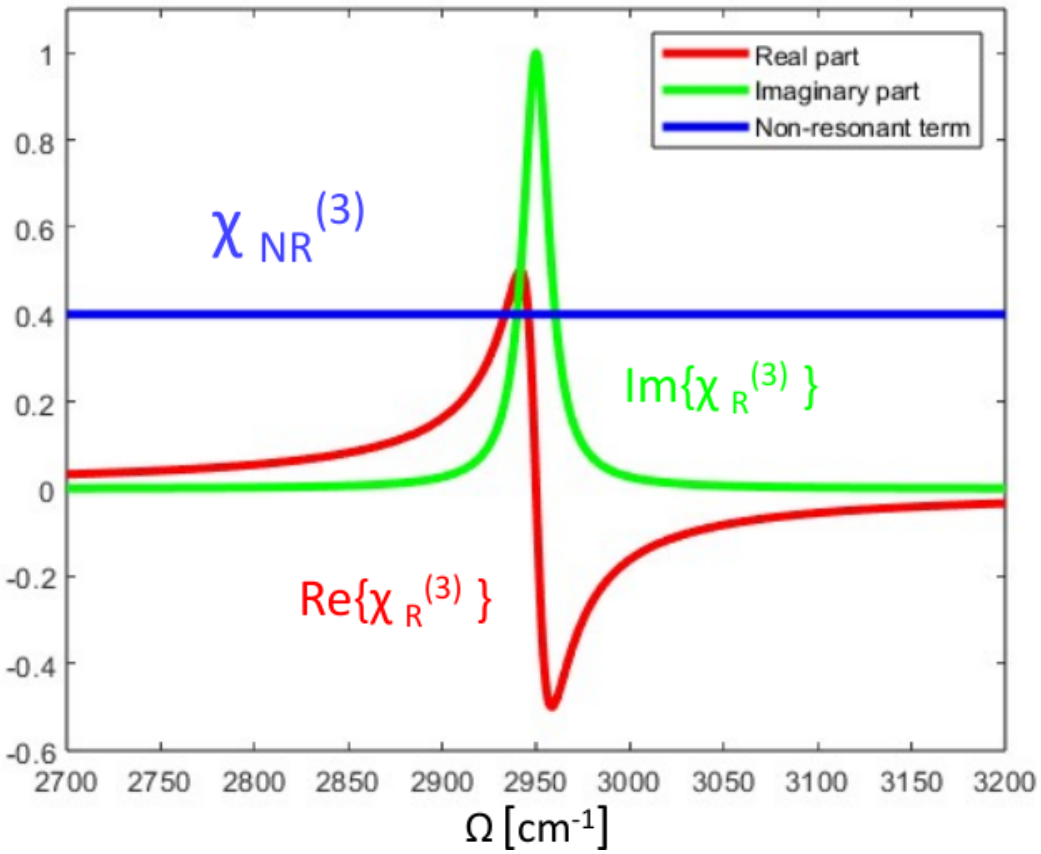

Figure 1.23: Spectral profile of the resonant and non-resonant third-order non-linear susceptibility in the CARS process.

susceptibility. By progressively decreasing the ratio of resonant to non-resonant signal, the vibrational response loses contrast and is distorted, as shown in figure 1.24. The NRB signal shows some differences with respect to the resonant one.

- At resonance, the NRB is dephased with respect to the resonant contribution.
- The resonant contribution reflects the population of a vibrational level and has a coherence time of a few picoseconds typically. The NRB, however, comes from the immediate electronic response of the medium [47], where only virtual levels are involved, so it only exists near time zero and lasts for about the same duration as the excitation pulse.

The resonant term is the only part of the CARS signal that contains information about the vibrational modes and is useful for spectroscopic applications. Therefore, it is often desirable to eliminate the NRB from the CARS signal. There are different ways to do this: either optically using polarization CARS [48], time-resolved CARS [49, 50], or Fourier-

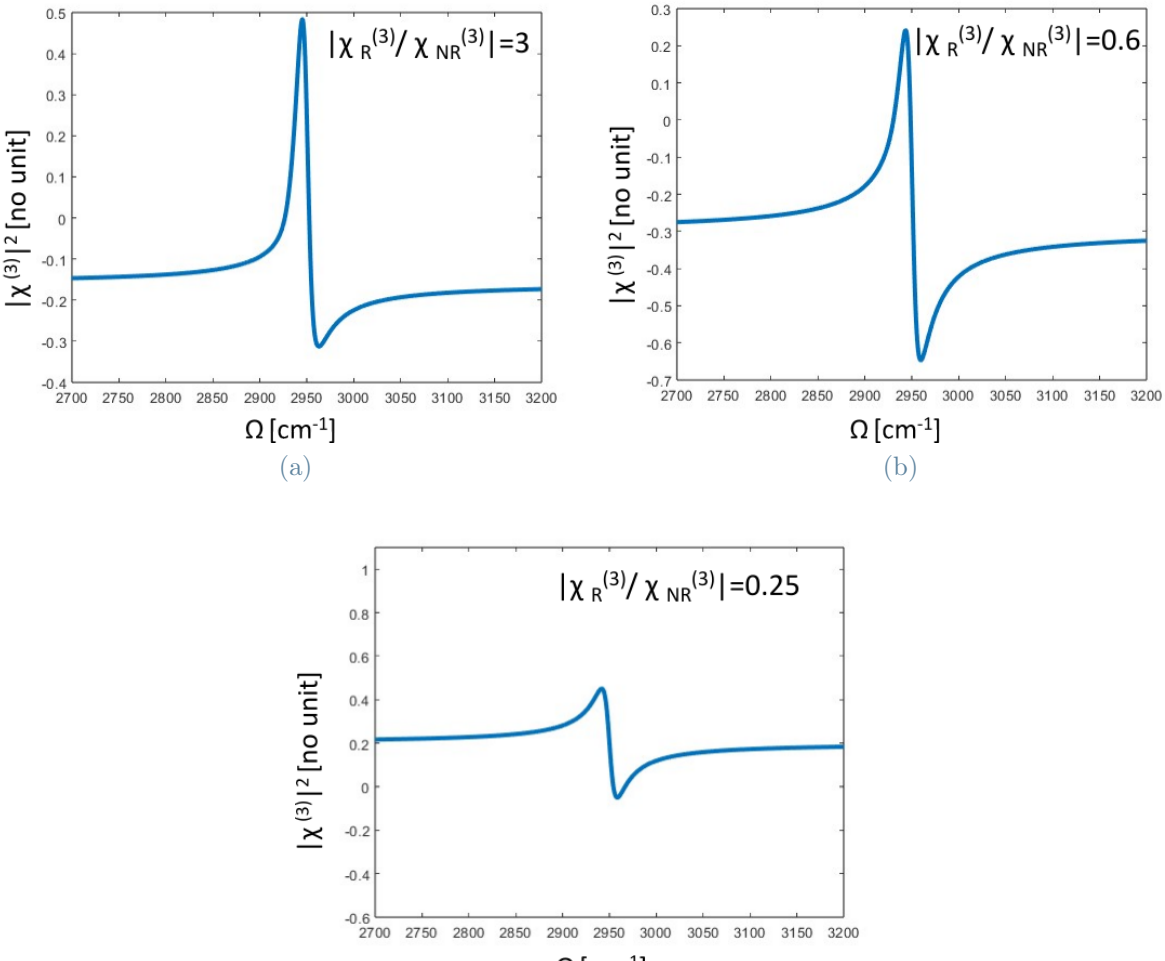

Figure 1.24: Overall third-order nonlinear susceptibility $\chi^{(3)}$ varying the ratio between the resonant and the non-resonant contributions, respectively with (a) $\frac{\chi_R^{(2)}}{\chi_{NR}^{(2)}} = 3$, (b) $\frac{\chi_R^{(2)}}{\chi_{NR}^{(2)}} = 0.6$ and (c) $\frac{\chi_R^{(2)}}{\chi_{NR}^{(2)}} = 0.25$.

transform CARS [51, 52] or in post-processing using numerical methods (Time-domain Kramers-Kronig [53] and Maximum-Entropy-Method [54]) or deep learning based methods [55–58]. In our experiments, we usually adopt the NRB removal by Kramers-Kroning. This approach will be discussed further in the next chapter.

1.4.3. Broadband CARS

The CARS process, which uses narrowband pump and Stokes beams in a single-frequency regime, can achieve high acquisition speeds up to the video rate [59]. However, this approach has limited information content since it can only probe a single vibrational transition, making it difficult to distinguish between different components in complex heterogeneous systems like cells and tissues with spectrally overlapped chemical species. Broadband CARS, on the other hand, can provide information content comparable to SR spectroscopy while maintaining high-speed acquisition. However, it requires more sophisticated technical implementations for optical source handling and generation, as well as signal detection. Various techniques can be utilized to measure the CARS spectrum, either in part or entirely for each image pixel. These techniques include Multiplex CARS, Hyperspectral CARS [60], Time-Resolved CARS [61], and Single-Beam CARS [62].
Multiplex CARS enables simultaneous acquisition of multiple vibrational frequencies, providing a broad spectrum of molecular information in a single measurement. Hyperspectral CARS extends this by capturing spectral data point by point, offering detailed molecular characterization across the entire sample. Time-resolved CARS employs precisely timed laser pulses to study dynamic processes, unraveling molecular kinetics. On the other hand, Single-Beam CARS employs a single laser beam for excitation and probing, simplifying experimental setups.

In our specific experiment, we employed the Multiplex CARS technique. This involved using a narrowband pump and a broadband Stokes pulse to generate a broadband anti-Stokes component, enabling simultaneous probing of different Raman modes. The full CARS spectrum can be detected in the frequency domain using a spectrometer. Several implementations have been proposed for multiplex CARS, including those that use a single ultra-broadband laser providing both pump and Stokes frequencies [63, 64] or combine narrowband pump pulses with broadband Stokes pulses obtained by supercontinuum generation in a tapered fiber [65] or photonic crystal fiber (PCF) [66]. Some methods are based on a time-domain Fourier transform approach [67, 68] or use frequency combs [69], while others detect the CARS signal using a simple spectrometer.
The state-of-the-art of BCARS applications can be summarized by citing three main works. Hashimoto et al. [68] demonstrated broadband CARS spectroscopy with spectral

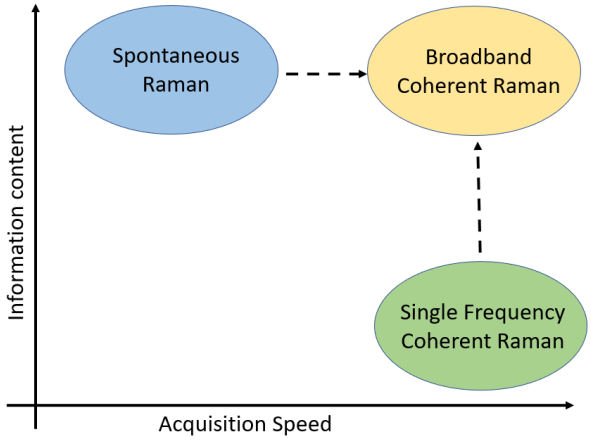

Figure 1.25: Comparison between spontaneous and coherent Raman scattering techniques in terms of imaging speed and information content. Adapted from [11].

coverage: 200–1500 cm^{-1} at a record scan rate of 24,000 spectra/s using a time-domain Fourier-transform approach, while Camp et al. [70] reported ultra-broadband multiplex CARS microspectroscopy, with spectral coverage: 500–3500 cm^{-1}, at 3.5 ms pixel exposure time when imaging biological tissues. More recently, Yoneyama et al. [71] proposed a multiplex CARS microscope, with spectral coverage: 600–3600 cm^{-1}, with exposure time down to 0.8 ms using a high-peak-power supercontinuum generated in a PCF pumped by a Q-switched microchip Nd: YVO4 laser oscillator generating sub-100-ps laser pulses at a 0.82 MHz repetition rate.
While in the narrowband CARS approach the NRB distorts the peak and cannot be removed in post-processing limiting the system sensitivity, in the broadband approach it can be exploited as a self-heterodyne amplifier of the resonant CARS signal. This allows heterodyne amplification through the term $2\chi^{(3)}_{NR}\mathbb{R}e\left\{\chi^{(3)}_{R}\right\}$ that can enhance the signal-to-noise ratio (SNR) of the measured spectra. In BCARS, line-shape distortions can be removed by using numerical methods or deep-learning approaches to extrapolate the pure vibrational information.

1.4.4. Two-color and three-color CARS

Multiplex CARS utilizes two distinct methods for generating the nonlinear signal: the "two-color" configuration and the "three-color" mechanism. In the two-color, the vibrational coherence is produced through one interaction with a narrowband pump pulse and another interaction with a broadband Stokes pulse and is subsequently detected via a further interaction with the narrowband pump, acting as a probe, which generates the anti-Stokes signal. In contrast, the three-color mechanism generates the vibrational co-

herence directly via the Impulsive Stimulated Raman Scattering (ISRS) process, whereby different frequency components of a single broadband pulse excite virtual levels and stimulate the emission down to vibrational levels of the ground state, creating a vibrational coherence in all modes whose oscillation period is comparable to or longer than the duration of the excitation laser pulse. The vibrational coherence can then be read out by interacting with the narrowband pump pulse. The excitation profile in the three-color CARS mechanism depends on the permutations of each frequency shift within the Stokes bandwidth and diminishes with increasing wavenumber, emphasizing the lower frequencies and making it particularly useful in the fingerprint region (400-1800 cm^{-1}). These two excitation methods often act in parallel, thus enabling one to collect signals in two different spectral regions simultaneously. In our experimental setup, which will be described in chapter 2, we leverage these two mechanisms to span distinct regions of the spectrum: employing the three-color mechanism enables coverage up to 1400 cm^{-1}, while the two-color mechanism effectively addresses the range between 1400 and 3200 cm^{-1}. The spectrum of toluene, obtained by harnessing both mechanisms, is depicted in the accompanying figure1.26.

The CARS signal intensity is generally proportional to the square modulus of the third-order polarizability generated by the interaction of the pump $E_p(\omega)$ and Stokes $E_s(\omega)$ electric fields at the sample. Thus, the CARS intensity can be expressed as:

$$I_{CARS} \propto |P^{(3)}(\omega_{as})|^2 \propto \left| \left\{ \chi^{(3)}[E_s(\omega) \otimes E_p(\omega)] \right\} * E_p(\omega) \right|^2 \tag{1.145}$$

here the cross-correlation operation represented by $\otimes$ is responsible for exciting vibrational modes with frequencies matching the difference between pump and Stokes frequencies. The convolution operation represented by $*$ with the narrowband pump field defines the spectral resolution of the system, assuming that the cross-correlation is broad enough. Equation 1.145 defines the two-color mechanism. However, if the broadband Stokes beam is short enough (shorter than the vibrational oscillation period), an intra-pulse ISRS or three-color excitation mechanism occurs at the sample plane. In this mechanism, the narrowband pump beam acts as a probe after excitation, determining the final emission at the anti-Stokes frequencies. Equation 1.145 is modified as:

$$I_{CARS} \propto |P^{(3)}(\omega_{as})|^2 \propto \left| \left\{ \chi^{(3)}[E_s(\omega) \otimes E_s(\omega)] \right\} * E_p(\omega) \right|^2 \tag{1.146}$$

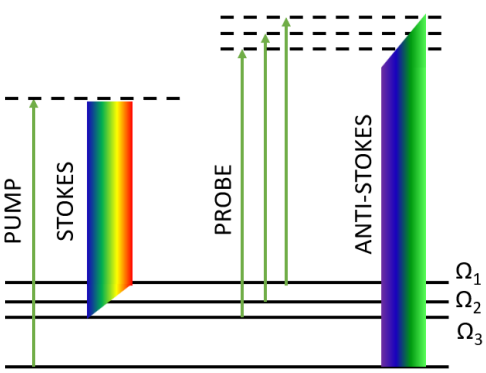

(a) Two-color CARS.

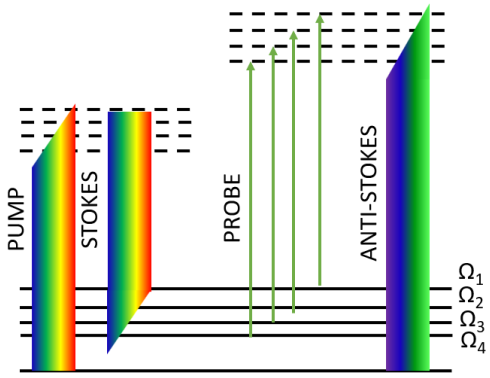

(b) Three-color CARS.

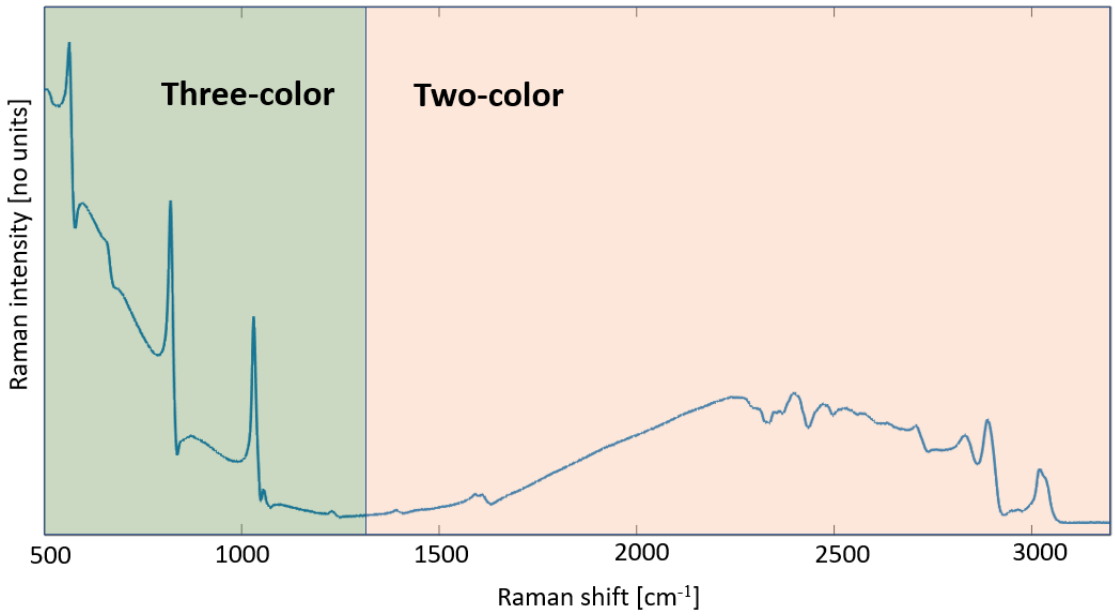

(c) CARS spectrum

Figure 1.26: The Jablonsky diagrams of Two-color CARS and Three-color CARS are depicted in (a) and (b) respectively. A CARS spectrum of toluene, acquired with 1-ms exposure time between two quartz coverslips, is shown in (c) to highlight the Two-color and Three-color regions.

In summation, the current chapter engages in a thorough and comprehensive elucidation of the fundamental mechanisms that form the bedrock for our measurements, encompassing phenomena such as BCARS and SHG. The subsequent chapter will delve into a meticulous analysis of the experimental configuration that underpins the foundational framework of this thesis. This exposition will encompass a precise delineation of the constituent elements and enhancements that I have implemented. Moreover, a concise yet scholarly presentation of Supercontinuum generation within bulk media will be offered.

2 | Experimental Setup

In this chapter, I present the experimental setup utilized for conducting BCARS measurements.

My thesis focuses on an existing experimental BCARS setup that has been previously utilized in other publications [72, 73]. My distinct contribution involves the enhancement of the software component related to data acquisition and analysis. Additionally, I extended the capabilities of the setup by incorporating a SHG channel. This enhancement has transformed the configuration into a multimodal microscope, thus enabling a more elaborate and holistic chemical analysis of the examined specimens due to the concurrent acquisition of both BCARS and SHG signals.

The BCARS experimental setup comprises three primary components: the light sources, the microscope, and the detection. The schematic representation of the setup can be observed in Figure 2.1.

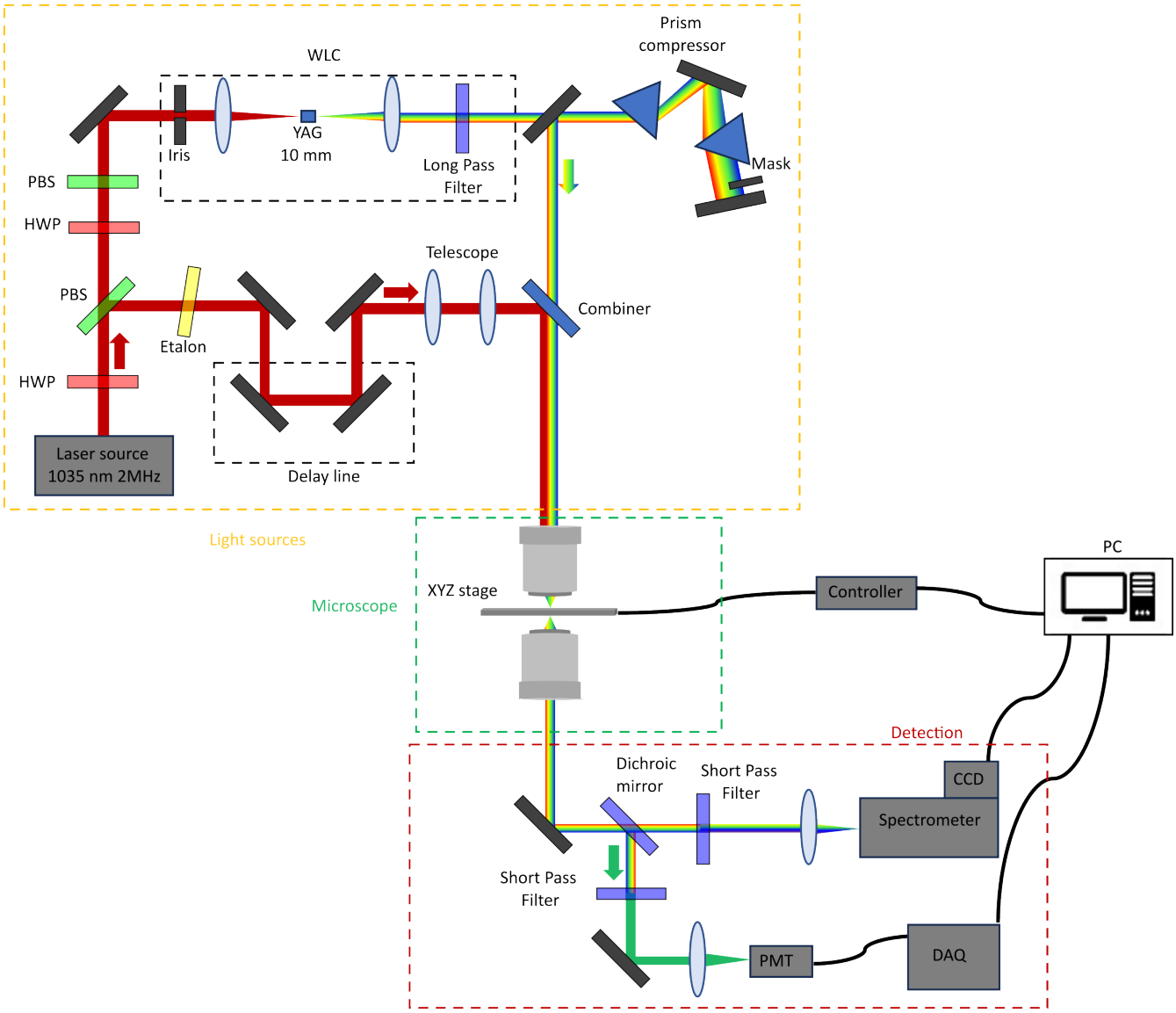

Figure 2.1: The figure presents an illustration of the experimental setup that I used for the measurements presented in this thesis, highlighting the main components. The propagation of the pump beam is represented by the red path, while the rainbow path indicates the propagation of the Stokes beam. Additionally, the green path illustrates the path of the SHG signal.

2.1. Light sources

The system starts with a commercially available fiber-based ytterbium laser system (Monaco 1035, Coherent) that delivers pulses of approximately 270 femtoseconds duration with a spectral bandwidth of 10 nm, centered at a wavelength of $\lambda_0 = 1035$ nm. The laser system offers adjustable repetition rates ranging from 1 to 50 MHz and a maximum average

power of 60 W. For our experiment, we set the repetition rate at 2 MHz and the average power at approximately 6 W. The laser output is divided into two branches using a polarizing beam splitter (PBS). The average power of the two beams can be controlled by a half-wave plate (HWP) mounted on a manual rotational stage.

The first beam replica, with an average power of approximately 2 W, passes through a high-finesse Fabry–Perot etalon (air-space etalon, SLS Optics). This etalon narrows down the spectral bandwidth, resulting in the generation of narrowband pump pulses. The narrowband pump beam exhibits an FWHM of approximately 0.9 nm, which, for a wavelength of $\lambda_0 = 1035$ nm, corresponds to a bandwidth of approximately $<9\ cm^{-1}$ in wavenumbers. This narrowband pump pulse is crucial to achieve the desired spectral resolution in the CARS spectra, matching the typical linewidths of vibrational Lorentzian peaks in condensed media [74]. It is worth noting that a narrowband pump pulse leads to an increased pulse duration due to the Fourier principle. However, maintaining a pulse duration on the order of 1 picosecond is important to ensure an impulsive excitation of the beam.

The second beam replica, with an average power of approximately 4 W, is employed to generate a White-Light Continuum (WLC) in a 10 mm YAG crystal. This WLC serves as the broadband Stokes pulse. In order to achieve WLC, the replica beam passes through another HWP-PBS system, enabling fine-tuning of the intensity incident on the crystal. An iris is utilized to control the beam's divergence, after which it is focused by a 75 mm lens onto the 10-mm-thick YAG crystal. The crystal is mounted on a single-axis translational stage. Subsequently, a second 75 mm lens collimates the beam without altering the spot size. To select the red-shifted lobe of the Supercontinuum (SC) (ranging from 1050 nm to 1600 nm) while filtering out the fundamental beam and the blue-shifted components, a long-pass filter (LP1050, Thorlabs) is employed. The chirp of the broadband beam induced by its propagation through the optical path and the objectives is compensated by an SF11 prism pair compressor with an apex-to-apex distance of 60 cm. To finely adjust the bandwidth of the Stokes beam, a homemade mask is placed after the second prism of the compressor, allowing all colors to propagate in parallel. The generated Stokes pulses exhibit a sub-20 femtosecond pulse duration at the sample plane, after passing through the illumination objective, and possess a bandwidth spanning from 1200 nm to 1600 nm, adjustable depending on the desired excitation mechanism and application.

The spatiotemporal overlap between the two pulse trains is achieved by finely adjusting a dichroic mirror (Di02-R1064-25x36, Semrock) and employing a manual delay line mounted on the pump beam path.

2.2. Microscope

After the generation module, we employ an upright confocal microscope configuration for our experimental setup. The microscope consists of a home-built design, where the two beams enter the system. The beams are combined using a dichroic mirror (Di02-R1064-25x36, Semrock), and a pair of 100x air objectives with high Numerical Aperture (NA) (Olympus LCPLN100XIR, NA=0.85) is utilized to collinearly focus the two beams onto the sample plane and collimate the transmitted BCARS beam. These objectives are mounted on separate XYZ manual stages, allowing precise positioning.
To achieve a proper match between the spot size of the two beams and the size of the back aperture of the illumination objective, a telescope configuration is employed. This is crucial to prevent power loss before reaching the sample and to avoid reducing the effective NA of the employed objective, which would compromise the spatial resolution of the acquired images. The telescope reduces the beam size of the pump beam, which slightly diverges after propagating over several meters on the optical table.
Sample scanning is accomplished using two translational stages: the PI-nano XYZ stage (P-545.3R8S, Physik Instrumente) and an XY motorized translation stage (U-780.DNS, Physik Instrumente), stacked on top of each other. The former allows fine adjustment of the sample position in the X, Y, and Z directions, enabling movement over a range of 200 µm along all three axes. The latter is used for raster scanning of the sample over larger areas, up to approximately 2x2 cm^2 (limited by the presence of the collection objectives that may collide with the stage). By combining these two translation stages, the sample image can be acquired using a raster scanning approach.
Additionally, the microscope is equipped with a bright-field microscopy system to visualize the field of view that needs to be imaged using BCARS. A LED serves as the light source, and a lens configuration, consisting of two objectives and another lens, creates a pseudo-Kohler illumination system. Finally, a camera (Thorcam, Thorlabs), positioned in the image plane, allows us to capture wide-field images of the sample. The schematic representation of the pseudo-Kohler illumination configuration is shown in Figure 2.2 2.1.

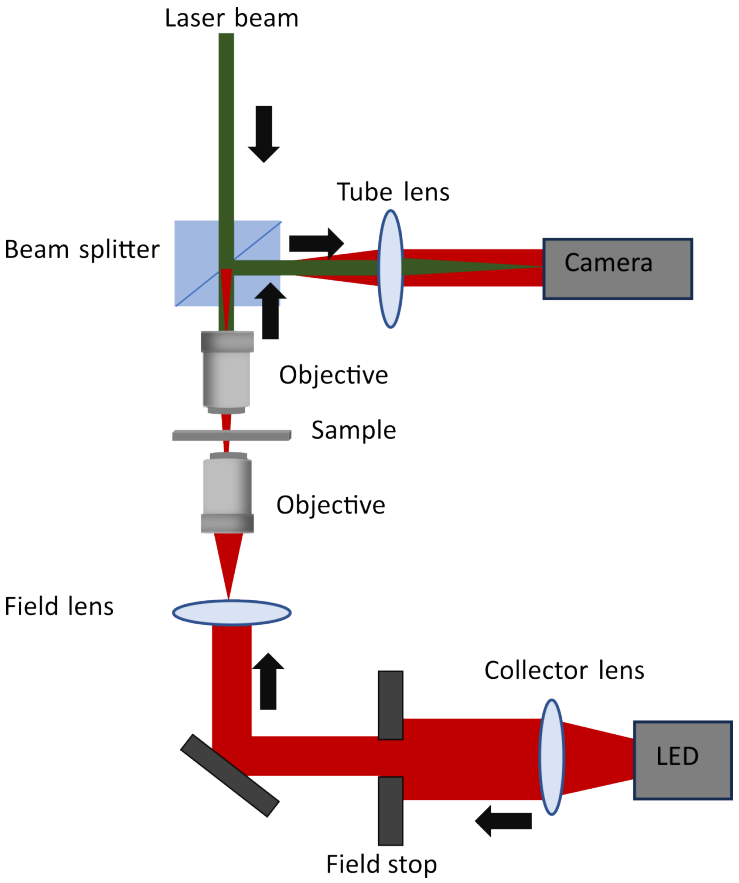

Figure 2.2: Schematic representation of the pseudo-Kohler illumination configuration implemented in the BCARS microscope. The LED light source is depicted in red, providing illumination. The laser beams, including the pump and Stokes beams, are represented in green.

2.3. Detection

After passing through the microscope, the BCARS signal enters the final component of the setup, namely the detection module, which is responsible for detecting the BCARS signal. Initially, the signal is focused onto the detection system, specifically the slit aperture of the spectrometer, using a 35 mm focusing lens (Acton SP2150p, Princeton Instruments). This lens ensures proper collection of the anti-Stokes light directed towards the spectrometer.

Before entering the spectrometer, the collimated beam, carrying the BCARS signal corresponding to the illuminated pixel, passes through a short-pass filter (SP1000, Thorlabs), which selectively transmits wavelengths below 1000 nm. This filter effectively blocks the pump and Stokes pulses while allowing the BCARS signal, centered at shorter wavelengths, to pass through. This spectral filtering ensures that the desired BCARS signal

is isolated for detection.
The detection module comprises a spectrometer equipped with 600 grooves/mm grating (AC-TON SP2150, Princeton Instruments), which effectively separates the different wavelengths of the BCARS signal. Accompanying the spectrometer is a back-illuminated deep depletion CCD camera (BLAZE100HR, Princeton Instruments), facilitating the achievement of a spectral resolution of 0.47 nm, corresponding to 5.8 cm^{-1}. The detection system is synchronized with the scanning stage through a custom-written MATLAB interface (Figure 2.3), enabling the collection of hyperspectral images. This setup allows for sample scanning along the X-Y, X-Z, and Y-Z directions.
To achieve high-speed imaging in a raster scanning fashion, the sample is positioned on a stepper motor controller that moves at a constant speed along one axis, generating a trigger signal. The MATLAB interface generates a trigger at each pixel step size. Simultaneously, the CCD camera acquires a CARS spectrum at each trigger event, utilizing binning over 100 rows and providing 1340 spectral points. This procedure is repeated for multiple pixels, resulting in a hyperspectral image. Each image is represented by a three-dimensional matrix (N $\times$ M $\times$ 1340), where the first two dimensions represent the spatial axes, and the third dimension represents the spectral points.
By employing this approach, it becomes possible to acquire images at very high speeds, utilizing the minimum exposure time allowed by the CCD camera which is 0.8 ms. Moreover, each pixel can be associated with a specific spatial position, without encountering any motion artifacts or shifts in the rows of the acquired images.
To convert the outlined experimental configuration into a multimodal microscope with the capability to concurrently capture BCARS and SHG signals, I implemented a series of modifications in both the hardware and software domains.
From a hardware perspective, I introduced a series of alterations to the setup. To acquire the SHG signal primarily from the pump but also from the Stokes after passing through the sample, I mounted a dichroic filter (FF757-DI01, Thorlabs) after the microscope. The dichroic filter allows the transmission of the BCARS signal toward the spectrometer while reflecting the SHG signals of both the pump and the Stokes. To prevent any residual pump and Stokes signals from being reflected, I used a short-pass filter, after the dichroic filter, in order to selectively transmit wavelengths below 800 nm.
Then, in the detection module, I installed a Photosensor Module equipped with a Photomultiplier Tube Module (PMT, H10721-110, Hamamatsu) to effectively capture the transmitted light. Then, I connected the PMT module, after passing through a transimpedance used to integrate the signal, to a Data Acquisition (DAQ) system (NI USB-6341), enabling the acquisition of the SHG signals from the sample under investigation.
For the acquisition of the BCARS image, a CCD camera is employed. This selection

is motivated by the capacity of the CCD to capture high-resolution images while maintaining a low noise profile. In contrast, the acquisition of the SHG signal necessitates the utilization of a PMT. The discerning deployment of a PMT stems from its inherent capability to exhibit heightened sensitivity at the level of individual photons, thereby facilitating the acquisition of signals characterized by low-intensity photon emissions.
From a software perspective, I developed a Matlab code designed to orchestrate the data acquisition process. This code enables the DAQ system to discreetly capture the signal obtained from the PMT in the background. However, the captured signal is stored solely when the MATLAB interface, responsible for BCARS signal acquisition, generates a trigger corresponding to the translation of the stepper motor of pixel step size. Simultaneously, the CCD camera is configured to capture the CARS spectrum at each trigger event, while the DAQ system concurrently records the SHG signal. This synchronized workflow results in the creation of two distinct maps of the identical sample region, each highlighting different signals.
This experimental configuration enables the efficient and synchronized acquisition of both SHG and BCARS signals. Both CCD and the DAQ system are utilized to simultaneously capture these signals, with their acquisition triggered by the stepper motor. The key distinction lies in the operational mode of the DAQ system, which functions in the background.

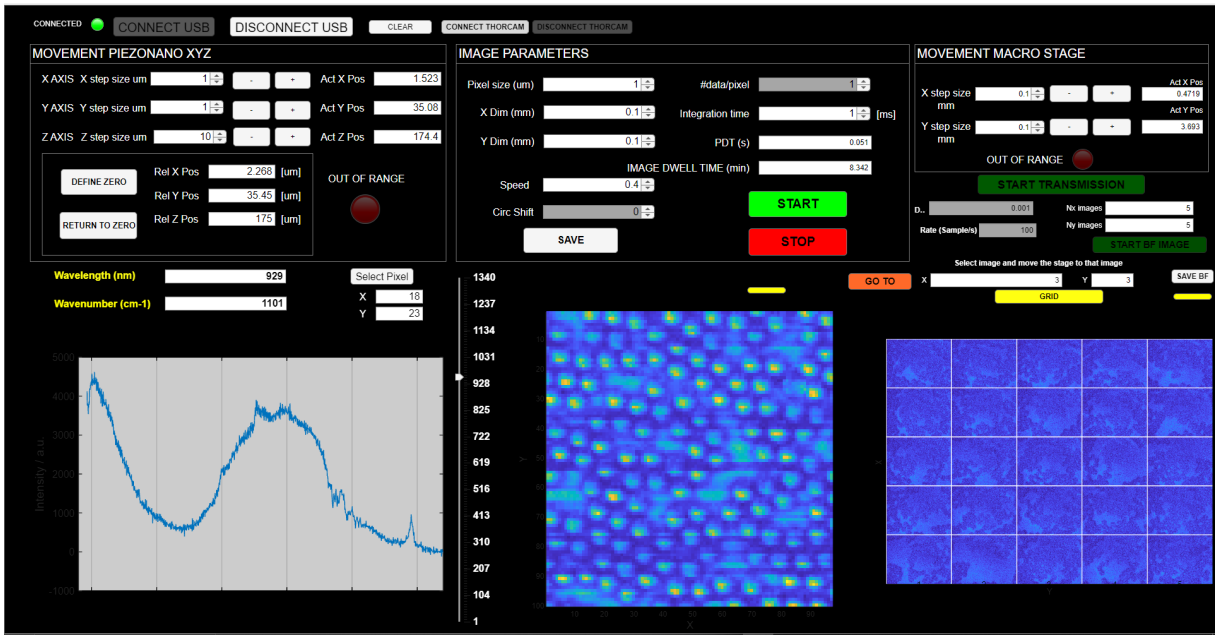

Figure 2.3: Matlab interface for the acquisition of the CARS images.

2.4. Supercontinuum generation in bulk media

This section provides a theoretical description of the processes involved in the generation of white light continuum (WLC) within the BCARS experimental setup, which serves as a broadband source.

When a high-intensity pulse propagates through a transparent medium, multiple simultaneous nonlinear processes are stimulated, resulting in a complex interplay between spatial and temporal effects and leading to a significant spectral broadening. The first phenomenon that emerges during nonlinear propagation is known as Self-Phase Modulation (SPM).

After propagating through a nonlinear medium for a distance z, the pulse envelope A can be described as:

$$A(z,t) = A(0,t)e^{-i\alpha\gamma|A(0,t)|^2} \tag{2.1}$$

Here, γ is defined as $\gamma \triangleq \frac{3\omega_0\chi^{(3)}}{8cn(\omega_0)}$.

Therefore, the electric field can be expressed in general as:

$$E(z,t) = \mathbb{R}e\Big\{A(0,t)e^{i\Phi(z,t)}\Big\} \tag{2.2}$$

where $\Phi(z,t)$ is a phase term that depends on the pulse envelope itself.

By calculating the instantaneous frequency, we find:

$$\omega(t) = \frac{\partial\Phi}{\partial t} = \omega_0 - \gamma z\frac{\partial|A(0,t)|^2}{\partial t} \tag{2.3}$$

This reveals that new frequencies are generated during propagation due to self-phase modulation, causing the pulse to become chirped. Specifically:

- For $t > 0$, $\omega > \omega_0$
- For $t < 0$, $\omega < \omega_0$

Consequently, the pulse exhibits positive chirping, with the red color arriving before the blue color. As propagation occurs, new frequencies are generated, causing the spectrum to broaden significantly compared to its initial state. Additionally, interference patterns may emerge as the same frequencies are generated at different times. Each color can contribute to interference, leading to spectrum modulation.

Another observed process during pulse propagation in a nonlinear medium is the self-focusing effect. This effect arises due to the Kerr effect in a $\chi^{(3)}$ medium, where the

effective refractive index experienced by the pulse can be expressed as:

$$n \approx n_0 + n_2 I \tag{2.4}$$

Here, n_0 represents the unperturbed refractive index, $n_2 \triangleq \frac{3\chi^{(3)}}{4c\epsilon_0 n_0^2}$, and I denotes the pulse intensity. Typically, the intensity I is a function of both time and space.
Consider a real-world light beam with a finite transverse cross-section. For our discussion, we focus on a cylindrical-symmetric beam with a radial dependence on the intensity $I(r, z)$. Consequently, we observe a radial modulation of the refractive index of the medium, given by:

$$n(r) = n_0 + n_2 I(r, z) \tag{2.5}$$

The accumulated phase of the beam during propagation is:

$$\phi(r, z) = k_0 n(r, z) z = k_0 z[n_0 + n_2 I(r, z)] \tag{2.6}$$

This introduces a spatial self-action of the light beam, resembling a lensing effect, where the beam is focused due to a higher accumulated phase in the center compared to the periphery. Consequently, this process is referred to as self-focusing.
It is worth noting that the self-focusing process involves positive feedback, where the intensity of the beam amplifies with focusing, leading to increasingly severe self-focusing. However, when the beam's cross-section becomes too small, the formation of plasma through ionization prevents a catastrophic collapse of the beam. This is due to the plasma-defocusing effect, where the plasma introduces an additional modulation of the refractive index, causing the beam to defocus. Consequently, a balance is achieved between self-focusing and self-defocusing, resulting in optical filamentation. In this regime of ultrashort pulse propagation, the cross-section of the beam remains constant over long distances.
To further explain the generation of plasma and its defocusing effect, let's consider a scenario where a plane wave propagates through a medium containing plasma. In this case, we can assume that the medium is dilute and only the electrons are in motion, while the ions remain relatively stationary. This approximation, known as the Born-Oppenheimer approximation, is valid as electrons, being much lighter than ions, move significantly faster for the same electric field.
Starting from the propagation equation and considering the plane wave approximation, we have:

$$\frac{\partial^2 E}{\partial z^2} - \frac{1}{c^2}\frac{\partial^2 E}{\partial t^2} = \mu_0 \frac{\partial J}{\partial t} \tag{2.7}$$

Here, the conduction current can be expressed as:

$$J = -eN_eV_e \tag{2.8}$$

where $e = 1.6 \times 10^{-19}, C$ represents the absolute value of the electron charge, N_e is the electron density in the medium, and V_e is the electron velocity. Assuming a constant N_e, we can calculate the time derivative of the conduction current as:

$$\frac{\partial J}{\partial t} = -eN_e\frac{\partial V_e}{\partial t} = -eN_ea_e \tag{2.9}$$

Here, a_e denotes the electron acceleration, which can be expressed as $a_e = -\frac{eE}{m_e}$. Substituting Equation 2.9 into Equation 2.10 and applying the Fourier transform, we obtain:

The equation describing the propagation of the electric field in the presence of plasma can be expressed as:

$$\frac{\partial^2\tilde{E}}{\partial z^2} + \frac{\omega^2 - \omega_p^2}{c^2}\tilde{E} = 0 \tag{2.10}$$

Here, $\tilde{E}$ represents the Fourier transform of the electric field, ω is the angular frequency, and ω_p is known as the plasma frequency, defined as $\omega_p^2 = \frac{e^2N_e}{\epsilon_0 m_e}$.

According to the Helmholtz equation, the refractive index in a plasma can be expressed as:

$$n_p = \sqrt{1 - \frac{\omega_p^2}{\omega}} \tag{2.11}$$

In this equation, n_p represents the refractive index of the plasma, ω_p is the plasma frequency, and ω is the angular frequency of the electromagnetic wave.
So far, our analysis has focused on plane waves propagating through a medium with a constant density of free electrons N_e. Now, we would like to extend our reasoning to the propagation of pulses, taking into account the time dependence of the free-electron density. In doing so, we will make four approximations:

- We consider only the contribution of electrons to the current J.
- We assume that there is only one ionization event per atom/molecule.
- The ionized electron is born in the continuum at rest.

- There is no interaction between the ionized electron and the ions.

Remarkably, it can be proven that even under these approximations, Equation 2.9 remains valid if we replace the fixed electron density N_e with $n_e(t)$, defined as:

$$n_e(t) = N\left[1 - e^{-\int_{-\infty}^{t} w(t')dt'}\right] \tag{2.12}$$

in the equation mentioned, $n_e(t)$ represents the time-dependent electron density, where N is a constant associated with the average electron density. The integral term in the equation accounts for the cumulative effect of ionization over time. The function $w(t)$ denotes the ionization rate, representing the rate at which ionization occurs at different times during the pulse propagation. By incorporating the ionization rate, we can accurately describe the time-dependent behavior of the electron density in the medium.
By considering the time-dependent electron density, we can express the refractive index in the presence of plasma as:

$$n_p = \sqrt{1 - \frac{\omega_{pp}^2}{\omega}} \tag{2.13}$$

Here, $\omega_{pp}^2 = \frac{e^2 n_e(t)}{\epsilon_0 m_e}$ represents the square of the plasma frequency.
Indeed, due to the ionization of electrons caused by the higher intensity at the center of the pulse, the refractive index in the center region becomes smaller compared to the periphery. This leads to the plasma acting as a defocusing lens, where the accumulated phase in the center of the pulse is lower than that at the periphery. As a result, the plasma-induced defocusing effect counteracts the self-focusing of the pulse, contributing to the balance between self-focusing and self-defocusing. This interplay between self-focusing and plasma-induced defocusing is crucial in understanding the dynamics of the pulse and its spatial characteristics during propagation.
In conclusion, when a high-intensity pulse propagates through a transparent medium, a combination of stimulated processes occurs simultaneously, resulting in a complex interplay between spatial and temporal effects. This leads to a significant spectral broadening while preserving the spatial characteristics of the pulse. This phenomenon is known as Supercontinuum (SC) generation in bulk materials.
The physical understanding of SC generation in transparent bulk media can be framed within the concept of optical filamentation. Optical filamentation arises from the interplay between self-focusing, SPM, and the generation of free electron plasma through multiphoton absorption/ionization. Specifically, the self-focusing induced by the Kerr effect is counteracted by the defocusing effect caused by the pulse propagating through the

plasma, which is generated by the pulse itself.
This interplay between self-focusing and plasma-induced defocusing results in the formation of a stable structure known as an optical filament. Optical filaments can propagate over extended distances that are much larger than the typical diffraction length while maintaining a narrow beam size, without the need for any external guiding mechanism. The presence of optical filaments enables the generation of a supercontinuum that spans a broad spectral range and possesses unique characteristics for various applications in photonics and nonlinear optics.

3 | Acquisition and processing of the CARS data

This section will outline the methodology employed for acquiring BCARS signals and extracting relevant information from them. Our experiments typically involve both spectroscopic and microscopic analyses. In the former, I acquire one or more spectra of the same chemical analytes, while in the latter, I collect hyperspectral data comprising three-dimensional cubes with both spatial and spectral information.
This chapter is organized into three main parts. In the first part, I provide a detailed description of the procedures and strategies used to acquire high-quality BCARS data. In the second part, I discuss the post-processing of BCARS data, including noise reduction and non-resonant background (NRB) removal. Finally, in the last section, I describe the different approaches I adopt to analyze our processed data, particularly in distinguishing between different chemical constituents when imaging heterogeneous samples.

3.1. Acquisition of BCARS data

In order to acquire BCARS data with high signal quality, it is crucial to align the experimental setup by optimizing spatial and temporal overlap of optical sources at the sample plane and aligning the anti-Stokes component to the spectrometer. The stability of the broadband source is also important, and adjustments may need to be made to impinging power, iris aperture, and crystal position relative to the focal plane.
Before collecting the data of the sample material, it is necessary to calibrate the wavenumber axis. To calibrate the wavenumber axis, the spectrum of toluene is acquired due to its numerous peaks in the fingerprint and CH-stretching regions. 100 μL of toluene is placed between two quartz coverslips, and 100 toluene CARS spectra, 100 NRB spectra, and 100 dark spectra are collected with a 1 ms exposure time. The NRB signal is measured by focusing the pump and Stokes beams on the quartz coverslip. After averaging the spectra and subtracting the NRB from the CARS spectrum using the time-domain Kramers-Kronig algorithm, a third-order polynomial function is fitted between the mea-

sured and spontaneous Raman peak positions of the eight main Raman peaks of toluene. The wavenumber axis is calibrated by fitting this function. To assess the efficacy of the calibration process, the errors between the positions of the eight peaks observed in the phase-retrieved and SR spectra are calculated. The calibration process is depicted in Figure 3.1, which showcases the various signals employed, such as the averaged CARS and NRB spectra in the top panel, the CARS spectrum with a balanced wavenumber axis and labeled peaks in the second panel, the SR spectrum in the third panel, and the corresponding errors in cm^{-1} for each peak in the bottom panel.

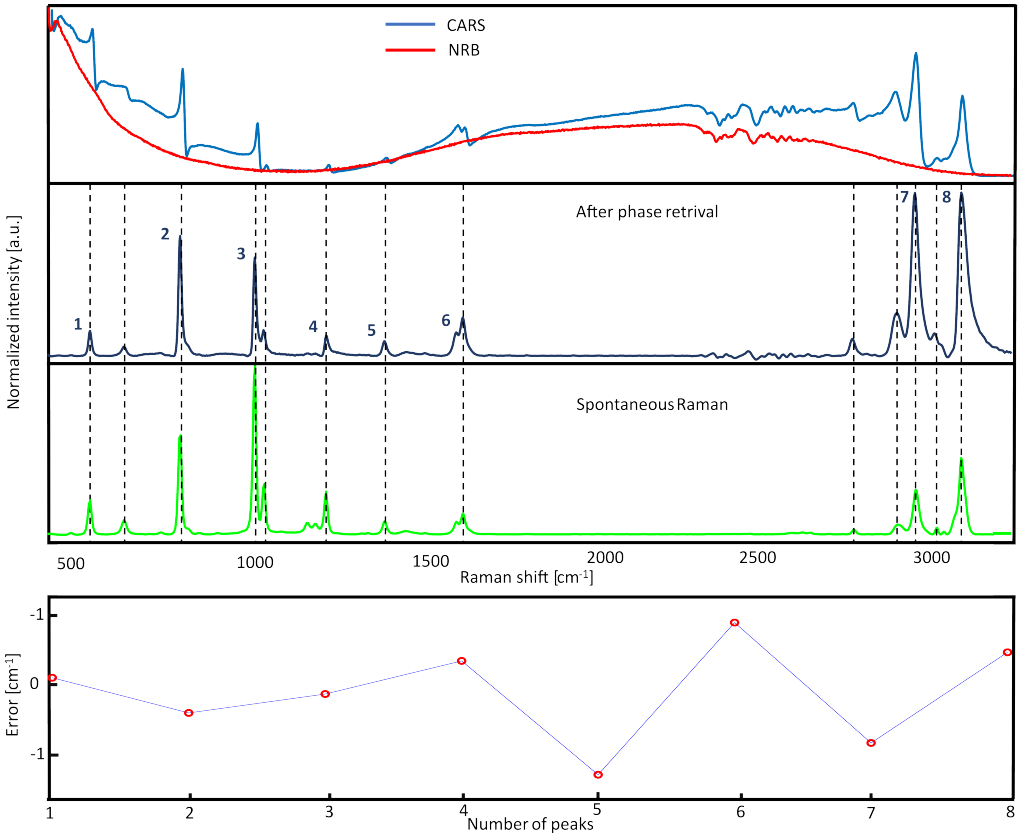

Figure 3.1: The presented figure showcases a comparison of various signals obtained during the calibration of the wavenumber axis. The blue and red curves correspond to the average CARS spectra of toluene and the average NRB, respectively. The CARS spectrum after phase retrieval is depicted by the dark blue curve, and the green curve represents the Spontaneous Raman spectrum. A third-order polynomial fitting is applied to compare eight selected peaks in the phase-retrieved spectrum with their corresponding peaks in the Spontaneous Raman spectrum, thereby obtaining a new wavenumber axis. The accuracy of the calibration procedure is evaluated by quantifying the error between the positions of the spectral peaks in the Spontaneous Raman spectrum and those in the calibrated phase-retrieved spectrum.

After performing the necessary calibration and alignment of the experimental setup, the sample preparation procedure commences. The next step involves identifying the region of interest within the sample. While in spectroscopic applications, the identification of the region of interest can be bypassed since only the sample spectrum is of interest, imaging applications require pinpointing the optimal position to measure the sample and determining the most suitable parameters for highlighting morphological features.
To achieve this, a bright-field image is generated using pseudo-Kohler illumination. This technique enables the analysis to be focused on the region of interest, resulting in enhanced visualization of morphological details. The generated image is then employed to extract crucial parameters such as the pixel size and image size, which are essential for ensuring accurate data analysis and interpretation.
After appropriately preparing the sample and identifying the region of interest, measurements can begin. However, to ensure high-quality measurements, the results must be continuously monitored during acquisition. This allows for real-time adjustments to be made to parameters such as pump or Stokes power, in cases where the intensity in certain pixels is too high and causes saturation of the CCD camera. Additionally, the pixel dwell time can be optimized to ensure optimal measurements. If the detected area contains no relevant information, or if a broader field of view is desired, the field of view can also be adjusted accordingly.
After obtaining satisfactory measurements and removing any data that clearly lacks quality, the results are saved for further processing. In the post-processing step, the collected data undergoes noise reduction and Non-Resonant Background removal before undergoing chemical analysis. Ensuring the quality of the measurements and the accuracy of the post-processing analysis is crucial to maintaining the validity and reliability of the results obtained. Paying proper attention to these steps can lead to deeper insights and a more comprehensive understanding of the sample being studied.

3.2. Data processing

The BCARS data obtained can be affected by various artifacts such as those caused by the instrumentation, sample characteristics, noise, fluctuations of the laser source, and distortion introduced by the NRB. To ensure the accuracy and reliability of the data, a procedure is followed to retrieve pure vibrational information while eliminating unwanted contributions. Additionally, a spectral unmixing algorithm is used to locate different chemical species in heterogeneous samples. In this section, I describe the procedure and algorithm used to achieve these goals.

3.2.1. Spatial denoising

After conducting an initial quality assessment, measurements that exhibit clear indications of poor quality, artifacts, or fail to detect the region of interest are discarded. Additionally, measurements with excessively high levels of noise are also excluded. Subsequently, upon selecting the desired images, a preliminary spatial denoising technique is applied to improve the quality of the image. This denoising method is based on the Fourier Transform of the image.

The proposed technique involves the utilization of the Fourier Transform to address the presence of vertical and horizontal stripes in acquired images. These stripes are typically caused by laser fluctuations, instrumental factors, and the raster scanning detection approach employed during image acquisition on the sample stage. By performing the Fourier transform on the original image, these undesired stripes, which manifest as vertical and horizontal lines passing through the center of the Fourier plane, can be effectively mitigated.

To reduce noise, a selective removal process is applied to the corresponding lines in the Fourier space, while preserving the central region of the Fourier space that retains the main information of the sample. This Fourier filtering methodology involves masking specific regions of the Fourier space of an image, followed by applying the inverse Fourier transform to obtain the denoised version. The objective of this selective removal is to minimize information loss and reduce noise as much as possible. To address the removal of these lines, the masked pixels in the Fourier domain are substituted with the mean value of adjacent pixels. This replacement helps to mitigate potential artifacts and the absence of spatial frequencies in the reconstructed images that may arise from the removal of certain pixels in the Fourier space.

To illustrate the efficacy of this method, I present Figure 3.2a, showcasing the integrated BCARS image of HeK293 cells. Initially, the image exhibits unwanted vertical and horizontal stripes, as depicted. In Figure 3.2c, the Fourier transform of the image is visualized, highlighting the presence of both horizontal and vertical lines. The denoised image is presented in Figure 3.2b, where the corresponding Fourier transform, shown in Figure 3.2d, has noise pixels replaced with the mean value of adjacent pixels. The noise eliminated solely by removing the vertical line in the Fourier space is displayed in Figure 3.2e, while Figure 3.2f showcases the noise removed by eliminating both the horizontal and vertical lines in the Fourier space. The resulting image exhibits a notable enhancement in quality, indicating that the process effectively distinguishes and removes noise without compromising spatial information.

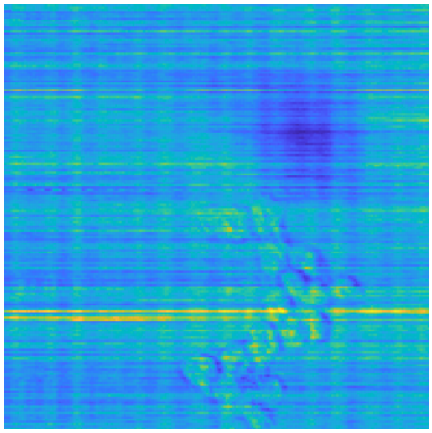

(a) Original BCARS image.

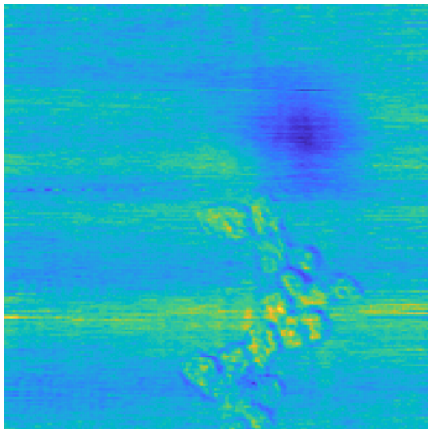

(b) Denoised BCARS image.

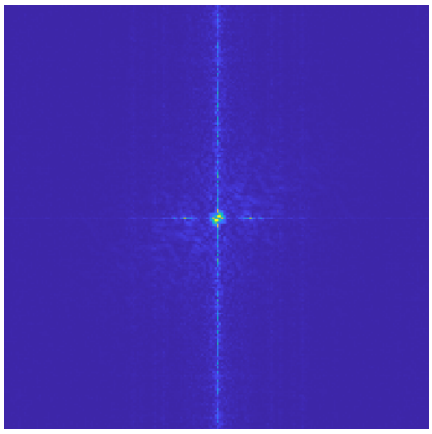

(c) Fuorier transform.

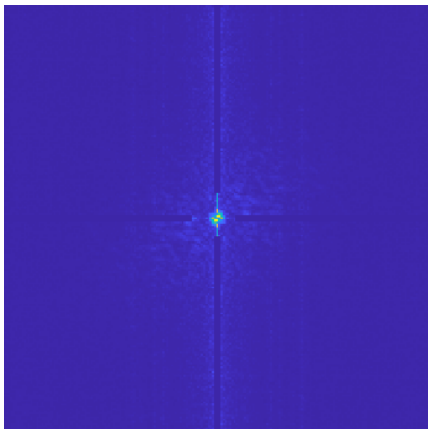

(d) Denosied Fourier transform.

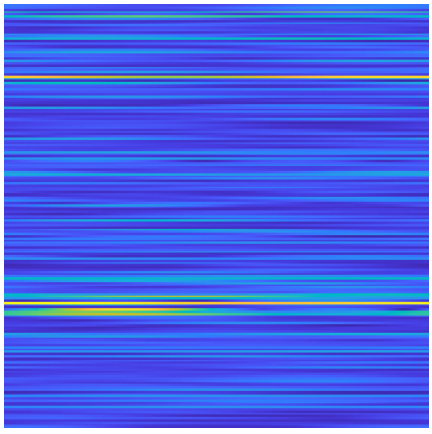

(e) Horizontal noise.

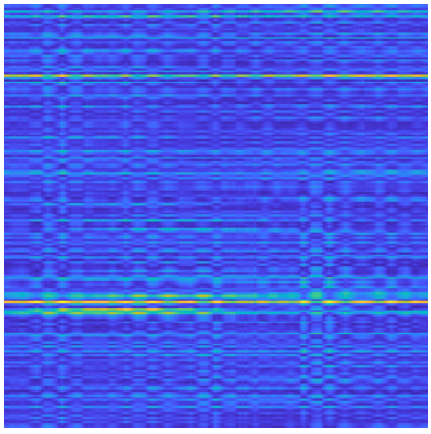

(f) Total noise.

Figure 3.2: Figure (a) depicts the integrated BCARS image of HeK293 cells prior to the denoising process. Subsequently, Figure (b) showcases the same image after undergoing the denoising procedure. The Fourier transform of the original image is presented in Figure (c), while Figure (d) exhibits the Fourier transform after the denoising procedure. Figure (e) specifically illustrates the noise attributed to the vertical line in the Fourier domain, whereas Figure (f) represents the overall noise resulting from both the vertical and horizontal lines in the Fourier domain.

3.2.2. Denosing via Singular Value Decompositon

The BCARS hyperspectral data still exhibit the presence of noise, which adversely affects the accuracy of the measurements. This noise predominantly takes the form of white noise, primarily stemming from the inherent dark noise of the CCD. Consequently, it becomes necessary to eliminate this noise. To achieve noise reduction in BCARS hyperspectral data, I employ singular value decomposition (SVD) on Anscombe-transformed spectra [75, 76].

The SVD technique operates under the assumption that noise is additive and follows a normal distribution, commonly known as Gaussian noise. However, in BCARS, the noise often possesses a mixed nature. It combines elements of both additive white Gaussian noise and Poisson noise. Consequently, in order to correctly apply SVD, the noise must be "whitened." In other words, the raw data exhibit a mixed noise with the mixing ratio varying across individual spectra, rather than having a noise that remains approximately constant within each spectrum. The Anscombe transform [77] can be applied to the BCARS hyperspectral data to perform a variance stabilization aimed at whitening the noise. To address the issue of mixed noise in the BCARS hyperspectral data, I adopted a two-step approach. First, an Anscombe transformation was applied to the data, followed by the inverse Anscombe transformation after matrix reconstruction. This process aimed to restore the BCARS spectra with mixed noise.

Subsequently, a singular value decomposition (SVD) denoiser was employed. The BCARS dataset is initially in a three-dimensional format, with dimensions of $m \cdot n \cdot s$. Here, m represents the number of spatial pixels along the x-axis, n represents the number of spatial pixels along the y-axis, and s represents the number of spectral pixels. To apply the SVD algorithm, the dataset was unfolded into a two-dimensional matrix, denoted as M. In this matrix, the rows represent the spectral axis with s spectral points, while the columns represent the spatial pixels, totaling $p = m \cdot n$. The SVD algorithm decomposes this matrix into three components:

$$M = USV^* \tag{3.1}$$

Where the matrix U is a two-dimensional matrix of size $s \cdot s$ that contains the spectral bases, which are orthonormal eigenvectors. The matrix S is a diagonal matrix of size $s \cdot s$ that contains the singular values (SV), also known as eigenvalues, ordered in descending order. The matrix V, with dimensions $p \cdot s$, describes the spatial distribution of the bases in U. The symbol '*' represents the conjugate transpose operation. A straightforward approach for noise removal involves setting an arbitrary cut-off threshold (C). All eigenvalues beyond this threshold are set to zero, effectively making all higher diagonal elements of S equal to zero. Subsequently, a denoised hyperspectral data matrix, denoted

as $\hat{M}$, is reconstructed using the following procedure:

$$\hat{M} = U\hat{S}V^* \tag{3.2}$$

where $\hat{S} = S\{1 : C\}$.
The singular values of the SVD decomposition capture different levels of spatial and spectral coherence in the data. The higher-order singular values represent the contribution of high spatial and spectral coherence, while the lower-order singular values correspond to less coherent parts. By setting all singular values above a specific order to zero, I effectively remove the singular vector with the least spatial and spectral coherence. This denoising approach takes advantage of the fact that noise is typically random in space and exhibits high frequencies in spectra [78].
However, it is important to select the appropriate singular value to ensure accurate reconstruction of the hyperspectral data. Selecting too many singular values can result in ineffective or weak denoising while using too few singular values can lead to distorted or erroneous signal reconstruction. Thus, a balance must be struck between maintaining spectral integrity and achieving significant noise reduction.
The method I employ for selecting singular values is more complex than those described previously. To determine the suitable singular values, I transform the absolute values of the spatial components (after subtracting the mean) for each singular value ($|V|$) using a two-dimensional Fourier transform. In the Fourier domain, a rectangular boundary is applied to separate the high-frequency components (mostly noise) from the low-frequency components (mostly signal). The high-frequency components outside the boundary primarily consist of noise, while the low-frequency components inside the boundary predominantly contain the signal. Figure 3.4 illustrates the Fourier transforms of the first and one-hundredth singular values of a BCARS image, with the highlighted boundary indicating the distinction between the signal region and the noise region. It is evident that the first singular value contains a significant amount of information about the image. However, as the order of the singular value increases, the information content progressively diminishes.

I can introduce a new feature called the "spatial signal ratio" (SSR), which quantifies the relationship between pixel intensities within and outside a designated boundary in the Fourier transform components. The SSR is computed as the sum of pixel intensities inside the boundary, represented by the complex modulus of the Fourier transform components, divided by the sum of pixel intensities outside the boundary. This ratio is then scaled by the respective number of pixels within and outside the boundary. I opted for rectangular borders situated at the center of the Fourier plane, covering an area equivalent to 1/9

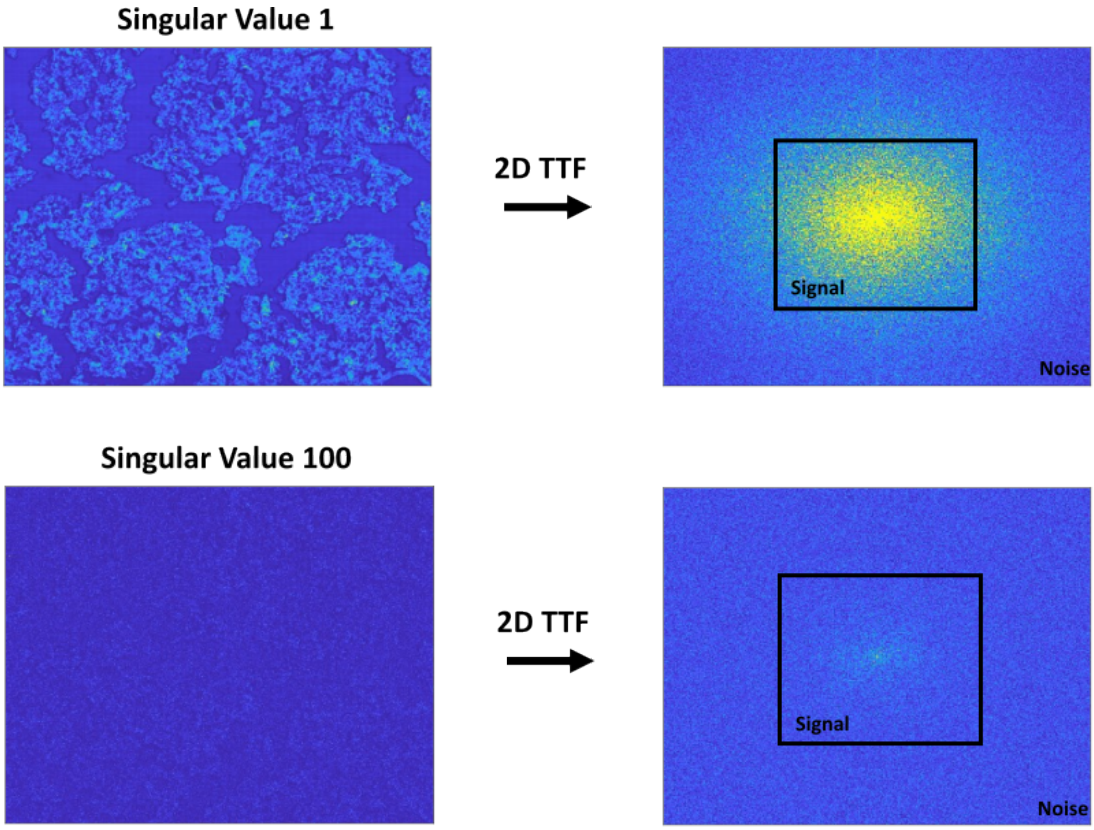

Figure 3.3: The figure presents the first and one-hundredth singular values of an image depicting NASH liver slices, along with their respective Fourier transforms. The visual representation highlights the conversion of spatial content into the Fourier domain, enabling the identification of distinct "signal" and "noise" regions.

of the total image area. This specific area proportion was consistently chosen across all experiments, following multiple trial iterations to ascertain and select the most optimal value.

In Figure 3.2.2, I plot the SSR as a function of the corresponding singular value. The plot reveals that the lowest singular values exhibit the highest SSR, indicating a stronger presence of signal-related information. Conversely, the higher singular values demonstrate smaller SSR values, suggesting a predominant presence of noise. Consequently, for the reconstruction of the denoised hyperspectral data matrix $\hat{M}$, I only consider singular values that exhibit high SSR and contain relevant signal information. The cut-off value, that discriminates the high and low SSR, is given by a multiple of σ, where σ is the standard deviation calculated from the SSR of the highest singular values. The multiplier factor is assumed to be 3.5.

In Figure 3.5, the spectrum of a single pixel from a NASH liver slice image is presented,

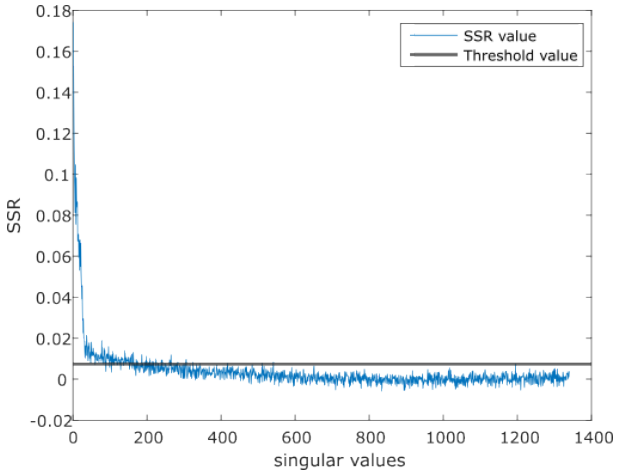

Figure 3.4: The figure displays the spatial signal ratio (SSR) for each singular value of matrix S. The SSR values are plotted, with the cut-off value separating the high and low SSR regions highlighted in black.

demonstrating the significant contribution of SVD in enhancing the quality of the spectrum. Notably, SVD plays a crucial role in reducing noise and minimizing fluctuations, resulting in a smoother and more reliable spectrum.

3.2.3. NRB removal

The primary objective of CARS microspectroscopy is to extract the chemical information contained within a sample, specifically by isolating the chemically specific Raman signal from the non-resonant background. The NRB arises from the combined effects of resonant and non-resonant susceptibility, leading to spectral distortions. However, it should be noted that the NRB amplifies the faint Raman signals, enabling high-sensitivity detection, even in the fingerprint region where signals tend to have low intensity [79, 80].
In the context of CARS spectroscopies, there are two commonly employed classes of numerical methods to mitigate NRB distortion after data acquisition. These methods utilize phase-retrieval techniques, leveraging the inherent heterodyne nature of the CARS signal. The first class involves maximizing entropy through the Maximum Entropy method (MEM) [81], while the second class exploits phase retrieval using the time-domain Kramers-Kronig (KK) relations [82]. It is worth noting that these techniques are functionally equivalent [83] and have been successfully applied to various sample types, including materials [84, 85] and biological samples [86, 87].
In section 1.4.2, it has been discussed that the intensity of the CARS signal is directly proportional to the square of the modulus of the third-order nonlinear susceptibility which

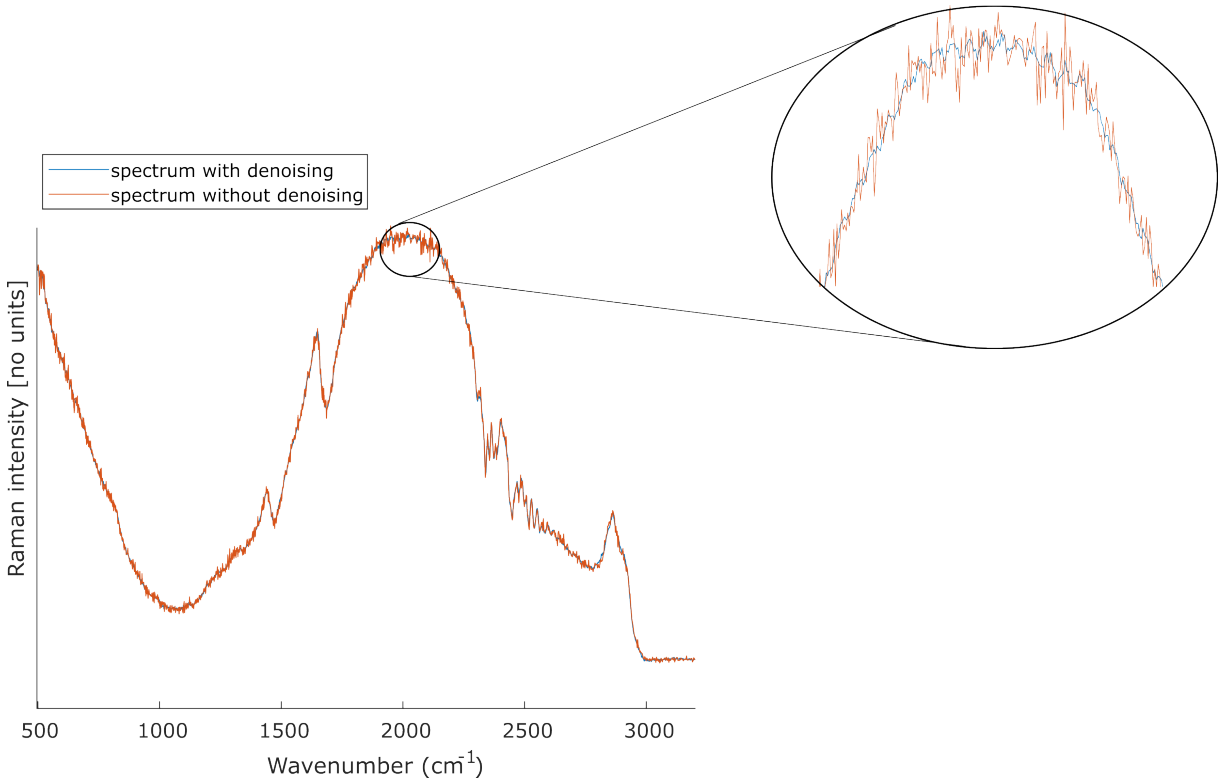

Figure 3.5: The figure showcases the BCARS signal obtained from a specific pixel in NASH liver slices, represented in red before the denoising procedure based on SVD, and in blue after the denoising. Additionally, a zoomed-in section of the spectrum emphasizes the significant impact of the denoising procedure in enhancing the quality of the spectrum.

is obtained by combining the resonant and non-resonant contributions.

$$I_{CARS} \propto |\chi^{(3)}|^2 = |\chi_R^{(3)} + \chi_{NR}^{(3)}|^2 = |\chi_R^{(3)}|^2 + |\chi_{NR}^{(3)}|^2 + 2\chi_{NR}^{(3)}\mathbb{R}e\left\{\chi_R^{(3)}\right\} \tag{3.3}$$

The resonant susceptibility $\chi_R^{(3)}$ is a complex number, with the real part exhibiting a dispersive shape and the imaginary part demonstrating a Lorentzian shape. On the other hand, the non-resonant susceptibility $\chi_{NR}^{(3)}$ is real when it is sufficiently far from electronic resonances. Consequently, MEM and KK methods are employed to retrieve the phase $\phi(\omega)$ of $\chi^{(3)}$ to isolate the imaginary Raman resonant component $\mathbb{I}m\left\{\chi_R^{(3)}\right\}$ from the overall nonlinear susceptibility.

In our experiments, we primarily employ the time domain Kramers-Kronig algorithm for the removal of the NRB. Here, we describe this method.

In section 1.4.2 we have expressed the CARS signal in terms of the pump and probe

intensities However, it could be rewritten in terms of the electric field:

$$I_{CARS}(\omega) = |\left\{ \Big[E_s(\omega) \otimes E_p(\omega)\Big]\chi^{(3)}(\omega) \right\} * E_p(\omega)|^2 \triangleq |\tilde{C}_{st}|^2||\tilde{\chi}^{(3)}|^2 \tag{3.4}$$

Where E_s and E_p are the electric fields of the stokes and pump beam, $\otimes$ indicates the cross-correlation operators, and $*$ is the convolution operators. C_{st} is the coherent stimulation profile and it corresponds to the correlation between pump and probe fields:

$$C_{st} = E_s(\omega) \otimes E_p(\omega) \tag{3.5}$$

If we assumed a spectrally narrow pump beam, we can introduce an effective stimulation profile $\tilde{C}_{st}$ and the effective non-linear susceptibility $\tilde{\chi}^{(3)}(\omega)$ as:

$$\tilde{C}_{st} = \frac{E_s(\omega) \otimes E_p(\omega)}{\int E_p} \tag{3.6}$$

$$\tilde{\chi}^{(3)}(\omega) = \chi^{(3)}(\omega) * E_p(\omega) \tag{3.7}$$

The time domain Kramers-Kronig relations establish an explicit connection between the real and imaginary components of a function, denoted as $f(\omega)$. In the context of CARS, neither the real nor imaginary part of the third-order susceptibility, $\chi^{(3)}$, can be directly observed. Furthermore, when the function is square integrable, its complex norm and phase are intricately related, as expressed by relation [75]:

$$\ln(|f(\omega)|) = -\hat{\mathscr{H}}(\phi(\omega)) \tag{3.8}$$

$$\phi(\omega) = \hat{\mathscr{H}} \ln(|f(\omega)|) \tag{3.9}$$

where $\hat{\mathscr{H}}$ is the Hilbert transform. In principle, to apply the formulas the complex modulus or the phase of the function over an infinite range of frequencies must be known. However, the CARS spectrum is limited in frequency, we measure only a portion of the spectrum; thus a 'windowed Hilbert transform' $\hat{\mathscr{H}}$, that is limited between frequency ω_a and ω_b, is required. It is defined as follows:

$$\hat{\mathscr{H}}_w(f(x); \omega_a, \omega_b) = \frac{\mathscr{P}}{\pi} \int_{\omega_a}^{\omega_b} \frac{f(x')}{x - x'} dx' \tag{3.10}$$

Where $\mathscr{P}$ is the Cauchy principal value. Under the following two conditions:

- The Raman peaks that are contained inside the spectral window is not affected by those outside of the window.
- We are far from any electronic resonances as is typically the case with infrared pumps and stokes.

the windowed and analytic Hilbert transform are related by the following relationship:

$$\hat{\mathscr{H}}_w\left\{\frac{1}{2}\ln(\left|\tilde{\chi}^{(3)}\right|^2)\right\} \approx \hat{\mathscr{H}}\left\{\frac{1}{2}\ln(\left|\tilde{\chi}^{(3)}\right|^2)\right\} + \epsilon(\omega) \tag{3.11}$$

Where $\epsilon(\omega)$ is an additive term introduced using the windowed version of the Hilbert transform. Applying the windowed Hilbert transform (3.10) of the logarithm of the CARS signal intensity (3.7) and considering the property (3.9) and (3.11), we can obtain the retrieved phase from raw CARS spectrum, ϕ_{CARS}:

$$\begin{aligned}\phi_{\mathrm{CARS}}(\omega) &= \hat{\mathscr{H}}_w\left\{\frac{1}{2}\ln(I_{\mathrm{CARS}}(\omega))\right\} \\ &\approx \epsilon(\omega) + \hat{\mathscr{H}}\left\{\frac{1}{2}\ln\left|\tilde{\chi}^{(3)}\right|^2\right\} + \hat{\mathscr{H}}_w\left\{\frac{1}{2}\ln\left|\tilde{C}_{\mathrm{st}}\right|^2\right\} \\ &= \epsilon(\omega) + \hat{\mathscr{H}}_w\left\{\frac{1}{2}\ln\left|\tilde{C}_{\mathrm{st}}\right|^2\right\} + \angle[\chi_R(\omega) + \chi_{NR}(\omega)]\end{aligned} \tag{3.12}$$

where $\angle$ represents the phase. In the assumption that we can measure directly the NRB intensity $I_{NRB} = |\tilde{C}_{st}|^2|\tilde{\chi}^{(3)}_{NR}|^2$, without Raman components and that we are far from electronic resonances such that $\chi^{(3)}_{NR}$ is almost real, we could apply the windows Hilbert transforms to the ratio $\frac{I_{CARS}}{I_{NRB}}$:

$$\begin{aligned}\phi_{\mathrm{CARS/NRB}}(\omega) &= \hat{\mathscr{H}}_w\left\{\frac{1}{2}\ln\left(\frac{I_{\mathrm{CARS}}(\omega)}{I_{\mathrm{NRB}}(\omega)}\right)\right\} \\ &\approx \epsilon(\omega) + \hat{\mathscr{H}}_w\left\{\frac{1}{2}\ln\left|\tilde{C}_{\mathrm{st}}\right|^2\right\} \\ &\quad - \left[\epsilon(\omega) + \hat{\mathscr{H}}_w\left\{\frac{1}{2}\ln\left|\tilde{C}_{\mathrm{st}}\right|^2\right\}\right] + \angle[\chi_R(\omega) + \chi_{NR}(\omega)] - \angle\chi_{NR}(\omega) \\ &\approx \angle[\chi_R(\omega) + \chi_{NR}(\omega)]\end{aligned} \tag{3.13}$$

Using the ratio $\frac{I_{CARS}}{I_{NRB}}$ as our signal, the complex spectrum can be written as:

$$I_{CARS/NRB} = \sqrt{\frac{I_{CARS}(\omega)}{I_{NRB}(\omega)}}e^{i\phi_{CARS/NRB}} \approx \frac{|\tilde{\chi}^{(3)}|}{|\tilde{\chi}^{(3)}_{NR}|}e^{i\angle[\chi^{(3)}_R + \chi^{(3)}_{NR}]} \tag{3.14}$$

The Raman spectrum I_{retr} can be extracted as the imaginary part of $I_{CARS/NRB}$:

$$I_{RL}(\omega) = \mathbb{I}m\{I_{CARS/NRB}(\omega)\} \approx \frac{\mathbb{I}m\{\chi_R^{(3)}(\omega)\}}{\left|\chi_{NR}^{(3)}\right|} \tag{3.15}$$

The imaginary part of the resonant third-order non-linear susceptibility carries the vibrational information. To a first degree of approximation [88] the spontaneous Raman spectrum is proportional to the imaginary part of the resonant susceptibility. Thus, the Raman-like spectrum is proportional to the spontaneous Raman spectrum scaled by the non-resonant component. The above method allows to extract the chemically-specific Raman signal from the NRB but it requires an accurate measurement of the NRB. In real-world conditions, the pure NRB of the sample cannot be measured directly. To overcome this problem the NRB is measured from a reference material with no Raman peaks, such as glass or water. So instead of the pure NRB measurement, we consider a reference measurement I_{ref}. By using the reference measurement, we introduce a multiplicative error such that $I_{ref}(\omega) = \zeta(\omega)I_{NRB}(\omega)$, where $\zeta(\omega)$ is assumed to be real and positive. Let us calculate the phase of the ratio $I_{CARS/ref}$, similarly to what we did in (3.13):

$$\phi_{CARS/ref}(\omega) = \hat{\mathscr{H}}_w\left\{\frac{1}{2}\ln\left(\frac{I_{CARS}(\omega)}{\zeta(\omega)I_{ref}(\omega)}\right)\right\} \approx \phi_{CARS/NRB} + \hat{\mathscr{H}}_w\left\{\frac{1}{2}\ln\left(\frac{1}{\zeta(\omega)}\right)\right\} \tag{3.16}$$

where the last term is the phase error introduced $\phi_{err}(\omega)$. Then, the Raman-like spectrum is the imaginary part of the spectrum obtained as the ratio $I_{CARS/ref} = \frac{I_{CARS}}{I_{ref}}$, where we use I_{ref} instead of I_{NRB}:

$$\mathbb{I}m\{I_{CARS/ref}(\omega)\} \approx \sqrt{\frac{1}{\zeta(\omega)}}\sqrt{\frac{I_{CARS}(\omega)}{I_{NRB}(\omega}})sin\Big(\phi_{CARS/NRB} + \phi_{err}\Big) \tag{3.17}$$

So, by using a reference NRB we get an amplitude error $A_{err} = \sqrt{\frac{1}{\zeta(\omega)}}$ and a phase error $\phi_{err} = \hat{\mathscr{H}}_w\left\{\frac{1}{2}\ln\left(\frac{1}{\zeta(\omega)}\right)\right\}$ that are connected by the Kramers-Kronig relation:

$$\ln(A_{err}) = -\hat{\mathscr{H}}\Big\{\phi_{err}(\omega)\Big\} \tag{3.18}$$

$$\phi_{err}(\omega) = \hat{\mathscr{H}}\Big\{\ln(A_{err}(\omega))\Big\} \tag{3.19}$$

However, a scaling error may be present. Since e the Hilbert transform of a constant is equal to zero, then $\zeta(\omega)$ is multiplied by a constant α, the phase error remains the same:

$$\phi_{\text{err}}(\omega) = \hat{\mathscr{H}_w}\left\{\ln\left(\frac{1}{\alpha\zeta(\omega)}\right)\right\} = \hat{\mathscr{H}_w}\left\{\ln\left(\frac{1}{\zeta(\omega)}\right)\right\} \tag{3.20}$$

In order to correct the phase and amplitude errors one can use the following steps:

- Remove phase error via detrending $\phi_{\text{CARS/ref}}(\omega)$ and correct part of the amplitude error exploiting the Kramers-Kronig relationship (3.19).
- Correct for scaling errors, related to the constant α, and for the use of the windowed version of the Hilbert transform in step 1, ϵ_{err} via unity-centering the real component of the phase-corrected spectrum [75].

The phase $\phi_{\text{CARS/ref}}$ is qualitatively similar to a Raman-like spectrum in which the spectral peaks extend positively from a zero baseline. Slowly varying deviation from the zero baselines is caused by a slowly varying phase error ϕ_{err}. Thus, one can use traditional baseline detrending methods in order to find ϕ_{err} from $\phi_{\text{CARS/ref}}$ and remove it. Then, from ϕ_{err}, one can retrieve part of the amplitude error and correct it. Finally, to get the phase-corrected spectrum I_{pc}, the retrieved spectrum $I_{\text{CARS/ref}}$ is multiplied by a complex phase-correction multiplier that takes into account the two corrections. The phase-corrected spectrum is as follows:

$$\begin{aligned} I_{\text{pc}} &= I_{\text{CARS/ref}}\left\{\frac{1}{e^{-\hat{\mathscr{H}_w}\{\phi_{\text{err}}(\omega)\}}}e^{-i\phi_{\text{err}}(\omega)}\right\} \\ &= \sqrt{\frac{I_{\text{CARS}}(\omega)}{I_{\text{ref}}(\omega)}}e^{i\phi_{\text{CARS/ref}}}\left\{\frac{1}{e^{-\hat{\mathscr{H}_w}\{\phi_{\text{err}}(\omega)\}}}e^{-i\phi_{\text{err}}(\omega)}\right\} \end{aligned} \tag{3.21}$$

Let's now consider the amplitude correction. We saw that retrieving A_{err} from ϕ_{err} leads to an ambiguity related to the scaling constant α. Furthermore, we are exploiting a window Hilbert transform instead of the analytical ones so window-effect error $\epsilon_{err}(\omega)$ is present:

$$\hat{\mathscr{H}_w}\{\phi_{\text{err}}(\omega)\} = \hat{\mathscr{H}_w}\{\phi_{\text{err}}(\omega)\} + \epsilon_{err} \tag{3.22}$$

To complete the error correction the ambiguity of A_{err} and $\epsilon_{err}(\omega)$ must be taken into account. Both quantities can be found by looking at the real component of the phase-corrected spectrum in (3.21). Since the real component of (3.16) is unitarily centered, which means that $\left\langle \frac{|\tilde{\chi}^{(3)}|}{|\tilde{\chi}^{(3)}_{NR}|} cos(\phi_{CARS/NRB/} \right\rangle = 1$, the existence of a scaling factor α will alter the mean. So, one can measure this mean and normalize I_{pc} by this value. On the other hand, the mean can have a frequency dependence due to ϵ_{err}. Using numerical means, though, one can find a slowly varying centerline and normalize the phase-corrected spectrum, thus removing α and ϵ_{err} in one step. Finally, the rescaled and phase-corrected

spectrum $I_{pc,sc}$ may be calculated as:

$$I_{pc,sc} = \frac{I_{pc}(\omega)}{\left\langle Re\{I_{pc}(\omega)\}\right\rangle} = \frac{|\tilde{\chi}^{(3)}|}{|\tilde{\chi}^{(3)}_{NR}|} e^{(i\phi_{CARS/NRB})} \tag{3.23}$$

The Kramers-Kroning algorithm allows removing the NRB from the raw spectrum even with a measurement of a reference NRB spectra and extrapolating the pure vibrational information.

The accompanying figures 3.6 and 3.7 serve as a compelling demonstration of the potential of denoising techniques, specifically through SVD decomposition and the KK algorithm, in the analysis of BCARS images obtained from a NASH liver slice. The sequential analysis of the images underscores the vital role played by denoising in enhancing contrast and improving the signal-to-noise ratio, as exemplified in Figures 3.6c and 3.6d. Notably, Figure 3.7 presents a significant finding, as denoising effectively reduces noise and artifacts in the retrieved CARS signal, resulting in heightened spectral sensitivity.

Through the denoising procedure, previously unseen and indistinguishable Raman peaks become detectable and discernible. For instance, the denoised retrieved spectrum (blue line) exhibits the presence of the phenylalanine peak at 1000 cm^{-1}, which is absent in the green curve. This exemplifies the increased capability of denoising to uncover subtle features within the data.

Furthermore, the figures affirm the efficacy of the KK algorithm in successfully removing the NRB, thereby enabling the retrieval of pure vibrational information from the spectrum. This combined approach of denoising and NRB removal holds promise for advancing the analysis and interpretation of BCARS data in the study of NASH liver slices.

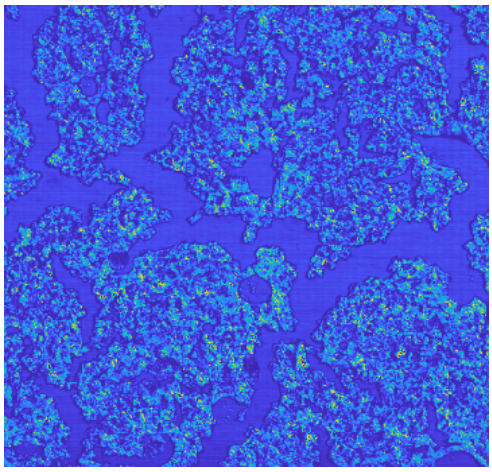

(a) Original image.

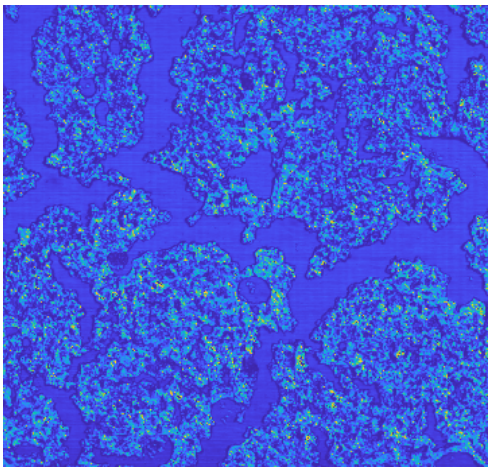

(b) Image after denoising.

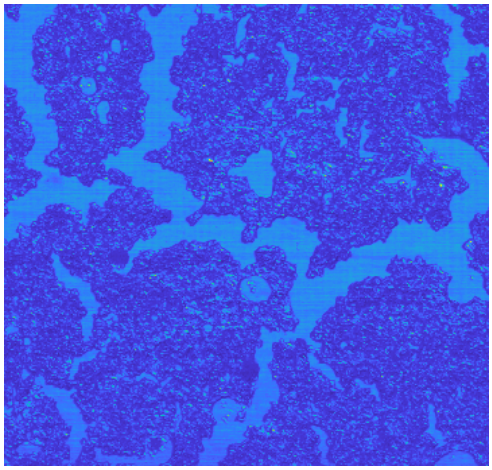

(c) Image after KK and denoising.

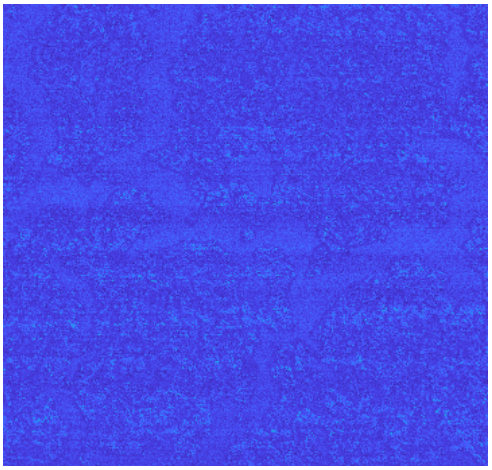

(d) Image after KK without denoising.

Figure 3.6: Presented here are the visual representations of NASH liver slices following the post-processing procedure. In Figure a, we observe the integrated raw BCARS image. Figure b showcases the integrated denoised image obtained through SVD decomposition. Moving on to Figure c, we witness the integrated image after the removal of NRB using the KK method. Finally, Figure d displays the ultimate integrated image following KK removal, although denoising was not applied in this case.

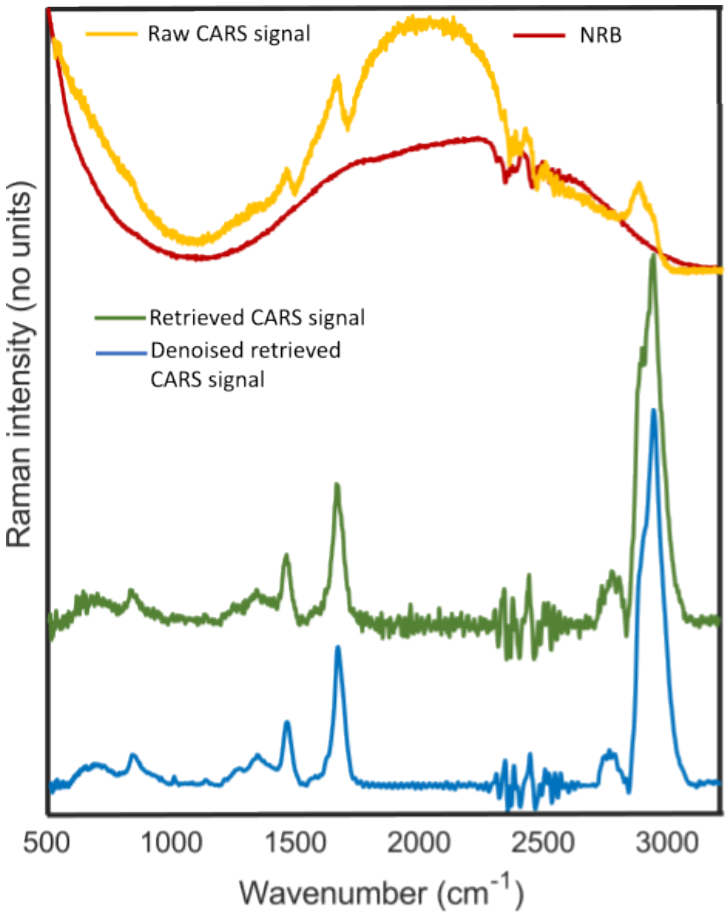

Figure 3.7: The red line represents the reference NRB that was measured and utilized in the KK algorithm. The yellow line corresponds to the raw BCARS signal obtained from a single pixel of a NASH liver slice. The green and blue lines depict the BCARS signal subsequent to KK removal, without and with denoising applied, respectively.

3.2.4. Spectral unmixing

After the denoising procedure and the removal of non-resonant background (NRB), we proceed with the unmixing of chemical components in heterogeneous samples. This process is particularly relevant in the context of broadband coherent anti-Stokes Raman scattering (BCARS) imaging and spectroscopy, aiming to identify distinct spectral features associated with the analytes under investigation.

In spectroscopic applications, we employ principal component analysis (PCA) to fulfill this purpose. PCA is a widely used technique for spectral analysis, enabling the identification and extraction of meaningful information from complex datasets. It allows for the reduction of dimensionality while preserving the most significant spectral variations.

In the case of CARS imaging, where spectral unmixing is required, we can classify the al-

gorithms into two categories: factorization-based methods, exemplified by the N-FINDR algorithm, and clustering methods, such as k-means cluster analysis.
The distinction between factorization and clusterization methods lies in their objectives. Factorization methods are geared towards decomposing the hyperspectral dataset $\boldsymbol{D}$ into two matrices, $\boldsymbol{S}$ for spectra and $\boldsymbol{C}$ for concentrations, in a manner such that $\boldsymbol{D} = \boldsymbol{C}\boldsymbol{S}^* + \epsilon$, with ϵ representing the minimized error in the algorithm's iterative process. In the context of factorization, each pixel spectrum within an image can be conceptualized as a linear amalgamation of the spectral components identified by the algorithm. The coefficients of this linear amalgamation correspond to the concentrations of specific species present in the sample.
In contrast, clusterization methods are designed to identify two or more groups of pixels with shared spectral attributes within hyperspectral images. The spectrum affiliated with a given cluster serves as a representative for all pixels within that cluster. Notably, within the clusterization framework, if a pixel belongs to one group, it is precluded from being included in another. Consequently, the outcome of clusterization comprises a matrix of representative spectra and an image in which each pixel is exclusively associated with a single class.
In the subsequent sections, we will provide detailed explanations of these methods, including their underlying principles, mathematical formulations, and practical implementations.

Principal Component Analysis

Principal Component Analysis (PCA) [89] is a technique utilized to reduce the dimensionality of large datasets, enhancing interpretability while minimizing information loss. PCA maximizes variance successively by creating new uncorrelated variables, known as principal components. These components are obtained by solving an eigenvalue-eigenvector problem specific to the dataset being analyzed.
PCA serves as a dimensionality reduction method, transforming a large set of variables into a smaller one while retaining most of the original information. Its objective is to identify the directions within the data that maximize variance, providing optimal projections for dimensionality reduction [90].
In summary, PCA finds the variance-maximizing directions onto which the data is projected, thereby reducing the number of variables while preserving crucial information. The algorithm can be defined as follows: the Principal component analysis procedure is a dimension reduction technique that projects the data on k-dimensions by maximizing

the variance of the data as follows:

- Step 1: Normalize the data to have a mean of 0 and a standard deviation of 1.

$$\hat{x}_j^{(i)} = \frac{x_j^{(i)} - \mu_j}{\sigma_j} \tag{3.24}$$

  where $\mu_j = \frac{1}{m}\sum_{i=1}^{m} x_j^{(i)}$ and $\sigma_j^2 = \frac{1}{m}\sum_{i=1}^{m}(x_j^{(i)} - \mu_j)^2$.

- Step 2: Compute the covariance matrix $\Sigma = \frac{1}{m}\sum_{i=1}^{m} \hat{x}^{(i)}(\hat{x}^{(i)})^T \in \mathbb{R}^{n\times n}$, which is symmetric with real eigenvalues.

- Step 3: Compute $u_!, ..., u_k \in \mathbb{R}^n$ the k orthogonal principal eigenvectors of Σ, i.e. the orthogonal eigenvectors of the k largest eigenvalues.

- Step 4: Project the data on $span_{\mathbb{R}}(u_1, ..., u_k)$. This procedure maximizes the variance among all k-dimensional spaces.

This procedure is exemplified in Figure 3.8

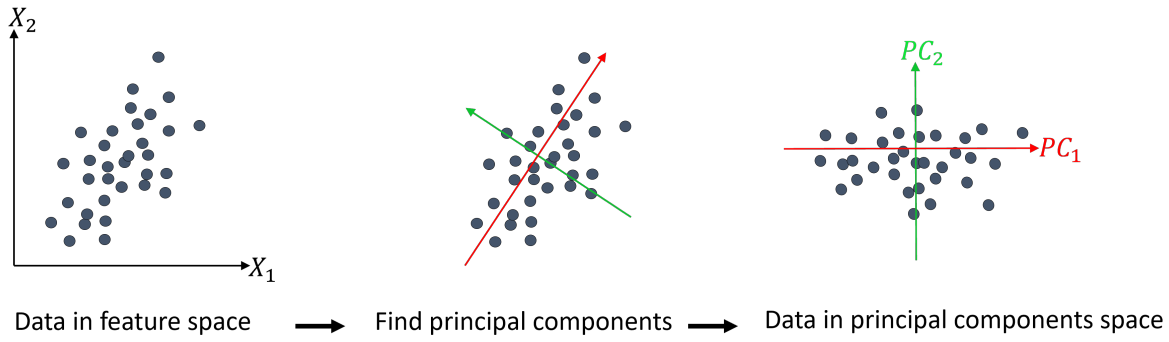

Figure 3.8: The image depicts a visual representation of the sequential steps involved in performing principal component analysis on a large dataset.

N-FINDR alghoritm

The N-FINDR algorithm [91] is a factorization method used for decomposing a hyperspectral dataset, denoted as D, into a matrix of spectra (S) and a matrix of concentrations (C). The goal is to minimize the error (ϵ) in the iterative process, resulting in the equation $D = CS^* + \epsilon$. In factorization methods, each pixel's spectrum in the image can be viewed as a linear combination of the spectral basis identified by the algorithm, with the coefficients representing the concentrations of the species in the sample.
Specifically, the N-FINDR algorithm aims to reduce the dimensionality of hyperspectral data by identifying the combination of spectra, referred to as endmembers, that best

represent the entire image. The algorithm maximizes a quantity proportional to the determinant of an augmented endmember matrix (E), which is constructed by appending a row of ones and the endmembers themselves, defining the $i-th$ endmember as e_i as follows:

$$E = \begin{bmatrix} 1 & 1 & \cdots & 1 \\ e_1 & e_2 & \cdots & e_m \end{bmatrix}$$

The volume, $V(E)$, is defined as:

$$V(E) = \frac{1}{(m-1)!} \cdot |E| \tag{3.25}$$

where m is the number of endmembers.
The algorithm starts with a random set of vectors and proceeds by evaluating each pixel's likelihood of being a pure or nearly pure pixel. This evaluation involves calculating the volume using each pixel as a replacement for each endmember. If the replacement results in an increase in volume, the pixel replaces the corresponding endmember. This process continues until no more replacements occur, resulting in the identification of the endmembers.
Once the endmembers are found, the spectra serve as the new basis for projecting the initial image using a non-negatively constrained least squares algorithm. This final step allows for the determination of abundance or concentration maps in the reduced dataset.

K-means cluster analysis

We also utilize K-means cluster analysis (KMCA) [92, 93] as another method belonging to the clusterization algorithm family, aiming to identify distinct groups of pixels with similar spectral features in hyperspectral images. Each cluster is represented by a spectrum that characterizes all the pixels within that cluster. It is important to note that each pixel can only belong to one cluster, resulting in a matrix of representative spectra and an image where each pixel is associated with a single class.
KMCA is specifically used for spectral unmixing. Clustering involves dividing the original dataset into k subsets known as clusters. We denote $c^{(i)}$ as the cluster of data point i and μ_j as the center of cluster j. The number of clusters, k, is initially determined through a guess. The k-means algorithm begins by randomly distributing the k clusters and then calculates the distance between each spectrum in the dataset and the mean cluster spectrum. Subsequently, each spectral trace is assigned to the cluster with the closest mean spectrum. Iterating these steps leads to optimized results. Therefore, the algorithm, after randomly initializing the cluster centroids $\mu_1, \mu_2, \ldots, \mu_k \in \mathbb{R}$, repeats the

following step until convergence:

$$c^{(i)} = \arg\min_j \|x^{(i)} - \mu_j\|^2 \tag{3.26}$$

and

$$\mu_j = \frac{\sum_{i=1}^{m} 1_{\{c^{(i)}=j\}} x^{(i)}}{\sum_{i=1}^{m} 1_{\{c^{(i)}=j\}}} \tag{3.27}$$

This procedure is exemplified in the Figure 3.9 .

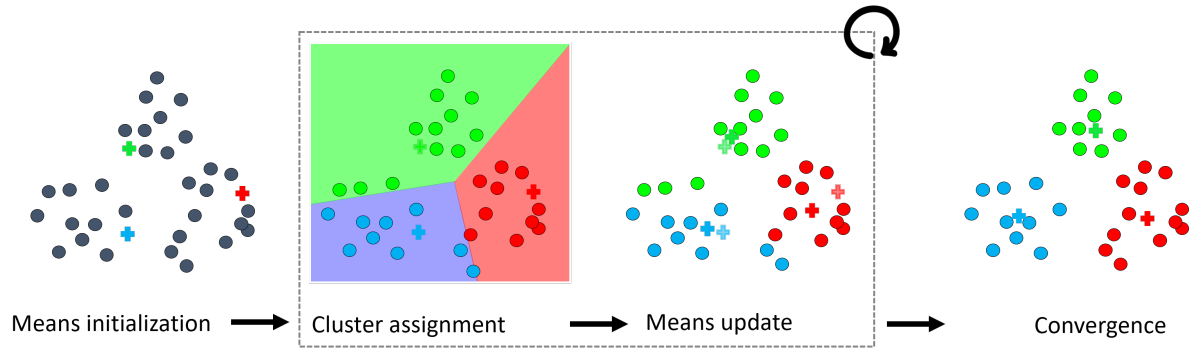

Figure 3.9: The image depicts a visual representation of the sequential steps involved in performing the k-means analysis.

The main objective of KMCA is to minimize the distances between data within each cluster while maximizing the distances between different clusters based on a well-defined distance metric. To evaluate the convergence of the algorithm, we examine the distortion function or clustering error defined as follows:

$$J(c, \mu) = \sum_{i=1}^{m} \|x^{(i)} - \mu_{c^{(i)}}\|^2 \tag{3.28}$$

As mentioned earlier, the k-means algorithm iteratively finds locally optimal solutions based on this distance metric.

4 | Experimental results

In this chapter, I will showcase and analyze the outcomes achieved using the BCARS system, along with the post-processing techniques mentioned in the preceding chapters. Initially, I will present the spectra of solvents, followed by a more detailed exploration of the chemical distinctions inherent in the spectra of subcellular components. Subsequently, I will undertake a statistical analysis utilizing PCA across distinct tumor lines, including HepG2 and HeK293. Moreover, I will showcase the practical implementation of BCARS imaging on a NASH liver slice, enabling high-speed acquisition and facilitating the generation of concentration maps for various chemical species. This approach offers valuable chemical insights without compromising the integrity of the samples. Lastly, I will showcase the multimodal imaging approach, capturing both BCARS and Second Harmonic Generation (SHG) images, to visualize microcalcifications and to extract the spectrum of collagen.

4.1. BCARS spectroscopy

4.1.1. BCARS spectroscopy of solvents

To evaluate the system's performance, I conducted measurements on the spectral profiles of six solvents: acetone, ethanol, methanol, isopropanol, dimethyl sulfoxide (DMSO), and toluene. These experiments involved depositing 100 μL droplets of the solvents between two glass coverslips, each with a thickness of 170 μm. The CCD exposure time was set to 1 ms. Subsequently, I calculated the average spectrum for each solvent by averaging the 100 individual spectra obtained during the measurements.
Our measurements comprehensively covered the entirety of the fingerprint region and the CH-stretching region, which spanned from 500 cm^{-1} to 3200 cm^{-1}. These measurements were facilitated by leveraging the capabilities of both the 2-color mechanism, which encompassed the range from 1400 to 3200 cm^{-1}, and the 3-color mechanism, which extended from 500 to 1400 cm^{-1}. The spectra obtained from the raw data were processed using the Kramers-Kronig algorithm to eliminate the NRB contribution. The resulting spectra are

depicted by the blue curve in the accompanying Figure 4.1.1. Additionally, I compared the BCARS spectra with the corresponding SR spectra, represented by the gray areas in Figure 4.1.1. Notably, the comparison revealed excellent agreement regarding the relative positions of the peaks and their amplitude ratios.
Despite achieving favorable results so far, in the subsequent section, I aimed to further evaluate the performance of our setup by analyzing more challenging samples, specifically subcellular components. I compared the obtained results with the SR spectra. Also, the measurements are conducted in collaboration with the Leibniz Institute of Photonic Technology (IPHT) in Jena, where an experimental BCARS setup based on WLC generation in bulk media is utilized, much like the setup employed for my thesis. However, the distinguishing factor lies in their utilization of solely the 2-color CARS mechanism.

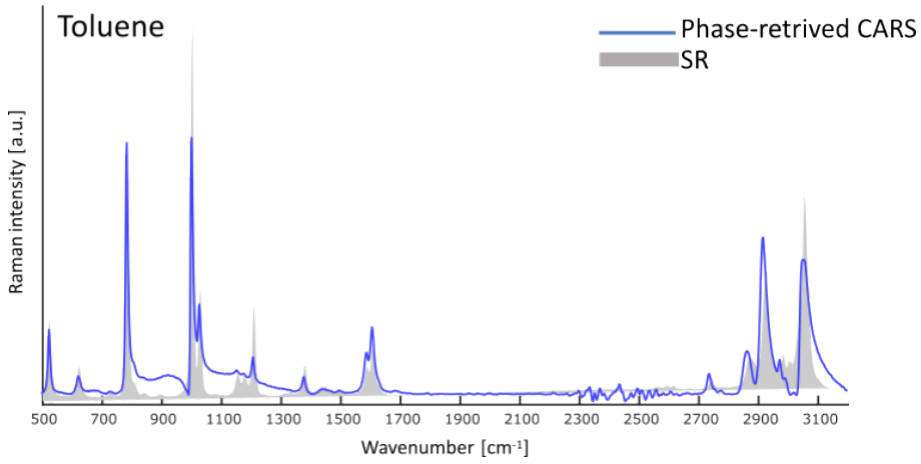
Toluene
Phase-retrived CARS
SR
Raman intensity [a.u.]
500 700 900 1100 1300 1500 1700 1900 2100 2300 2500 2700 2900 3100
Wavenumber [cm-1]

(a)

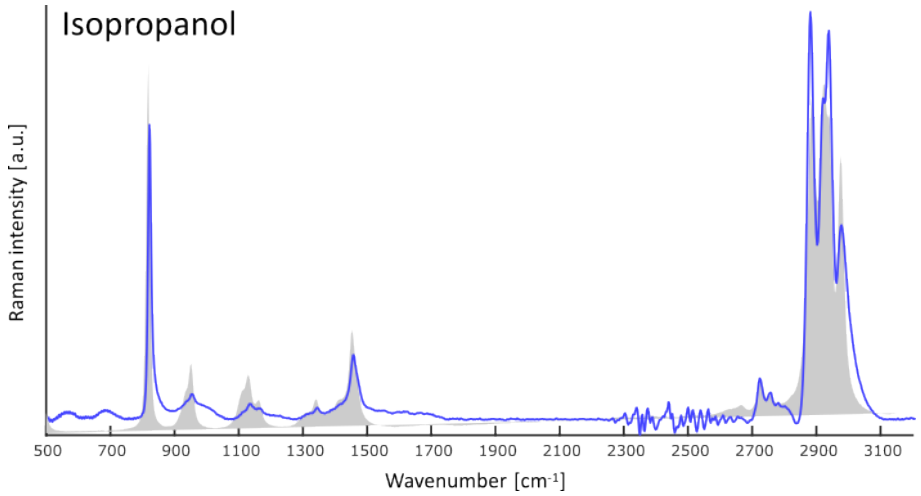
Isopropanol
Raman intensity [a.u.]
500 700 900 1100 1300 1500 1700 1900 2100 2300 2500 2700 2900 3100
Wavenumber [cm-1]

(b)

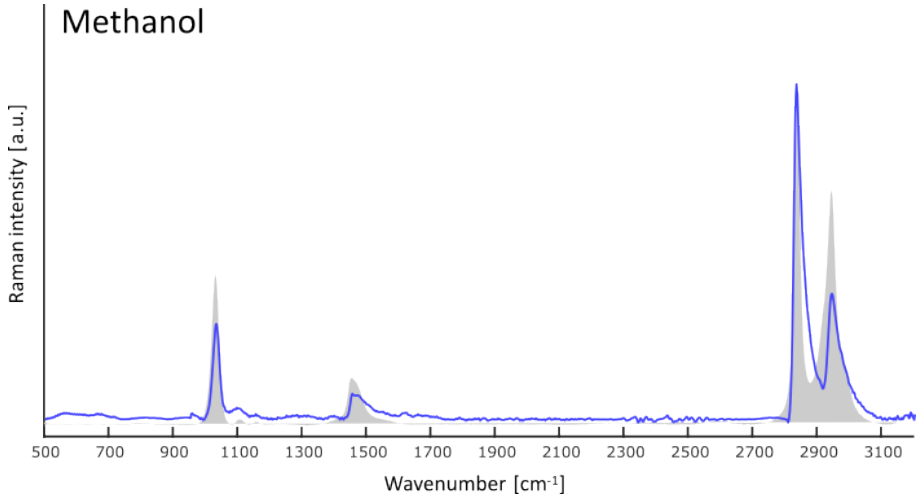
Methanol
Raman intensity [a.u.]
500 700 900 1100 1300 1500 1700 1900 2100 2300 2500 2700 2900 3100
Wavenumber [cm-1]

(c)

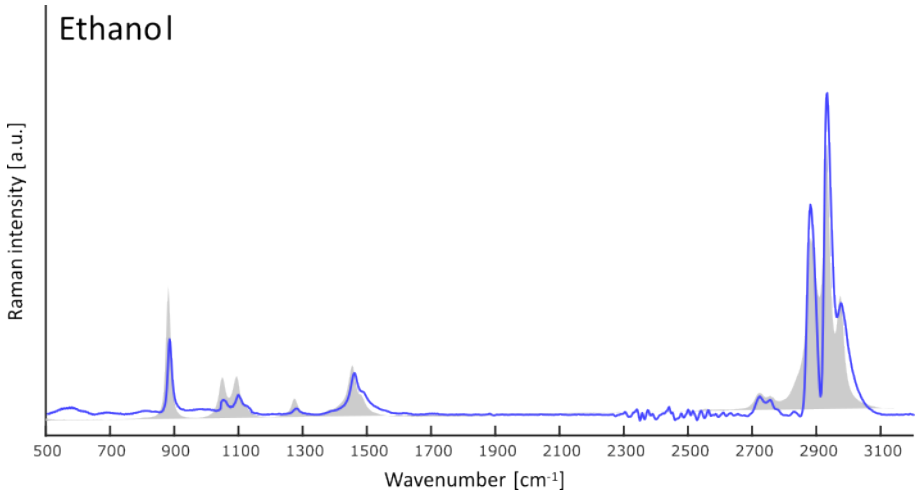

(d)

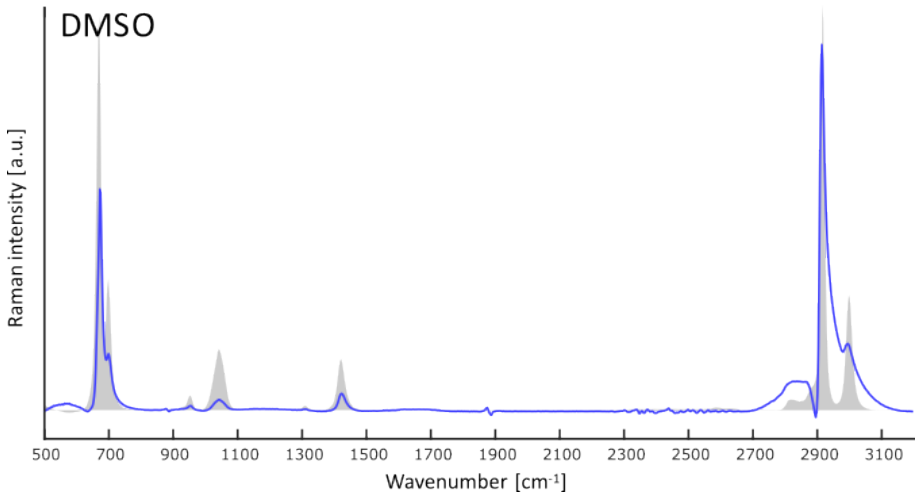

(e)

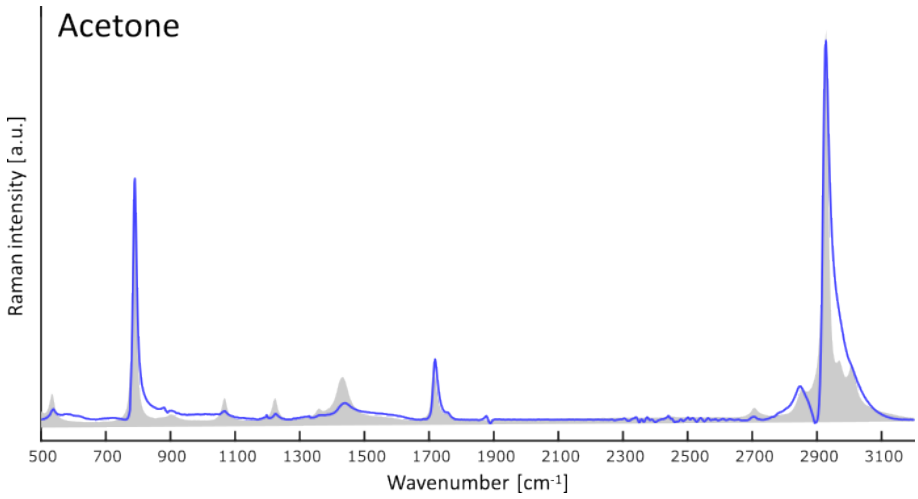

(f)

Figure 4.0: Reconstructed BCARS spectra (blue curves) and corresponding spontaneous Raman (SR) spectra (grey areas) of solvents (e) dimethyl sulfoxide (DMSO) and (f) acetone.

4.1.2. BCARS spectroscopy of subcellular componenets

In the following section, I assess the high sensitivity and accuracy of the BCARS setup in detecting subcellular components. Six distinct subcellular components, namely endoplasmic reticulum (ER), cytoplasm, nuclei, lysosomes, mitochondria, and mitochondria-associated membrane (MAM), were isolated from mice liver through centrifugation steps. The sample under analysis consists of 2 μL droplets of each subcellular component and buffer onto a 170 µm quartz coverslip and let it dry out for 1-2 hours. BCARS spectra were acquired with an exposure time of 50 ms. Each spectrum was then compared with its corresponding SR spectrum. For practical purposes, SR data were collected by analyzing subcellular components in a solution within a quartz cuvette, while BCARS data were collected by analyzing subcellular components dried onto a quartz coverslip.
The batch of subcellular components was purified and dialyzed to remove most of the residual molecules, primarily salts and surfactants, present in the purification buffers used during the isolation process. Figure 4.1 presents both the BCARS (in blue) and SR (in red) spectra of the four buffers used for the purification of subcellular components. The spectra of these buffers exhibit high similarity and mainly display spectral features attributed to surfactants, particularly Tween 20. Tween 20, also known as Polysorbate 20, is a non-ionic surfactant extensively utilized in various industries, including pharmaceuticals, cosmetics, and food. In the case of buffers, there is a notable resemblance between BCARS and SR measurements, especially in the fingerprint region, although BCARS may not be able to resolve some peaks in the CH-stretching regions and some peaks of the IBM3 buffer within the range of 1300-1400 cm^{-1}.

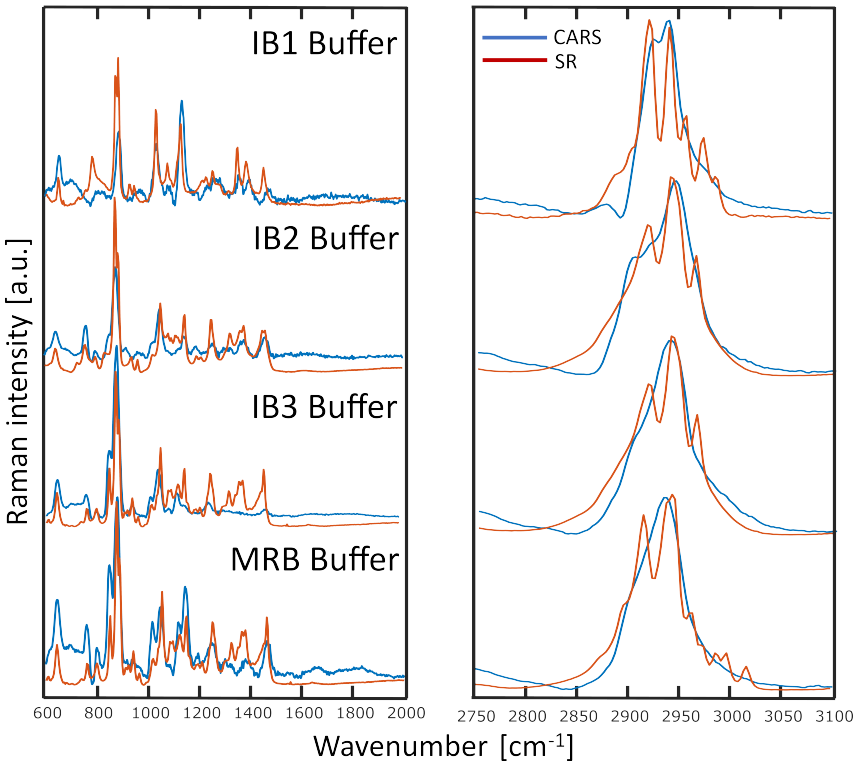

Figure 4.1: The image depicts the SR, in red, and the BCARS, in blue, spectra of the four buffers used for the purification of subcellular components.

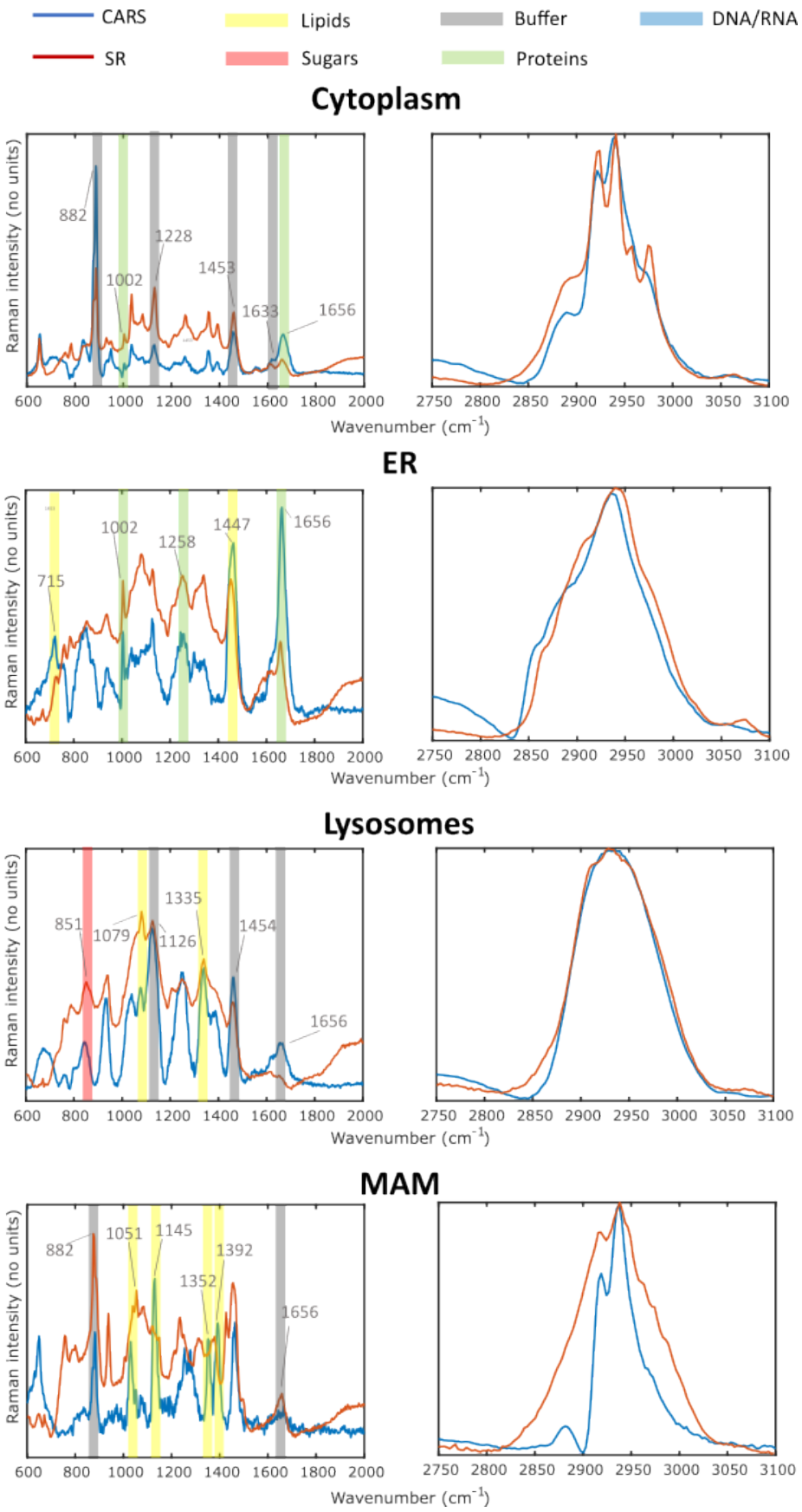
CARS
SR
Lipids
Sugars
Buffer
Proteins
DNA/RNA
Cytoplasm
Raman intensity (no units)
882
1002
1228
1453
1633
1656
Wavenumber (cm-1)
ER
715
1002
1258
1447
1656
Lysosomes
851
1079
1126
1335
1454
1656
MAM
882
1051
1145
1352
1392
1656

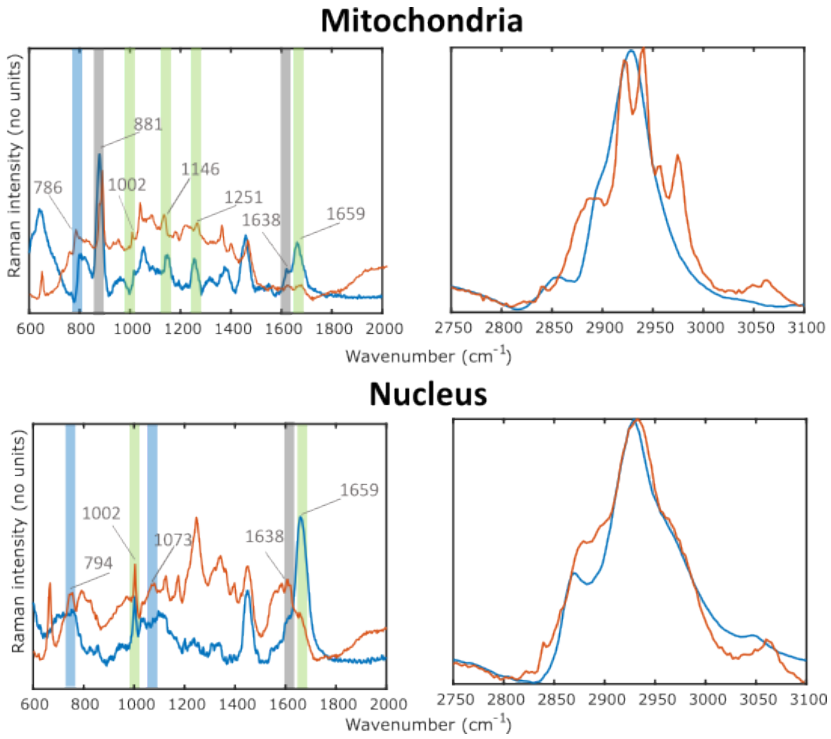

Figure 4.2: The figure illustrates both the BCARS (in blue) and SR (in red) Raman spectra in the fingerprint and CH-stretching regions obtained from the six different subcellular components (ER, cytoplasm, nuclei, lysosomes, mitochondria, and MAM). The colored bars indicate vibrational modes typically associated with a specific class of molecules (lipids, proteins, sugars, DNA/RNA) or buffers.

Figure 4.2 illustrates both the BCARS (in blue) and SR (in red) Raman spectra in the fingerprint and CH-stretching regions obtained from the six different subcellular components (ER, cytoplasm, nuclei, lysosomes, mitochondria, and MAM). Most spectral features observed in SR spectra are also visible in the spectra obtained by the two BCARS setups. Particularly, spectra related to ER, lysosomes, and nuclei display high similarity when comparing SR and BCARS spectra.
The presence of the water band around 1630 cm^{-1} in the SR spectra, observed in all subcellular components, represents a significant differentiation between SR and BCARS spectra. This discrepancy can be attributed to the fact that SR data were acquired from water-based solutions (buffers). In a similar vein, prominent peaks around 881 cm^{-1} may be discerned in several BCARS spectra. These peaks are likely associated with the presence of salts in the buffers and manifest as highly intense and relatively narrow bands when samples are examined under dry conditions, leading to a localized high salt concentration. Additional subtle variations can be observed when comparing different spectra; however, I attribute these primarily to the inherent heterogeneity of the sample after deposition onto the quartz substrate for BCARS analysis. The data obtained from the analysis of the endoplasmic reticulum (ER) provide additional evidence supporting the strong agreement between SR and BCARS data in the investigation of cellular components. The high level of similarity between the SR and BCARS spectra obtained from both setups in the case of the ER sample represents a highly promising outcome. The analysis of the spectra presented in Figure 4.2 indicates that the majority of spectral features align with the expected biochemical composition of the subcellular components obtained from mice liver purification. Specifically, the cytoplasm, representing the soluble components of the cell after separating most organelles such as the nucleus, lysosomes, endoplasmic reticulum (ER), and mitochondria, exhibits spectral characteristics primarily associated with soluble proteins, including peaks at 1002 cm^{-1} (phenylalanine) and 1656 cm^{-1} (Amide I). Some Raman bands are observed exclusively in the BCARS setup. The ER spectra prominently display Raman peaks corresponding to proteins (1002 cm^{-1}, phenylalanine; 1257 cm^{-1}, Amide III; 1655 cm^{-1}, Amide I) and lipids (715 cm^{-1}, cholesterol; 1446 cm^{-1}, CH_2). These biochemical features align with the composition of the ER, which consists of a complex network of lipid-containing vesicles and cisternae involved in protein and lipid biosynthesis and functionalization. Lysosomal spectra exhibit complex Raman features primarily attributed to sugars (851 cm^{-1}) and lipids (1078 cm^{-1},$C-C$; 1334 cm^{-1}, CH_3CH_2). Data obtained from the analysis of mitochondria-associated membranes (MAM) demonstrate intense lipid-related bands (1050 cm^{-1} and 1144 cm^{-1}), particularly in the BCARS spectra and to a lesser extent in the SR spectrum. This discrepancy may be attributed to the acquisition of SR data in an aqueous buffer, potentially reducing the

concentration of MAM-specific molecules. Mitochondrial spectra, in SR and BCARS setups, exhibit a distinct band around 785/790 cm^{-1} typically associated with nucleic acids (pyrimidine), indicating the presence of mitochondrial DNA. Additionally, mitochondria display peaks related to proteins (1002 cm^{-1}, 1146 cm^{-1}, 1250 cm^{-1}, 1658 cm^{-1}). The SR spectrum of the nucleus reveals two DNA bands around 790 cm^{-1} and 1070 cm^{-1}, along with peaks associated with proteins (1002 cm^{-1}, 1658 cm^{-1}). Conversely, the BCARS spectrum does not clearly exhibit the DNA bands.

In order to ensure the repeatability of our BCARS measurements, I conducted a comparative analysis between the BCARS spectra obtained at POLIMI and those obtained at IPHT. By comparing measurements taken using different setups, I aimed to evaluate the consistency of our results. Remarkably, the measurements, shown in Figure 4.3 exhibited a high degree of similarity, particularly when analyzing the nucleus, lysosomes, mitochondria, and endoplasmic reticulum. Considering that these samples were studied in two distinct laboratories, on different days, and under similar but slightly varied experimental conditions, these findings are quite promising.

However, it is worth noting that certain differences were observed, particularly in the MAM spectrum around the 1400 cm^{-1} region associated with lipids. Specifically, the BCARS spectrum obtained at POLIMI exhibited additional bands that were not observed when using the IPHT setup. This disparity may be attributed to the inherent heterogeneity present in dried samples, which can sometimes result in granules containing different substances randomly distributed on the optical substrate.

Furthermore, it is noteworthy that in the cytoplasm, specific Raman bands were solely observed when utilizing the BCARS setup at POLIMI, indicating potential variations in molecular composition or structural characteristics.

In conclusion, our investigation into the repeatability of BCARS measurements has yielded promising and encouraging results. The high degree of similarity observed between the BCARS spectra obtained at POLIMI and IPHT demonstrates the robustness and reliability of this technique in generating consistent and reproducible spectral data. Notably, the spectral features generated by BCARS closely align with those obtained through conventional SR techniques, encompassing both Raman shift and relative peak intensities. This remarkable consistency in spectral data not only validates the effectiveness of BCARS as a powerful analytical tool but also enhances its credibility for various applications. Also, this agreement is observed despite the examination of the samples in two separate setups, on different days, and under similar but distinct experimental conditions involving variations in laser parameters, acquisition time, data pre-processing, and sample preparation prior to measurement.

While certain differences have been identified between BCARS and SR approaches, it is

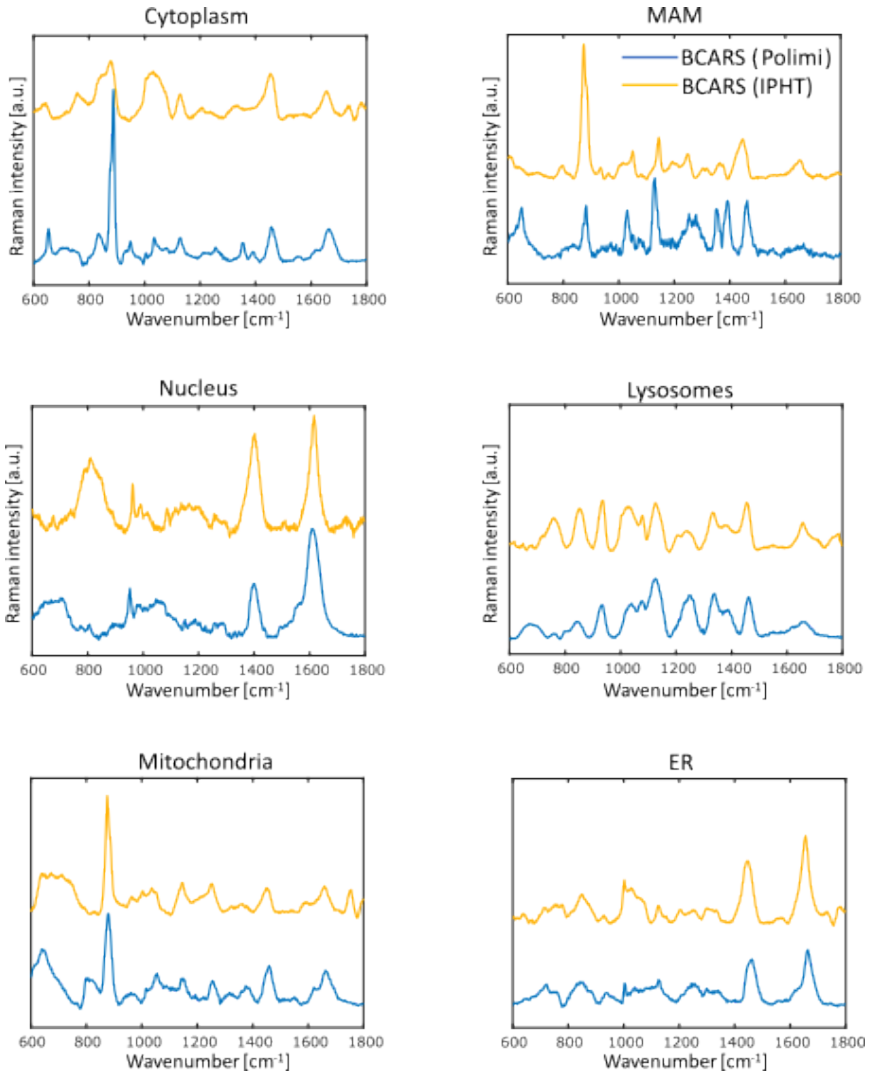

Figure 4.3: The figure showcases the BCARS spectra of subcellular components obtained using the setup at POLIMI, represented by the blue curve, and those acquired with the IPHT setup, depicted by the yellow curve.

essential to acknowledge that these disparities can be attributed to variations in sample conditions. Specifically, SR measurements were conducted using samples in solution, whereas BCARS measurements were performed on dried samples. Such variances in sample preparation can account for a portion of the observed differences between the two techniques.

Furthermore, the majority of spectra acquired through BCARS approaches offer valuable and specific information about the biochemical composition of distinct subcellular components. This finding underscores the ability of BCARS techniques to extract meaningful insights from cellular components, contributing to a comprehensive understanding of cellular structures and functions.

4.2. Cellular segmentation and PCA on HepG2 and HeK293 cells

In this section, I present an analysis of a large dataset of BCARS spectra of cells. The cells were fixed on a $22 \times 22 mm^2$ and $170 \mu m$ thick quartz coverslip. For the measurement, I adopted a sandwich configuration using a $25 \times 50 mm^2$ and $170 \mu m$ thick quartz coverslip on which I released a drop of PBS and then stuck the sample coverslip using enamel. The dataset was obtained by acquiring several $400 \times 400 \mu m^2$ images with a pixel size of $1 \mu m$ and integration time of $1 ms$. Two different human cell lines were used in the analysis: HepG2 and Hek293. These cell lines were chosen due to their extensive use in scientific research. HepG2 cells are derived from human liver cancer, while HeK293 cells are derived from human embryonic kidneys. Furthermore, measurements were conducted on samples derived from two different cultures for each cell line.

Following image acquisition, I performed a cellular segmentation to retrieve the average spectrum of the cells within the sample. To accomplish this, I transferred the BCARS image at the Raman shift of 2850 cm^{-1} to ImageJ and utilized the freehand selection option to select the borders of different regions of interest. The first region of interest selected was a cell-free area, providing a measure of the background. I then created a binary mask within the border, with a value of 1 inside and 0 outside, and multiplied it by the CARS signal on MATLAB to compute the average spectrum. This process provided the reference NRB for the specific image being considered. Different NRBs were found every time a new image was analyzed, or if a region far from the area used to extract the NRB was being considered within the same image. The other regions of interest were the cells, and I applied the previous procedure for each cell to obtain its average spectrum. I delimited the cell border on ImageJ, created a mask that was multiplied with the CARS signal, and applied spatial denoising and Kramer-Kronig with the NRB removal using the reference NRB found earlier. In Figure 4.4, I can see a portion of the sample that was analyzed, with a yellow line that delimits the perimeter of a cell and the region from which I retrieved the NRB. I then computed the average spectrum to obtain the average spectrum of a single cell. This process was repeated for every cell that was distinguishable in the image.

It is worth highlighting that the HeK293 cells have a lower signal intensity than the HepG2 cells. Moreover, the second batch of HeK293 cells had a higher cell density than the first batch, making it more challenging to find the area to retrieve the NRB and distinguish cells from one another and from the background. Additionally, the measurements on HeK293 are more reliant on the selection of the reference NRB compared to the case

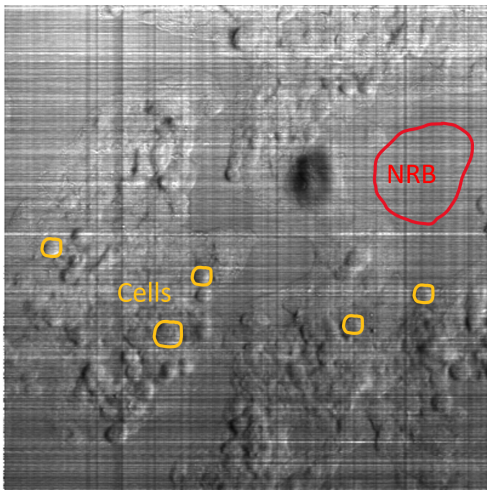

Figure 4.4: The figure displays an image of the HepG2 cell sample obtained at the Raman shift of 2850 cm^{-1}. The yellow perimeter represents the cell boundary, while the red area corresponds to the region from which the reference NRB was extracted.

of HepG2.

After acquiring the dataset for the two cell lines from different batches, I conducted a quality control to filter out cells with spectra that displayed higher levels of noise and artifacts. In Figure 4.5 are reported seven average spectra for the HepG2 cell line from the first and second batches, as well as for the HeK293 cell line.

Furthermore, Figure 4.6 showcases the average spectrum of all the cells belonging to the HepG2 and HeK293 lines, with the standard deviation depicted in grey for each Raman shift. The spectrum of HepG2 cells exhibits several distinctive peaks, including those related to, CH stretch at 2902 cm^{-1}, lipids at 2852 cm^{-1}, triglycerides at 1745 cm^{-1}, Amide I at 1655 cm^{-1}, amide II at 1570 cm^{-1}, CH_2 bending mode of proteins and lipids at 1446 cm^{-1}, CH_3, CH_2 wagging of proteins at 1335 cm^{-1}, lipids at 1300 cm^{-1}, triglycerides at 1264 cm^{-1}, hydroxyproline and tyrosine at 1206 cm^{-1}, $C = C/C - N$stretching of proteins at 1160 cm^{-1}, $(C - N)$ of proteins at 1123 cm^{-1}, DNA and $C - N$ stretching at 1094 cm^{-1}, CH_2, CH_3 bending mode of phospholipids at 1032 cm^{-1}, phenylalanine of proteins at 1005 cm^{-1}, ring breathing of tyrosine of proteins at 854 cm^{-1}, $O - P - O$stretching of DNA/RNA at 828 cm^{-1}, and DNA at 786 cm^{-1} and at 721 cm^{-1}.

On the other hand, the spectrum of HeK293 cells displays several distinct peaks, including those associated with symmetric CH_3 stretch, primarily in proteins at 2947 cm^{-1}, lipids at 2852 cm^{-1}, Amide I at 1665 cm^{-1}, $C = C$ bending mode of phenylalanine at 1583 cm^{-1}, CH_2 bending mode of proteins and lipids at 1455 cm^{-1}, $C - N$ stretching at 1392 cm^{-1}, the region related to DNA and phospholipids at 1330 cm^{-1}, CH_2 twisting of lipids at 1300 cm^{-1}, Amide III at 1265 cm^{-1}, stretching of $C - N$ at 1216 cm^{-1}, tyrosine at 1163

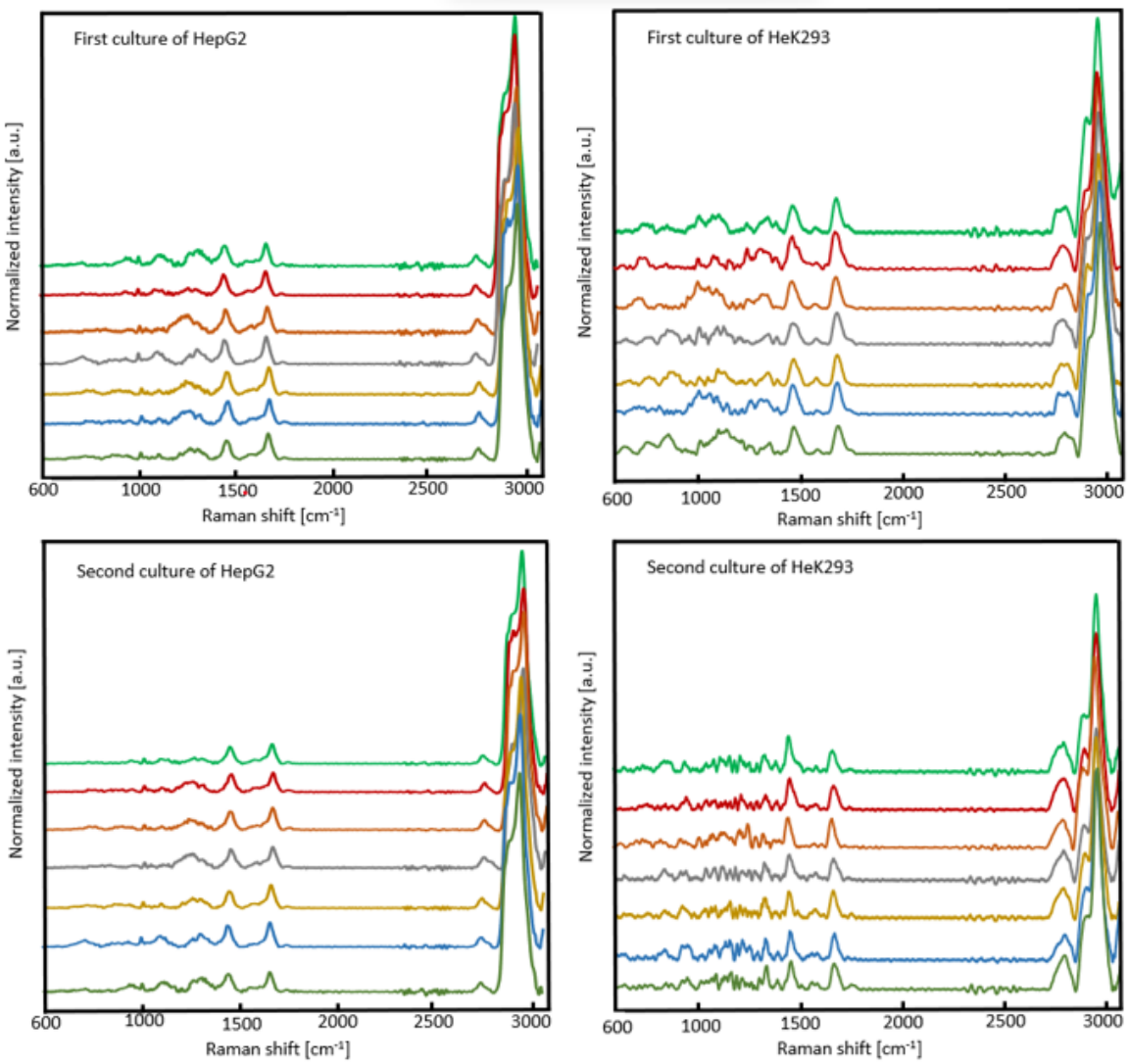

Figure 4.5: The figure reports seven average spectra for the HepG2 cell line from the first and second batches, as well as for the HeK293 cell line.

cm^{-1}, $C = C$ stretch at 1121 cm^{-1}, lipid at 1095 cm^{-1}, proteins at 951 cm^{-1}, tyrosine ring breathing at 852 cm^{-1}, DNA: $O - P - O$ at 786 cm^{-1}, and DNA at 752 cm^{-1}. It is worth noting that the ratio between the peak at 1666 cm^{-1} and 1455 cm^{-1} is different in the two spectra, with the higher peak being at 1666 cm^{-1} in HepG2 and at 1455 cm^{-1} in HeK293. Additionally, the presence of the triglyceride peaks at 1745 cm^{-1} and 1264 cm^{-1} and intense peaks associated with lipids at 2852 cm^{-1} and 1300 cm^{-1} in HepG2 suggests a higher concentration of lipids in these cells compared to HeK293. These observations align with the fact that HepG2 cells are derived from the liver and are known to be richer in lipids than HeK293 cells.

To validate the qualitative analysis, a statistical analysis based on Principal Components

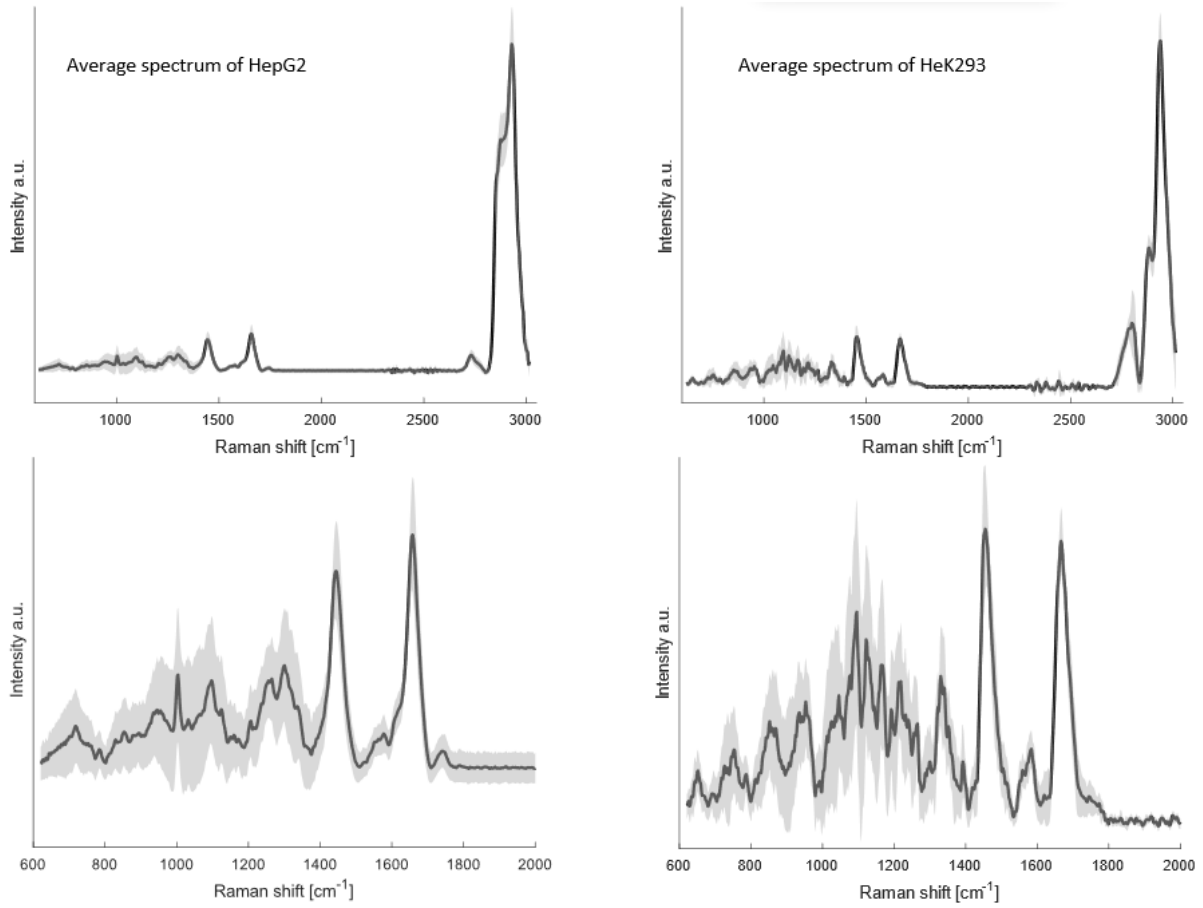

Figure 4.6: The figure illustrates the average Raman spectra of the HepG2 and HeK293 cell lines, with the shaded gray region indicating the standard deviation at each Raman shift. To better visualize the spectral differences between the two cell lines, the fingerprint region is zoomed in and displayed below the full spectra.

Analysis (PCA) was performed. A subclass of cells was selected from different cell lines and batches to perform the PCA. The Explain vector of the PCA, which contains the percentage of the total variance explained by each principal component, was plotted in Figure 4.7.

It was observed that the first principal component (PC1) explains the highest percentage of the total variance in the dataset, indicating that it can distinguish between cells belonging to different lines. Other principal components were less relevant to explain the variance of the problem. Figure 4.8 shows the projection of the data on the first three principal components and the plot PC1vsPC2 demonstrates that PC1 can distinguish between cells belonging to HepG2 lines and HeK293 lines. HepG2 cells represented by red and blue asterisks have positive values of PC1, while HeK293 cells represented by black and green dots have negative values of PC1. This behavior can also be seen in the plot

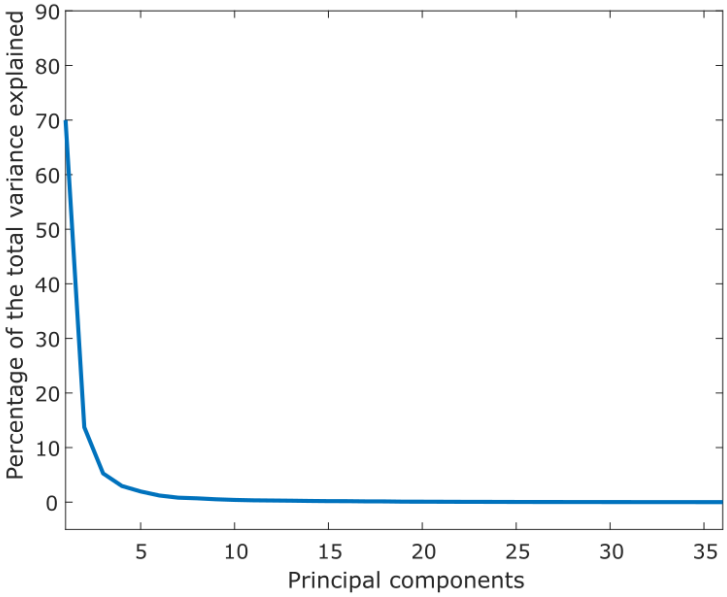

Figure 4.7: The plot illustrates the Explained Vector obtained through PCA, displaying the percentage of total variance explained by each principal component.

that shows the distribution of cells on PC1. In addition to the above, I found that PC2, while explaining a relatively small portion of the total variance, can effectively distinguish between different batches of HeK293 cells, but not for HepG2 cells. This could be attributed to the fact that the two batches of HeK293 cells had different densities, resulting in a slightly different accuracy of the analysis. Nevertheless, our statistical analysis based on Principal Components Analysis has successfully demonstrated the capability of the BCARS setup to distinguish between different cell lines.

To further explore our analysis, I examined the loading of the first principal component, which represents the eigenvector of PC1 (Figure 4.9). Given the substantial differences between the two cell lines and the fact that PC1 accounted for most of the total variance, I expected the loading to reflect the spectrum differences between the two lines. As HepG2 cells have positive values of PC1, positive peaks in the loading correspond to the HepG2 cell line, while negative peaks correspond to the HeK293 cell line. Analysis of the loading of PC1 revealed that HepG2 cells have higher concentrations of some elements, corresponding to peaks at 2902 cm^{-1} (CH_2 stretch of lipids and proteins), 2852 cm^{-1} (CH_2 symmetric stretch of lipids), 1745 cm^{-1} (triglycerides), 1655 cm^{-1} (Amide I), 1530 cm^{-1} (vibrations of CC and CN in lipids and nucleic acids), 1429 cm^{-1} (Deoxyribose, a component of DNA), 1300 cm^{-1} (Lipids), and 1000 cm^{-1} (phenylalanine). On the other hand, HeK293 cells have higher concentrations of elements with peaks at 2947 cm^{-1} (CH_2 vibrations in proteins), 2807 cm^{-1} (CH_2 vibrations in lipids and proteins), 1663

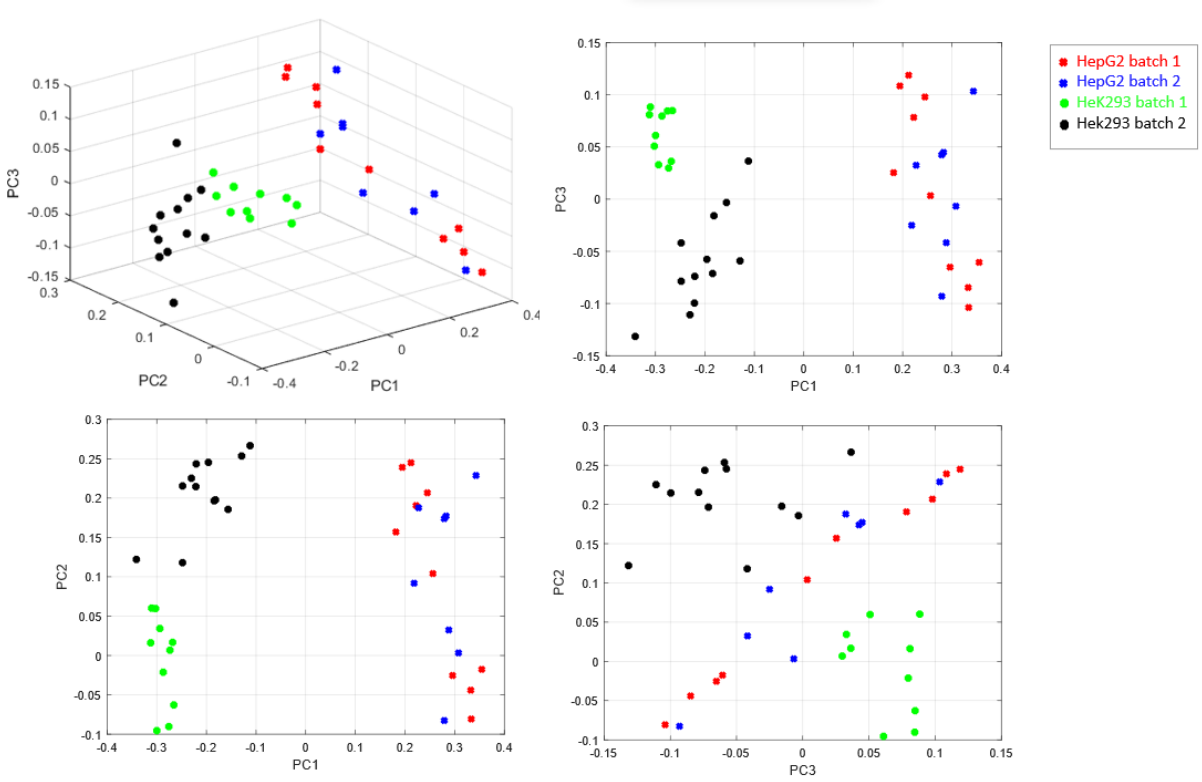

Figure 4.8: The figure displays the projection of the data onto the principal components (PCs). The top-left plot represents the projection of the data onto the first three PCs, while the top-right, bottom-left, and bottom-right plots show the projection onto specific combinations of PCs, namely PC3 and PC1, PC2 and PC1, and PC2 and PC3, respectively. In the figure, cells from the first batch of the HepG2 line are indicated with red asterisks, while those from the second batch are represented with blue asterisks. Similarly, cells from the first and second batches of HeK293 are denoted with green and dark dots, respectively.

cm^{-1} (DNA and proteins), 1585 cm^{-1} (phenylalanine), 1464 cm^{-1} (lipids), and 1330 cm^{-1} (region associated with DNA and phospholipids). The majority of the peaks observed in the spectra were also present in the average spectrum of both cell lines. The dominance of the peaks at 2850 cm^{-1} and 1300 cm^{-1} in HepG2 suggests that this cell line is richer in lipids, while the peak at 1000 cm^{-1} indicates a higher concentration of phenylalanine. Conversely, the HeK293 line appears to be richer in proteins, as evidenced by the peak at 2947 cm^{-1} associated with proteins and the peak at 1665 cm^{-1} associated with amide I. The fact that the other principal components accounted for only a small amount of variance suggests that the only factor capable of distinguishing between different cell types was the cell line, with no other factors contributing to variability in the dataset such as artifacts, sample preparation or variations in experimental conditions. Finally, as a final

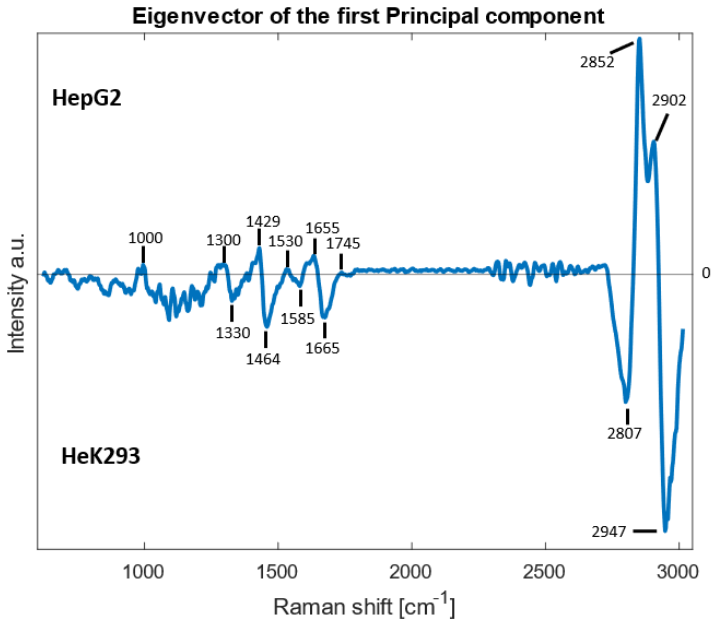

Figure 4.9: The plot of the eigenvector of PC1 highlights the peaks associated with the HepG2 and HeK293 cell lines.

check of the quality of our analysis, I calculated the spectrum difference and compared it with the loadings of PC1, as shown in Figure 4.10. As expected, the two spectra were almost identical, providing further evidence for the accuracy of our results.

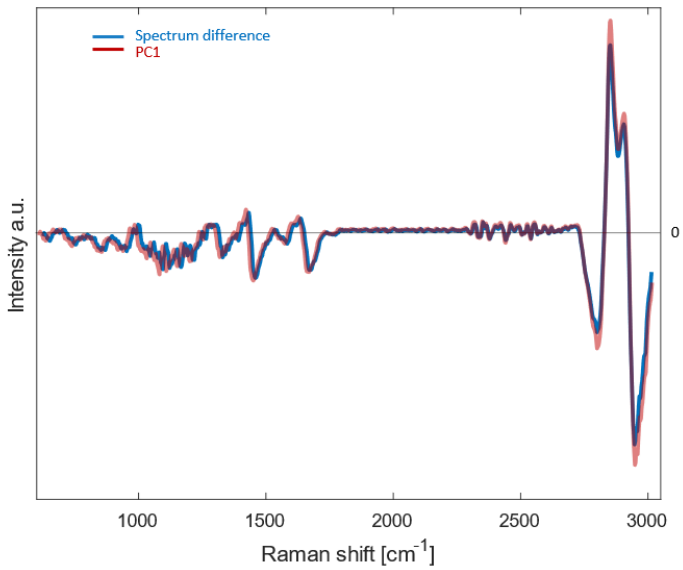

Figure 4.10: The figure shows the overlap between the spectrum difference of the average spectra of HepG2 and HeK293 cells (blue) and the eigenvector of PC1 (red).

4.3. BCARS imaging of NASH samples

In the current section, I show that BCARS is a promising technique in biomedical imaging for identifying NASH from healthy tissue. In experiments using biological samples affected by non-alcoholic steatohepatitis (NASH) and control tissue, it is demonstrated the potential of BCARS in diagnosing NASH.

NASH is a liver disease closely related to non-alcoholic fatty liver disease (NAFLD), characterized by inflammation and damage to liver cells caused by a build-up of fat in the liver without alcohol abuse [94]. NASH is a severe form of NAFLD, leading to scarring (fibrosis) of the liver, which can progress to cirrhosis and liver failure, increasing the risk of liver cancer and cardiovascular disease. NASH affects an estimated $3-12\%$ of the general population and is most commonly diagnosed in people aged 40 to 60, but can occur at any age. Diagnosis typically involves a combination of medical history, physical exam, blood tests, imaging tests such as ultrasound or MRI, and liver biopsy [95]. However, these techniques can be complex, potentially disruptive, can require specific fluorescent labeling, and can require enzymological, biochemical, histological, transcriptomic, and omics analyses of the liver. The effects of NASH on the human body can vary in severity, ranging from mild cases with no noticeable symptoms to more advanced cases leading to fatigue, weakness, abdominal pain, and swelling. NASH can also increase the risk of developing other health conditions such as type 2 diabetes, cardiovascular disease, and metabolic syndrome. Biologically, NASH affects liver tissue by causing the accumulation of fat (steatosis) in liver cells, oxidative stress, and the formation of fibrous tissue (fibrosis), ballooned hepatocytes, fatty hepatocyte foci, inflammation, and increased hepatocyte cell death [96]. These changes can lead to liver cell injury and death, causing scarring and permanent damage to liver tissue [97]. Microscopic examination of liver tissue affected by NASH typically shows features such as ballooning degeneration of liver cells, inflammation, and fibrosis, with severe cases showing signs of cirrhosis, such as nodules and bridging fibrosis [98]. Not all individuals with NAFLD will develop NASH, and not all cases of NASH will progress to cirrhosis or liver cancer, but NASH is a significant public health concern due to its potential to cause serious liver-related and non-liver-related complications. Early detection and management of NASH are essential for preventing disease progression and improving long-term health outcomes.
In our experiment, I acquired different BCARS images of both tissues affected by NASH and healthy tissue. I image a large field of view of $10\mu m$ thick liver tissue slices obtained from a control sample and from a liver isolated from a NASH mice model. In

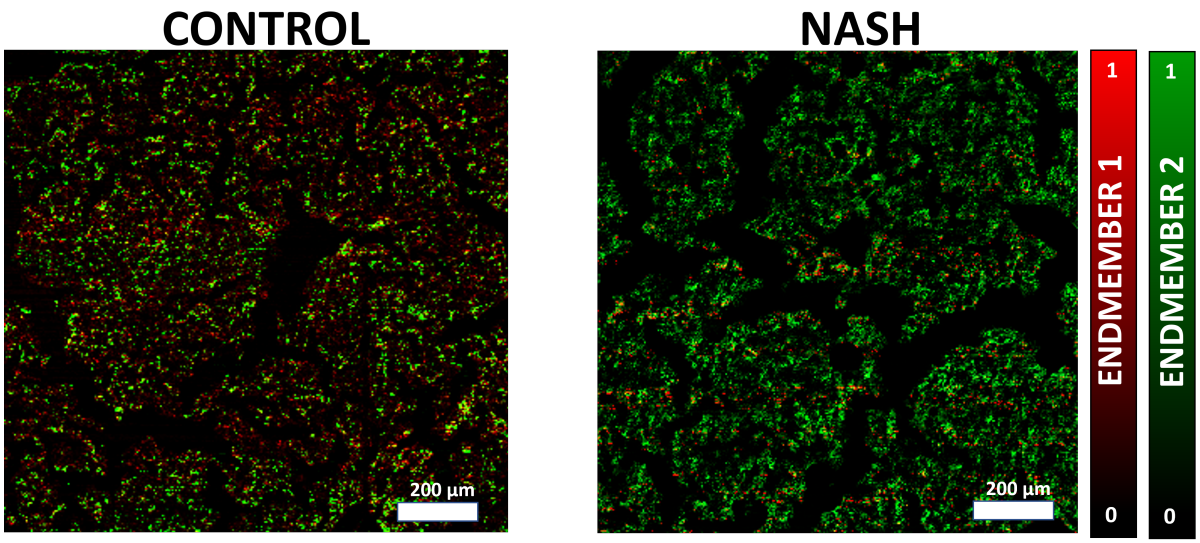

(a)

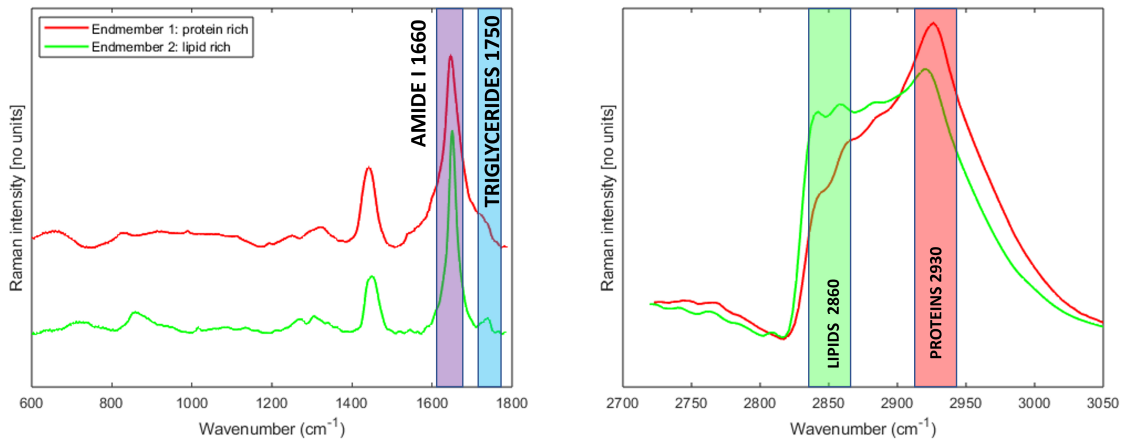

(b)

Figure 4.11: Figure (a) represents the concentration map of the two endmembers obtained by using the N-FINDR algorithm on the NASH liver slice for both NASH and control. Figure (b) illustrates the spectra of the two endmembers, highlighting the distinct characteristics of each. The red line represents the spectra of the protein-rich endmember, while the green line corresponds to the lipid-rich endmember. Additionally, the Figure identifies the prominent peaks associated with Amide I, triglycerides, proteins, and lipids.

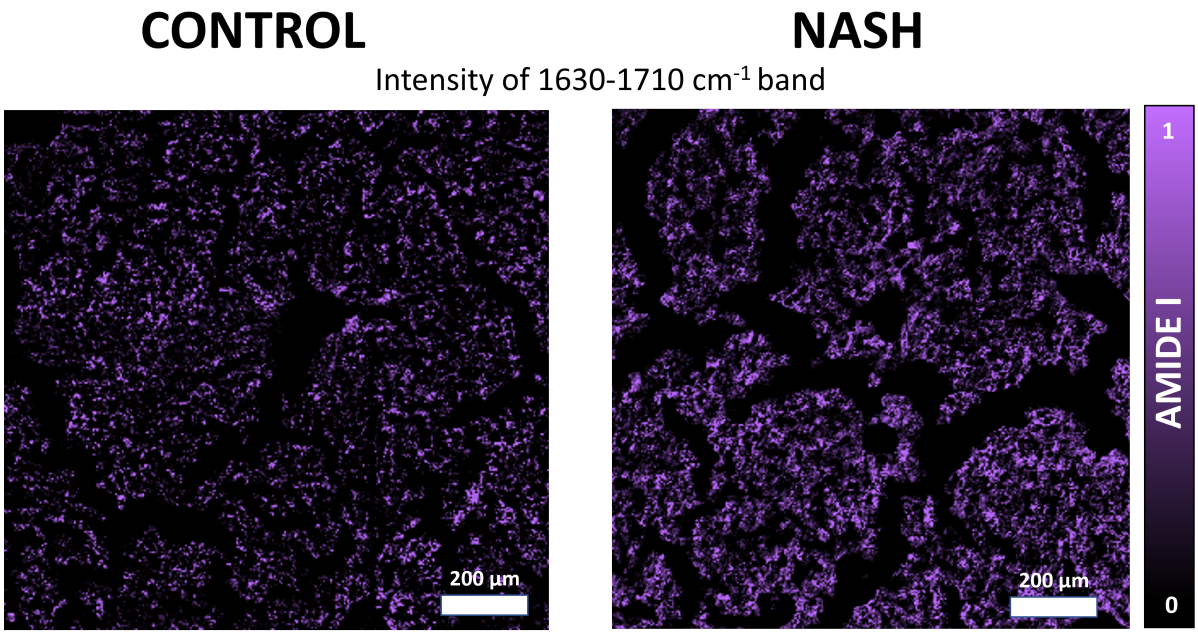

(a)

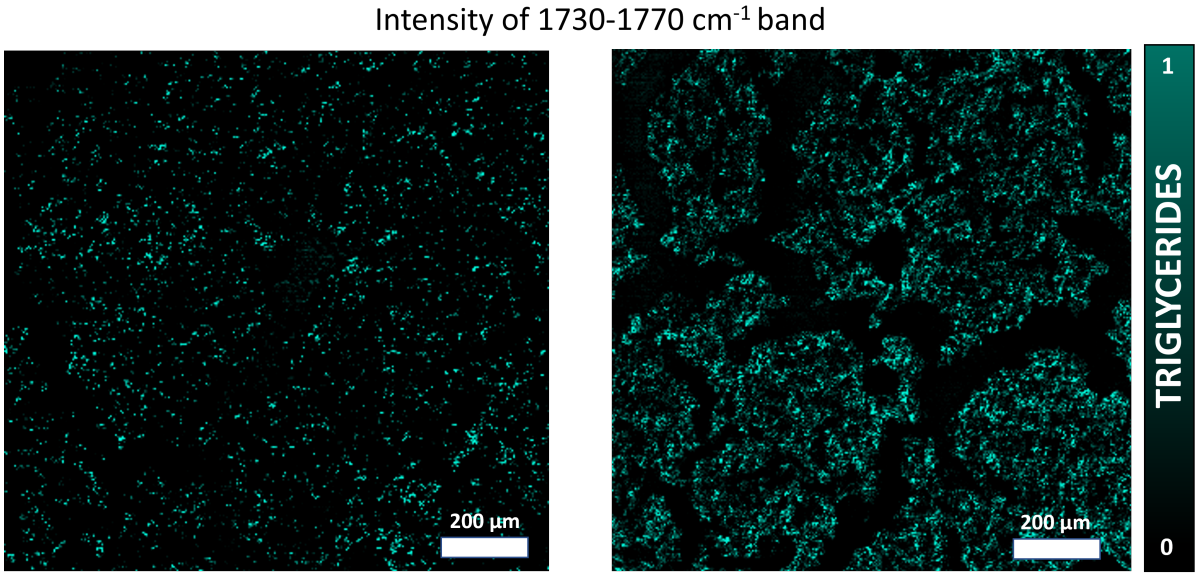

(b)

Figure 4.12: Figure (a) shows the concentration map of Amide I for both control and NASH, integrating into the band 1730-1770 cm^{-1}. Figure (b) displays the concentration map of triglycerides for both control and NASH, integrating into the band 1730-1770 cm^{-1}.

both samples, I imaged a $800 \times 800\mu m^2$ region and set a pixel size of $2 \times 2\mu m^2$ with $3ms$ pixel dwell time. After denoising and NRB removal, the images were analyzed using RamApp software (https://beta.ramapp.io). Only the most relevant and characteristic images for control and NASH tissue were considered in the following description. Firstly, utilizing a K-means analysis, I successfully differentiated between the foreground and the substrate. Subsequently, employing the unsupervised N-FINDR algorithm exclusively on the foreground, I identified two primary endmembers showcasing distinctive spectra characterized by peaks occurring at varying wavenumbers (Figure 4.11a), such as 645 cm^{-1} ($C-C$ twisting mode of phenylalanine (proteins)), 831 cm^{-1} (DNA/protein), at 1005 cm^{-1} (Phenylalanine (proteins)), 1125 cm^{-1} ($C-C$ stretch of proteins and lipids), 1257 cm^{-1} (lipids band), 1325 cm^{-1} (lipids), 1450 cm^{-1} (CH_2 bending), 1567 cm^{-1} (amide II), 1660 cm^{-1} (Amide I) and 1750 cm^{-1} (triglycerides). In the high-wavenumber regions, the main peaks are the one at 2850 cm^{-1} associated with the CH_2 symmetric stretch of lipids, at 2874 cm^{-1} typical of the CH_2 asymmetric stretch of lipids, and at 2930 cm^{-1} of the CH_3 stretching of proteins. Both endmembers exhibit distinct signatures of proteins and lipids. The red endmember represents the protein-rich component, characterized by a prominently intense peak at 2930 cm^{-1}. On the other hand, the green endmember represents the lipid-rich component, distinguished by a highly pronounced peak at 2860 cm^{-1}, along with additional peaks corresponding to triglycerides at 1750 cm^{-1}. Figure 4.11b, representing the concentration map of the two endmembers, shows that the control slice is characterized by a large amount of endmember 1 (proteins rich) compared to the NASH slice, where there is a higher concentration of the lipidic component, indicating an accumulation of fat (steatosis). In contrast, the dominant component in the control slice is the protein-rich endmember 1. By analyzing the spectra obtained with the N-FINDR algorithm, I can unveil another interesting property. Specifically, the endmember 2 exhibits a distinct peak at 1750 cm^{-1} that is characteristic of triglycerides, which is nearly absent in the endmember 1. Moreover, both spectra display a very intense peak at 1660 cm^{-1} that is characteristic of Amide I. Therefore, I integrate the two images in the spectral band between 1730-1770 cm^{-1} and 1630-1720 cm^{-1} in order to obtain the concentration map of triglycerides and Amide I, respectively. In figure 4.12b the concentration map of triglycerides of both the control and NASH slice is shown. It can be observed qualitatively that the concentration of triglycerides in the NASH tissue is higher than that in the control tissue. Figure 4.12a, which displays the concentration of AMIDE I, shows a slighter higher concentration of AMIDE I in NASH with respect to the control. These results are consistent with previous studies [99–102] that report an accumulation of triglycerides in non-alcoholic fatty liver disease and NASH and pave the way for an exploration of the role of triglycerides in different NASH phenotypes using BCARS microscopy.

In conclusion, our study demonstrated that BCARS can be used to identify NASH regions and distinguish them from healthy portions in thin tissue slides.

4.4. BCARS coupled with SHG

The paragraph highlights the immense potential of BCARS microscopy in conjunction with SHG microscopy for advancing biological studies. Through the seamless fusion of both techniques, I gained a remarkable advantage, obtaining highly precise and comprehensive insights into the morphology and chemical properties of the sample, all without the need for labeling.

The biological tissue that I consider is breast tissue containing microcalcifications. Microcalcifications are minute mineral deposits composed of calcium phosphate crystals that form within breast tissue as a result of various biological processes [103]. These processes include normal cellular turnover, which occurs naturally with aging and leads to the shedding of cells from the breast tissue. Microcalcifications can also arise from inflammation, such as in the case of breast tissue that has been affected by an infection or injury. Additionally, certain benign breast conditions like fibroadenomas or cysts can lead to the formation of microcalcifications. Microcalcifications can also be an early sign of breast cancer. As abnormal cells, including cancer cells, grow and multiply within breast tissue, they can cause calcium to accumulate in the surrounding tissue, leading to the formation of microcalcifications. Detecting microcalcifications is therefore crucial in the screening and diagnosis of breast cancer. Mammography is the primary imaging technique used to detect microcalcifications [104]. This technique produces detailed images of breast tissue that enable doctors to identify any abnormal deposits, including microcalcifications. If microcalcifications are detected, further testing may be required, such as a biopsy, to determine whether they are benign or malignant.

In recent years, BCARS microscopy has emerged as a promising imaging technique that could enhance the detection and diagnosis of microcalcifications in breast tissue [105]. This technique provides high-resolution imaging of biological tissue, offering detailed information about tissue structure and composition without the need for labeling or staining. So, BCARS microscopy can be used to detect and characterize microcalcifications in breast tissue with high accuracy and sensitivity and may have the potential to improve the early detection and diagnosis of breast cancer.

In this section, I introduce the initial technique for performing multimodal microscopy, which relies on altering the central wavelength of the grating of the spectrometer to detect sequentially the BCARS and SHG signals. This approach is relatively straightforward, cost-effective, and easy to implement. However, it comes with the drawback of extended

acquisition time, as the detection of BCARS and SHG signals occurs sequentially.
In the second part of this section, I present an innovative configuration for our microscope, enabling simultaneous detection of BCARS and SHG signals by incorporating a Photomultiplier Tube (PMT). This new setup addresses the limitation of the previous technique, significantly reducing the acquisition time.

4.4.1. Coupling BCARS with SHG Detection Using a Spectrometer

In our experiment, $400 \times 400 \mu m^2$ BCARS images on sections of breast tissue containing microcalcifications are acquired with an integration time of $8ms$. The sample is prepared in a sandwich configuration between a $25 \times 50 mm^2$ and 170 μm thick quartz coverslip and $22 \times 22 mm^2$ and 170 μm thick coverslip. The BCARS data are post-processed using SVD and NRB removal and calibrated with measurements taken from toluene. The images are analyzed using the RAMAPP software, which utilizes the k-means algorithm to cluster the image and identify the foreground and the substrate that need to be removed. The N-FINDR algorithm is used to find and separate different chemical species.
The SHG signal is acquired separately from the BCARS signal in the same region of interest of the sample by changing the central wavelength of the grating of the spectrometer from 885 nm to 500 nm with a pixel dwell time of 15 ms. In Figure 4.13 the SHG spectrum of a single pixel is reported. The SHG signal, which shows a peak between 1414 cm^{-1} and 1435 cm^{-1}, is analyzed on RAMAPP. The resulting images are built by overlapping both the SHG and BCARS signals. Several images are acquired but only the most significant is reported.

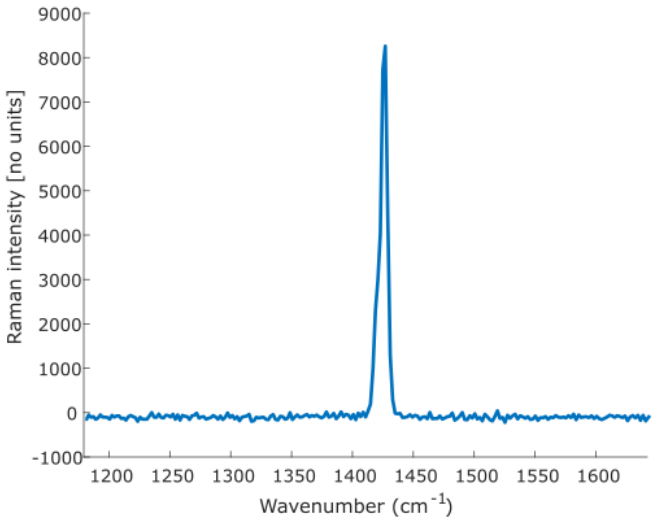

Figure 4.13: SHG signal from a single pixel.

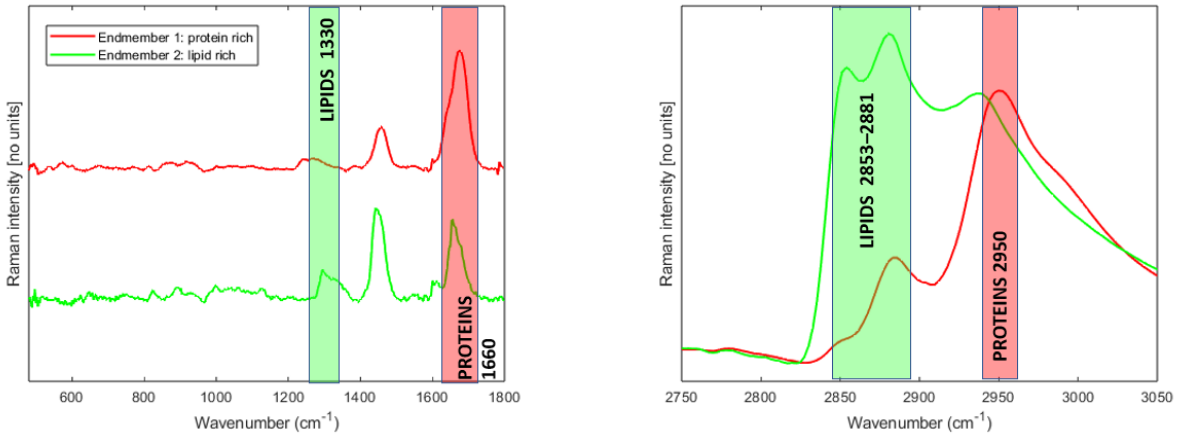

Figure 4.15: The Figure illustrates the spectra of the two endmembers, highlighting the distinct characteristics of each. The red line represents the spectra of the protein-rich endmember, while the green line corresponds to the lipid-rich endmember. Additionally, the Figure identifies the prominent peaks associated with proteins and lipids.

Two main endmembers are identified by the BCARS signal, one is represented by green and the other by red color as shown in Figure 4.14 that displays the corresponding concentration map. In Figure 4.15 are reported the spectrums of these two components. The blue color shows the regions in which the SHG signal is present. The red species exhibits distinctive characteristics indicating its composition primarily comprises proteins. This inference is supported by the presence of a Raman peak at 1660 cm^{-1}, which is a hallmark of the Amide I band in proteins, along with an additional peak at 1460 cm^{-1}, representing

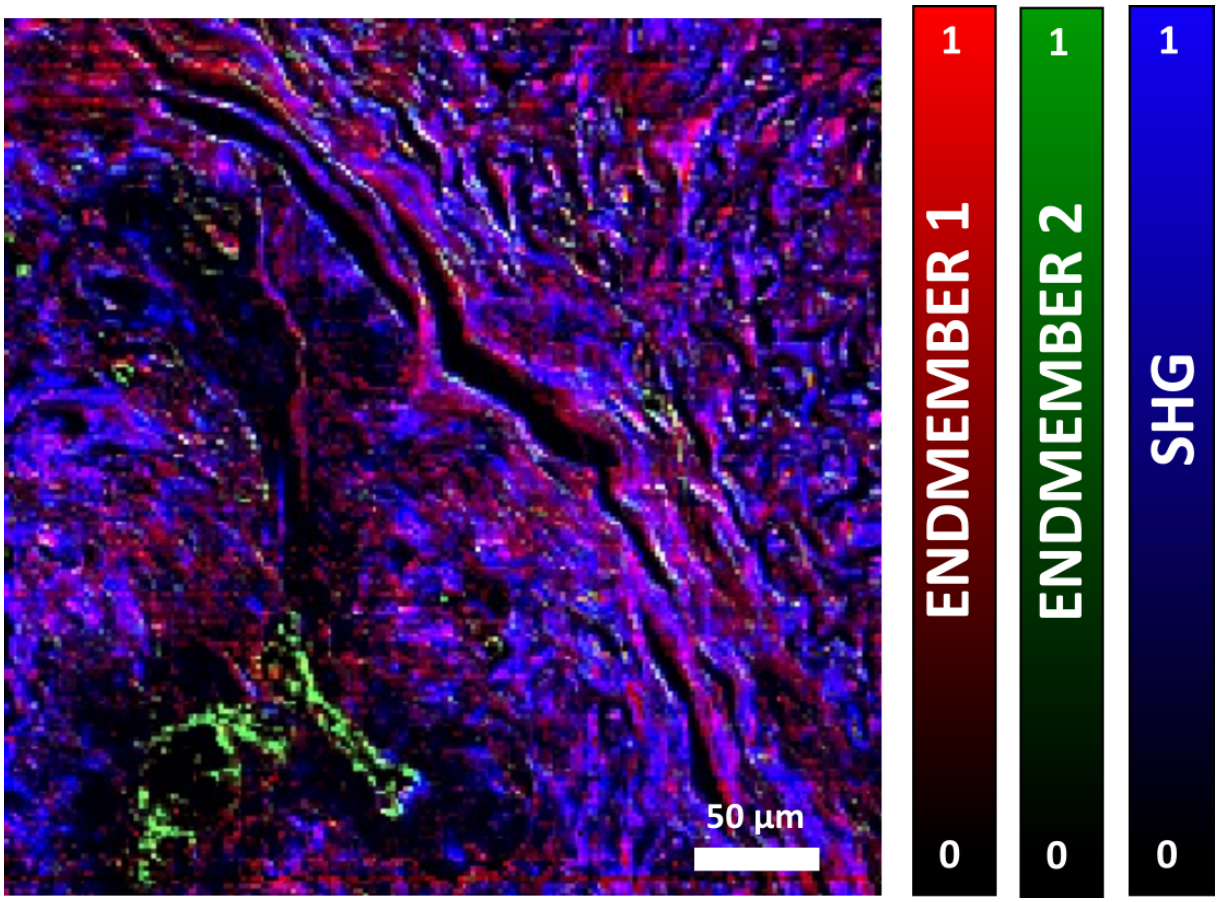

Figure 4.14: The image presents a concentration map of two endmembers generated using the N-FINDR algorithm and the SHG signal. In this map, the protein-rich endmember (endmember 1) is highlighted in red, while the lipid-rich endmember (endmember 2) is depicted in green. The blue color represents the concentration map of collagen, as indicated by the SHG signal.

the CH_2/CH_3 deformation of lipids and collagen. The distinct ratio between these two peaks, compared to the green endmember, serves as clear evidence that the red species is richer in proteins than the other component which is richer in lipids. Another peak is observed at 1270 cm^{-1}, which is characteristic of Amide III present in both collagen and proteins. At 817 cm^{-1}, there is the peak of $C-C$ stretching, which is a collagen assignment, and at 509 cm^{-1}, the $S-S$ disulfide stretching band of collagen. In the CH region, a peak is present at 2950 cm^{-1} that is characteristic of proteins. So, this endmember has different contributions from different species as collagen, lipids, and proteins, but the most relevant contributions are given by proteins due to the fact protein peaks at 1660 cm^{-1} and 2950 cm^{-1} are the most intense. The red endmember is proteins rich, but it showed also some collagen peaks. Collagen, being a non-centro-symmetric material, has a very strong SHG signal. The blue areas in Figure 4.14 represent mostly the contributions from

collagen and it is observed that the protein distribution and collagen are very similar, indicating that a significant component of the protein is given by collagen fibers, which are proteins. The green endmember, on the other hand, shows similar peaks with respect to the red endmember. But, in this case, the lipid peak at 2853 cm^{-1} and 2881 cm^{-1} that correspond to the CH_2 symmetric stretch of lipids and CH_2 asymmetric stretch of lipids and proteins, are much more intense with respect to the peaks in the spectrum of the endmembers of rich-proteins. Furthermore, the green spectrum shows additional peaks that are typical of lipids at 1330 cm^{-1} that is in-plane twist vibration (lipid band) and at 1168 cm^{-1}. In conclusion, the green species identifies rich-lipids species. Then, I retrieve the collagen spectrum alone following this procedure:

- Step 1: I integrate the SHG signal in the SHG bandwidth.
- Step 2: A suitable threshold is chosen, which is calculated as the mean value of the SHG intensity of all pixels in the image plus three times the standard deviation.
- Step 3: A mask is generated, assigning a value of 0 to pixels below the threshold (indicating no SHG signal) and a value of 1 to pixels above the threshold (indicating the presence of SHG signal).
- Step 4: The post-processed image is multiplied by the mask, effectively selecting pixels showing strong SHG signals.
- Step 5: I calculate the average spectrum from all the pixels above the threshold, which are representative of collagen due to their higher SHG intensity.
- Step 6: The substrate spectrum obtained from the analysis with Ramapp is then subtracted from the collagen spectrum.

The outcome of this procedure is illustrated in the collagen spectrum presented in Figure 4.16.

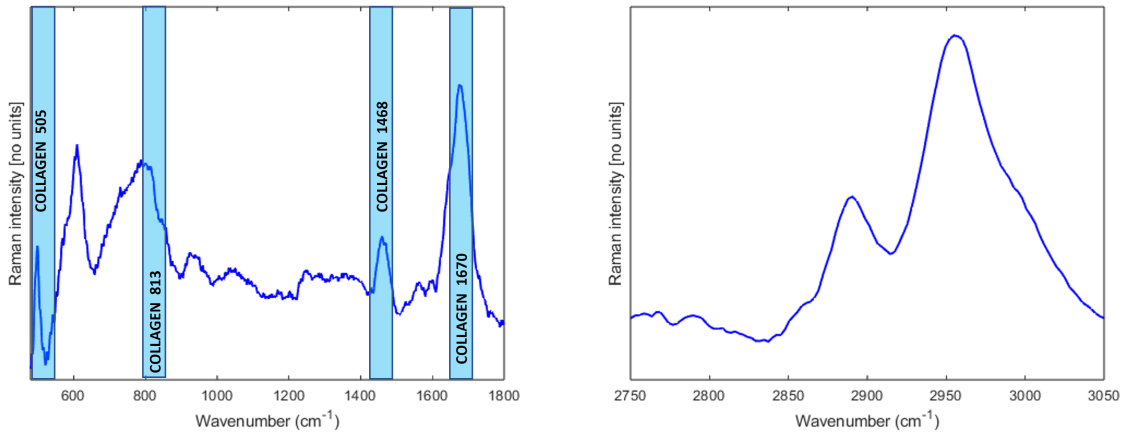

Figure 4.16: Figure depicts the retrieved spectra of the collagen where the characteristic collagen peaks are highlighted.

This information could not be retrieved using the N-FINDR algorithm, likely due to the overlapping signal from collagen with other components. Three main peaks are observed in the collagen spectrum [106], which is characteristic of collagen: 505 cm^{-1} $S-S$ disulfide stretching band of collagen, 1468 cm^{-1} CH_3, CH_2 deformation (collagen assignment), 1670 cm^{-1} Amide I (collagen assignment) and peak at 813 cm^{-1} ($C-C$ collagen assignment). These peaks are also present in the rich-protein species, indicating that proteins and collagen are strongly correlated. Also, another main peak is detected at 618 cm^{-1} associated with $C-C$ in proteins, but it is not a collagen assignment.
In order to validate the experiment, I conducted a comparison of the collagen spectrum depicted in Figure 4.17 [107]. The spectrum of unburned collagen, denoted by the blue line, exhibited identical peaks corresponding to Amide I, CH_2, and $C-C$. Although the peak of Amide III in our measurement was less pronounced, there was a significant agreement observed in the fingerprint and CH regions. These findings highlight the enhanced sensitivity and chemical specificity of our experimental setup and the subsequent data analysis techniques employed.

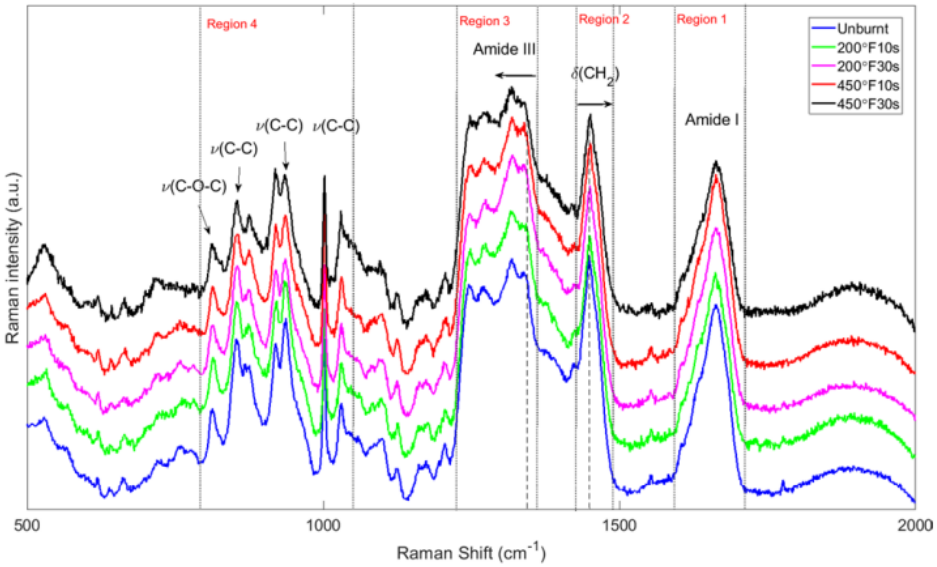

Figure 4.17: Collagen spectrum from [107].

4.4.2. Coupling BCARS with SHG Detection Using PMT

In the preceding subsection 4.4.1, I demonstrated the multimodal capabilities of our setup to detect both BCARS and SHG signals. However, the previous configuration had a significant drawback when acquiring the SHG signal using a spectrometer, resulting in a lengthy measurement time. This was due to the need to sequentially measure BCARS with an 8 ms integration time and the gratings of the monochromator were centered at the wavelength of 885 nm. Subsequently, the SHG image was acquired with a 15 ms integration time by moving the gratings to the central wavelength of 500 nm.

In this subsection, I present an improved configuration that enhances the performance of our microscope by enabling simultaneous acquisition of BCARS and SHG signals, thereby reducing the acquisition time by 15 ms per pixel compared to the previous approach. To achieve this, I employed a Photomultiplier Tube (PMT) coupled with a Data Acquisition (DAQ) system. The transmitted light from the sample is split into two branches using a dichroic filter, which transmits light above 750 nm for BCARS detection and reflects light below 750 nm for SHG signal detection. The reflected light then passes through a low-pass filter, eliminating wavelengths above 800 nm to remove any residual CARS signal and select only the SHG signal. The light is subsequently directed to the PMT, and with the assistance of the DAQ, I can now detect the SHG signal simultaneously with the BCARS signal, significantly reducing the acquisition time.

To evaluate the true potential of this configuration, I used the same sample as in the previous subsection, namely, microcalcifications in breast tissue. I acquired images of

$200 \times 200 \mu m^2$ with a pixel size of 1 μm and a integration time of 8 ms.
Both BCARS and SHG images are now acquired simultaneously. The BCARS image undergoes denoising using SVD, and the NRB is removed using the KK-algorithm. The calibrated axis is obtained from the toluene measurement performed on the same day and compared with the SR spectra of the toluene. Subsequently, both the SHG and BCARS signals are loaded into Ramapp, where I identify and remove the substrate using the k-means algorithm. Next, the N-FINDR algorithm is applied to the foreground of the BCARS image to find the endmembers. The concentration maps of these endmembers, along with the SHG image, are overlaid as shown in Figure 4.18.

The N-FINDR algorithm distinguishes two main endmembers, represented by green and

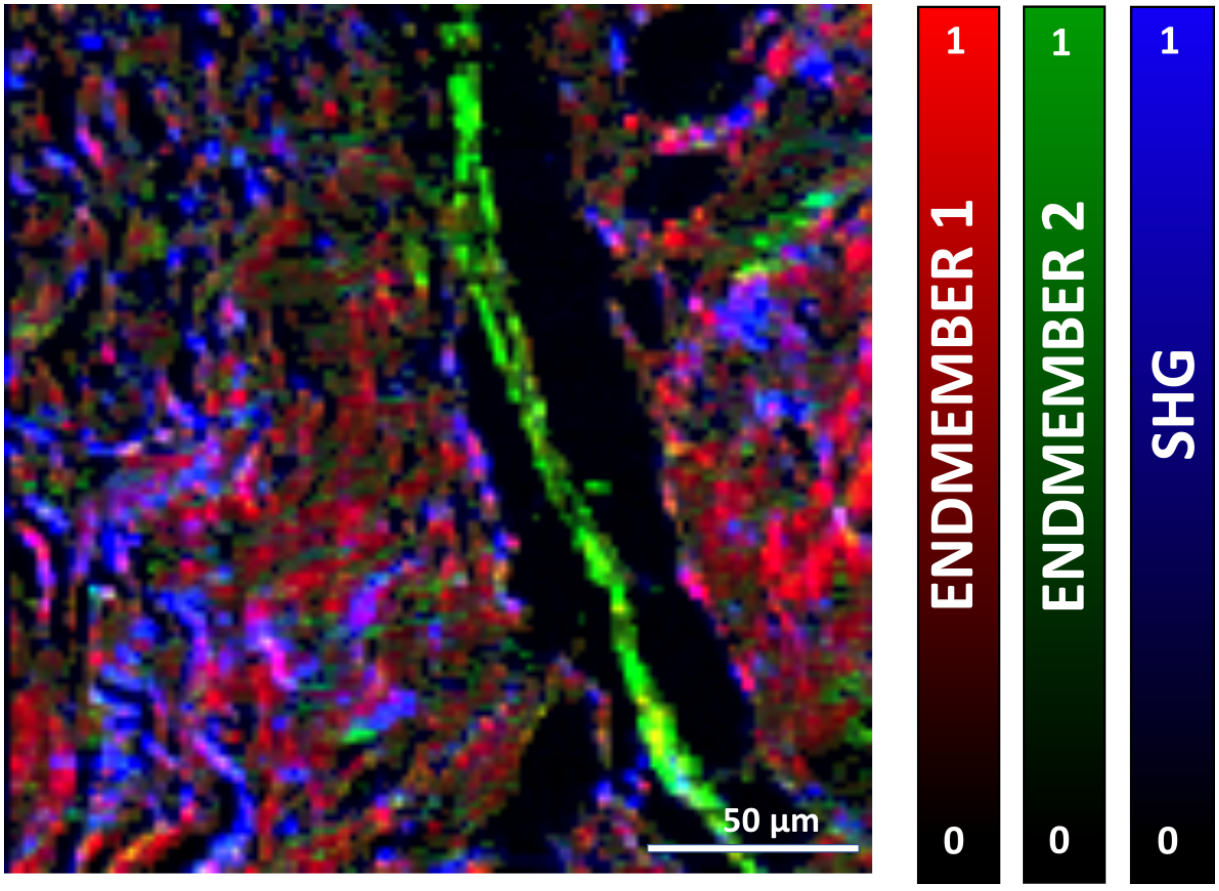

Figure 4.18: The image displays a concentration map obtained through the N-FINDR algorithm. It depicts two distinct endmembers, represented in different colors. The red color indicates regions rich in proteins, while the green color signifies areas abundant in lipids. Additionally, the concentration map of collagen is presented in blue, which corresponds to the SHG signal.

red spectra in Figure 4.19. The green endmember corresponds to lipid-rich components of the sample, exhibiting characteristic lipid peaks such as those at 1330 cm^{-1} and in the

band 2853-2881 cm^{-1}. On the other hand, the red endmember represents protein-rich components, lacking the characteristic lipid peaks but containing protein-specific peaks, such as those at 1660 cm^{-1} (associated with Amide I) and 2930 cm^{-1}.

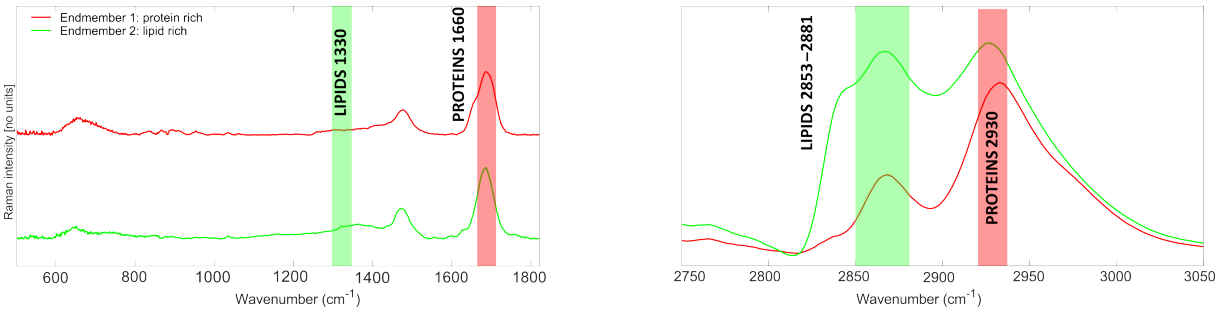

Figure 4.19: The Figure exhibits the spectra of the two endmembers, showcasing their distinct characteristics. The red line in the graph represents the spectrum of the protein-rich endmember, while the green line corresponds to the lipid-rich endmember. Within the spectra, prominent peaks associated with proteins and lipids are clearly identified.

Moving on to the SHG signal, I extracted the collagen spectrum. First, a binary mask of the SHG image is created, where pixels with intensity higher than a certain threshold are set to 1, while the others are set to 0. This mask is then multiplied with the denoised raw BCARS image, and an average spectrum is obtained. The KK-alghoritm is applied to remove the NRB, resulting in the spectrum displayed in Figure 4.20. The spectrum obtained in this subsection closely resembles the collagen spectrum acquired in the previous subsection. It exhibits characteristic collagen peaks at specific Raman shifts. These peaks include those at 505 cm^{-1}, 850 cm^{-1} (proline),938 cm^{-1} (proline), 970 cm^{-1}, 1030 cm^{-1} (Phenylalanine of collagen), 1468 cm^{-1}, and 1670 cm^{-1}.

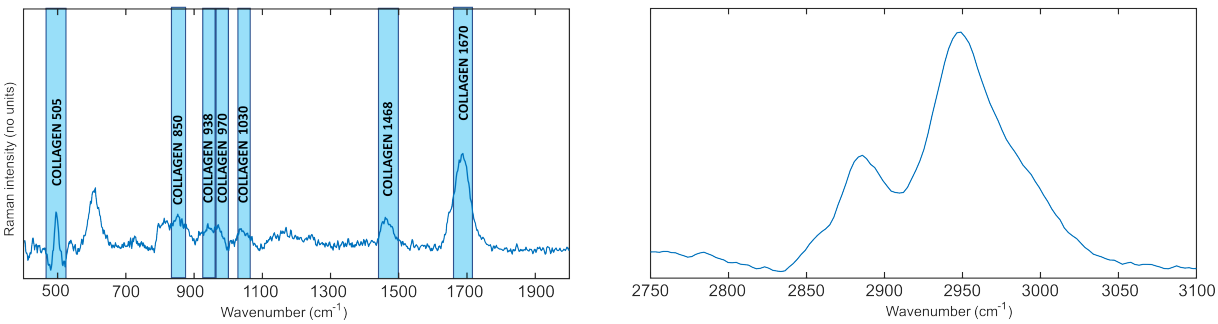

Figure 4.20: The Figure displays the retrieved spectra of collagen, with a focus on highlighting the characteristic peaks specific to collagen.

The close similarity between the obtained spectrum and the known collagen spectrum [102, 106] validates the identification of collagen within the sample using the multimodal microscopy technique employed in this study. This confirms the capability and reliability of our setup in accurately detecting and characterizing collagen-rich regions, offering valuable insights into the structural and biochemical properties of the tissue under investigation.

In summary, this subsection underscores the exceptional capability and performance of our multimodal microscope, which efficiently performs simultaneous BCARS and SHG measurements. The incorporation of SHG detection has proven invaluable, allowing us to retrieve additional chemical and morphological information, including the collagen spectrum and concentration map. This enhancement further amplifies the performance and versatility of our BCARS setup, unlocking possibilities for comprehensive imaging and analysis of complex biological structures.

5 | Conclusions and future developments

In conclusion, this thesis has been dedicated to the exploration and application of coherent anti-Stokes Raman scattering (CARS) as a valuable and powerful imaging technique in the field of Raman microscopy. Additionally, another main goal of this thesis is to make this microscopy technique more powerful. This is done by combining it with second harmonic generation (SHG) microscopy. This combination makes the technique even more useful for advanced microscopic applications.

CARS has demonstrated its potential in overcoming the limitations of other microscopy methods, offering a chemically specific signature that reveals intricate molecular structures without the need for exogenous markers. With respect to standard techniques that employ labels, such as fluorescence microscopy, the system enables avoiding the long preparation time of the sample and the use of markers that often alter the chemical structure or undergo photobleaching, preventing to image of the same region twice. On the other hand, with respect to other label-free techniques, such as SR, it provides higher acquisition speed and does not suffer from sample autofluorescence. These attributes collectively make CARS particularly well-suited for biomedical imaging, providing a non-invasive and label-free approach for the analysis of diverse biological samples, including tissues and cells.

Moreover, the integration of CARS with SHG microscopy paves the way for intrguing advancements in biomedical applications. SHG microscopy stands out as a potent label-free technique, eliminating the need for exogenous dyes or fluorophores, while demonstrating remarkable sensitivity to collagen structures. The deliberate fusion of CARS and SHG microscopy thus highlights an exceptionally promising pathway for investigating intricate biological systems. This synergistic combination leverages the strengths of both methods, providing researchers with a powerful toolkit for the thorough and non-invasive analysis of various biological samples. This, in turn, opens up possibilities for deepening our comprehension of complex biological processes and pathologies.

My thesis began with a thorough introduction to the CARS process and SHG microscopy,

followed by a detailed theoretical description of the main physical processes involved and the derivation of CARS in Chapter 1.
In Chapter 2, the experimental setup used for conducting CARS measurements was presented, consisting of three essential elements: the light source, microscope, and detection system. Notably, the fiber-based Ytterbium pulsed femtosecond laser with wide-ranging output powers, coupled with a YAG crystal for supercontinuum generation, enabled broadband Stokes pulses for efficient CARS excitation. Additionally, the incorporation of a photomultiplier tube (PMT) in the setup allowed for the simultaneous detection of CARS and SHG signals, transforming the system into a multimodal microscope for enhanced imaging capabilities.
Chapter 3 outlined the innovative pipeline adopted for acquiring CARS data and described the post-processing algorithms used to extract relevant chemical information. The denoising procedure based on Singular Value Decomposition (SVD) and the Non-resonant Background (NRB) removal technique using Kramers-Kronig relations were crucial in achieving high-quality, low-noise chemical maps. These sophisticated data processing methods significantly improved the accuracy and reliability of the results obtained.
The final chapter showcased the experimental results that I obtained, demonstrating the system's ability to deliver high-speed (1ms) and high-sensitivity spectroscopy. BCARS spectroscopy was performed on various solvents (acetone, ethanol, methanol, isopropanol, dimethyl sulfoxide (DMSO), and toluene), and the obtained spectra showed excellent agreement with reference spectra obtained from a Spontaneous Raman setup. In continuation, I delved into spectroscopy on subcellular components, namely the Endoplasmic reticulum (ER), cytoplasm, nuclei, lysosomes, mitochondria, and mitochondria-associated membrane (MAM). The obtained spectra from these subcellular components demonstrated remarkable concurrence with SR spectra and also with another BCARS setup at IPHT. This striking consistency of results underscored the repeatability and reliability of our CARS measurements, solidifying the credibility of our findings.
Furthermore, the thesis explored the application of BCARS on different tumor cell lines, specifically HeK293 and HepG2. Through BCARS, I successfully retrieved the average spectrum of individual cells, and by conducting a statistical analysis based on Principal Component Analysis (PCA), I was able to discriminate between different tumor lines based solely on their unique Raman spectra. This highlights the immense potential of CARS in advancing cancer research and diagnostics.
Subsequently, the imaging performance of the setup was demonstrated on biological samples such as NASH liver tissue. Hyperspectral data acquired in a raster-scanning fashion at high acquisition speed enabled the derivation of concentration maps of chemical species, providing valuable chemical information without causing damage to the samples. The

chemical images of control and NASH liver tissue slices, acquired over large fields of view, enabled qualitative comparisons, underscoring the potential of CARS in biomedical imaging for identifying tumors from healthy tissue.

Finally, I present the remarkable upgrade to the setup, which has transformed it into a multimodal microscope with the unique capability to detect both BCARS and SHG signals, further enhancing its performance and versatility. Initially, I acquired the SHG signal by adjusting the central wavelength of the gratings of the spectrometer to differentiate it from the BCARS signal, thus avoiding simultaneous acquisition that hindered fast data collection. Subsequently, I made further improvements to the setup by introducing a photomultiplier tube (PMT), enabling the realization of a true multimodal microscope capable of simultaneously detecting SHG and BCARS signals. This advancement has enabled to achieve high acquisition speed for both signals. Thanks to the incorporation of SHG detection, I retrieved additional chemical and morphological information, including the collagen spectrum and concentration map of collagen in breast tissue containing microcalcifications. These transformative upgrades augmented the capabilities of the system significantly, opening up exciting possibilities for comprehensive imaging and analysis of biological samples. By simultaneously capturing BCARS and SHG signals, the multimodal microscope not only enhances imaging performance but also offers a powerful tool for probing complex tissue structures with high precision and efficiency. The ability to retrieve chemical information, such as collagen concentration in tissues, paves the way for a deeper understanding of tissue microenvironments and disease pathology, making the multimodal microscope a valuable asset in biomedical research and diagnostics.

In conclusion, the demonstrated capabilities of CARS, both independently and in conjunction with SHG, hold immense promise in revolutionizing biomedical imaging and cancer research, offering a label-free and non-invasive approach to exploring the intricate molecular world within living tissues. As CARS technology continues to evolve and gain wider acceptance, it promises to become an indispensable tool for biomedical researchers and clinicians, facilitating a deeper understanding of biological processes and disease mechanisms. Moreover, the pursuit of user-friendly features and potential commercialization will ensure the accessibility and applicability of CARS in clinical settings, making it an invaluable asset for the precise identification and characterization of tumors and other complex biological structures. Also, other future developments of the BCARS setup can be a lot.

As I look towards the future, there are exciting prospects for further development of the CARS setup. Improving acquisition speed through line scanning or wide-field illumination techniques could further elevate the utility of CARS in high-speed imaging applications. Additionally, I envision the further exploitation of multimodal capabilities beyond just

SHG detection, encompassing the detection of two-photon and three-photon excitation fluorescence (TPEF). This extension could open new frontiers for deep-tissue imaging and the study of live biological samples, leveraging ability of TPEF to provide higher resolution and chemical information.

Bibliography

[1] J.B. Pawley. *Handbook of Biological Confocal Microscopy*. Springer, New York, NY, USA, 3rd edition, 2006.

[2] M. Bruchez. *Science*, 281, 1988.

[3] R. Y. Tsien. *Annu. Rev. Biochem.*, 67-509, 1988.

[4] C. Krafft, I. W. Schie, T. Meyer, M. Schmitt, and J. Popp. Developments in spontaneous and coherent raman scattering microscopic imaging for biomedical applications. *Chemical Society Review*, 2016, 1819-1849.

[5] Rohit Bhargava. Infrared spectroscopic imaging: the next generation. *Appl Spectrosc*, 1091-1120, October 2012.

[6] Mahmoud Ghomi. Applications of raman spectroscopy to biology: from basic studies to disease diagnosis. *IOS press*, 2012.

[7] GJ Puppels, FM De Mul, Cornelis Otto, J Greve, M Robert-Nicoud, DJ Arndt-Jovin, and TM Jovin. Studying single living cells and chromosomes by confocal raman microspectroscopy. *Nature*, 1990, 301-303.

[8] G. Turrell and J. Corset. Raman microscopy: Developments and applications. *Academic*, 347, 301, 1990.

[9] N. Stone, C. Kendall, J. Smith, P. Crow, and H. Barr. Faraday discuss. 126, 141, 2004.

[10] U. Neugebauer, T. Bocklitz, J. H. Clement, C. Krafft, and J. Popp. Analyst. 135, 3178, 2010.

[11] D. Polli, V. Kumar, C.M. Valensise, M. Marangoni, and G. Cerullo. Broadband coherent raman scattering microscopy. *Laser Photonics Rev.*, 2018.

[12] G.J. Thomas Jr. *Annu. Rev. Biophys. Biomol. Struct.*, 28, 1, 1999.

[13] S. Sunder, R. Mendelsohn, and H. J. Bernstein. *Chem. Phys. Lipids*, 17, 456, 1976.

[14] H. Yamakoshi, K. Dodo, M. Okada, J. Ando, A. Palonpon, K. Fujita, S. Kawata, and M. Sodeoka. *J. Am. Chem. Soc.*, 133, 6102, 2011.

[15] Nicholas Stone, Catherine Kendall, Jenny Smith, Paul Crow, and Hugh Barr. Faraday discuss. 126,141, 2004.

[16] U. Neugebauer, T. Bocklitz, J. H. Clement, C. Krafft, and J. Popp. Analyst. 135, 3178, 2010.

[17] Conor L Evans and Sunney Xie. Coherent anti-stokes raman scattering microscopy: chemical imaging for biology and medicine. *annual review of analytical chemistry*, 1(1):883, 2008.

[18] Ji-Xin Cheng and Xiaoliang Sunney Xie. Coherent raman scattering microscopy. *Annual Review of Analytical Chemistry*, 2016.

[19] G.L. Eesley. Coherent raman spectroscopy. *Journal of Quantitative Spectroscopy Radiative Transfer*, 22(6):507–576, 1979.

[20] T. H. Maiman. Stimulated optical radiation in ruby. *Nature*, 187(4736):493–494, 1960.

[21] W. Denk and J. H. Strickler. Two-photon laser scanning fluorescence microscopy. *Science*, 248(4951):73–76, April 1990.

[22] Yanping Liand Binglin Shen, Shaowei Li, Yihua Zhao, Junle Qu, and Liwei Liu. Review of stimulated raman scattering microscopy techniques and applications in the biosciences. *Advanced Biology*, 5(1):2000184, 2021.

[23] Christian W. Freudiger, Wei Min, Brian G. Saar, Sijia Lu, G. R. Holtom, Chengwei He, Jason C Tsai, Jing xuan Kang, and X. Sunney Xie. Label-free biomedical imaging with high sensitivity by stimulated raman scattering microscopy. *Science*, 322:1857 – 1861, 2008.

[24] Evelyn Ploetz, Stefan Laimgruber, Stefan Berner, Wolfgang Zinth, and Peter Gilch. Femtosecond stimulated raman microscopy. *Applied Physics B*, 87:389–393, 2007.

[25] P Nandakumar, A Kovalev, and A Volkmer. Vibrational imaging based on stimulated raman scattering microscopy. *New Journal of Physics*, 11(3):033026, 2009.

[26] Kazuki Hashimoto, Megumi Takahashi, Takuro Ideguchi, and Keisuke Goda. Broadband coherent raman spectroscopy running at 24,000 spectra per second. *New Journal of Physics*, 6(1):21036, Feb 2016.

[27] M. D. Duncan, J. Reintjes, and T. J. Manuccia. Scanning coherent anti-stokes raman microscope. *Opt. Lett.*, 7(8):350–352, Aug 1982.

[28] Andreas Zumbusch, Gary R Holtom, and X Sunney Xie. Three-dimensional vibrational imaging by coherent anti-stokes raman scattering. *Physical review letters*, 82(20):4142, 1999.

[29] Paul J. Campagnola and Chen-Yuan Dong. Second harmonic generation microscopy: principles and applications to disease diagnosis. *Laser & Photonics Reviews*, 5(1):13–26, 2011.

[30] Leila Mostaço-Guidolin, Nicole L. Rosin, and Tillie-Louise Hackett. Imaging collagen in scar tissue: Developments in second harmonic generation microscopy for biomedical applications. *Centre for Heart Lung Innovation, University of British Columbia*, 1, 2017.

[31] Clotilde Odin, Thomas Guilbert, and Ahmed et al. Alkilani. Collagen and myosin characterization by orientation field second harmonic microscopy. *Optics Express*, 16:16151–16165, 2008.

[32] Hongying Liu, Tian Lan, Xiaomei Chen, and Guoqiang Ni. Dispersion compensation based on prism compressor. *In Takashige Omatsu, editor, SPIE Proceedings*, April 2017.

[33] H. R. L. Fork, O. E. Martinez, and J. P. Gordon. Negative dispersion using pairs of prisms. *Optics Letters*, May 1984.

[34] Arash Aghigh, Stéphane Bancelin, Maxime Rivard, Maxime Pinsard, Heide Ibrahim, and François Légaré. Second harmonic generation microscopy: a powerful tool for bio-imaging. *Journal of Biological Engineering*, 2022.

[35] Robert M. Williams, Warren R. Zipfel, and Watt W. Webb. Multiphoton microscopy in biological research. *Current Opinion in Chemical Biology*, 5:603–608, 2001.

[36] Richard G. Reish and E. Eriksson. Scars: A review of emerging and currently available therapies. *Plastic and Reconstructive Surgery*, 122:1068–1078, 2008.

[37] Chandan K. Sen, Gayle M. Gordillo, Sashwati Roy, Robert Kirsner, Lynn Lambert, Thomas K. Hunt, Finn Gottrup, Geoffrey C. Gurtner, and Michael T. Longaker. Human skin wounds: A major and snowballing threat to public health and the economy. *Wound Repair and Regeneration*, 17:763–771, 2009.

[38] Xiaoyun Chen, Oleg Nadiarynkh, Sergey Plotnikov, and Paul J. Campagnola. Sec-

ond harmonic generation microscopy for quantitative analysis of collagen fibrillar structure. *Nature Protocols*, 7:654–669, 2012.

[39] Guy Cox. Biological applications of second harmonic imaging. *Biophysical Reviews*, 3:131, 2011.

[40] Paul J. Campagnola, Andrew C. Millard, and Mark et al. Terasaki. Three-dimensional high-resolution second-harmonic generation imaging of endogenous structural proteins in biological tissues. *Biophysical Journal*, 82:493–508, 2002.

[41] Guy Cox, Eleanor Kable, and Andrew et al. Jones. 3-dimensional imaging of collagen using second harmonic generation. *Journal of Structural Biology*, 141:53–62, 2003.

[42] Edward E. Hoover and Jeff A. Squier. Advances in multiphoton microscopy technology. *Nature Photonics*, 7:93–101, 2013.

[43] William Mohler, Andrew C. Millard, and Paul J. Campagnola. Second harmonic generation imaging of endogenous structural proteins. *Methods*, 29:97–109, 2003.

[44] Ivan Gusachenko, Vinh Tran, and Yasmine G. et al. Houssen. Polarization-resolved second-harmonic generation in tendon upon mechanical stretching. *Biophysical Journal*, 102:2220–2229, 2012.

[45] Ahmad et al. Golaraei. Polarimetric second-harmonic generation microscopy of the hierarchical structure of collagen in stage i-iii non-small cell lung carcinoma. *Biomedical Optics Express*, 11:1851–1863, 2020.

[46] Hervé Rigneault. Chapter 1 - coherent raman scattering processes. *Stimulated Raman Scattering Microscopy*, page 3–20, 2022.

[47] Jennifer P. Ogilvie, Meng Cui, Dmitry Pestov, Alexei V. Sokolov, and Marlan O. Scully. Time-delayed coherent raman spectroscopy. *Molecular Physics*, 106(2-4):587–594, 2008.

[48] Ji-Xin Cheng, Lewis D. Book, and X. Sunney Xie. Polarization coherent anti-stokes raman scattering microscopy. *Optics Letters*, 26(17):1341, Sep 2001.

[49] Andreas Volkmer, Lewis D. Book, and X. Sunney Xie. Time-resolved coherent anti-stokes raman scattering microscopy: Imaging based on raman free induction decay. *Applied Physics Letters*, 80(9):1505–1507, 2002.

[50] Paul J. Wrzesinski, Hans U. Stauffer, Waruna D. Kulatilaka, James R. Gord, and Sukesh Roy. Time-resolved femtosecond CARS from 10 to 50 bar: Collisional sensitivity. *Journal of Raman Spectroscopy*, 44(10):1344–1348, Mar 2013.

[51] Miu Tamamitsu, Yusuke Sakaki, Tasuku Nakamura, G. Krishna Podagatlapalli, Takuro Ideguchi, and Keisuke Goda. Ultrafast broadband fourier-transform CARS spectroscopy at 50,000 spectra/s enabled by a scanning fourier-domain delay line. *Vibrational Spectroscopy*, 91:163–169, Jul 2017.

[52] Kazuki Hashimoto, Megumi Takahashi, Takuro Ideguchi, and Keisuke Goda. Broadband coherent raman spectroscopy running at 24,000 spectra per second. *Scientific Reports*, 6(1):21036, Feb 2016.

[53] Marcus T. Cicerone, Khaled A. Aamer, Young Jong Lee, and Erik Vartiainen. Maximum entropy and time-domain kramers-kronig phase retrieval approaches are functionally equivalent for CARS microspectroscopy. *Journal of Raman Spectroscopy*, 43(5):637–643, Apr 2012.

[54] Erik M. Vartiainen, Hilde A. Rinia, Michiel Müller, and Mischa Bonn. Direct extraction of raman line-shapes from congested CARS spectra. *Optics Express*, 14(8):3622–3630, 2006.

[55] C. M. Valensise, A. Giuseppi, F. Vernuccio, A. De la Cadena, G. Cerullo, and D. Polli. Removing nonresonant background from CARS spectra via deep learning. *APL Photonics*, 5(6):061305, Jun 2020.

[56] Rola Houhou, Parijat Barman, Micheal Schmitt, Tobias Meyer, Juergen Popp, and Thomas Bocklitz. Deep learning as phase retrieval tool for CARS spectra. *Optics Express*, 28(14):21002, Jul 2020.

[57] Zhengwei Wang, Kevin O'Dwyer, Ryan Muddiman, Tomas Ward, Charles H. Camp, and Bryan M. Hennelly. Very deep convolutional autoencoders for non-resonant background removal in broadband coherent anti-stokes raman scattering. *Journal of Raman Spectroscopy*, 53(6):1081–1093, Mar 2022.

[58] Miloš Miljkovic, Tatyana Chernenko, Melissa J. Romeo, Benjamin Bird, Christian Matthäus, and Max Diem. Label-free imaging of human cells: Algorithms for image reconstruction of raman hyperspectral datasets. *The Analyst*, 135(8):2002, 2010.

[59] Brian G. Saar, Christian W. Freudiger, Jay Reichman, Christine M. Stanley, Gary R. Holtom, and X. Sunney Xie. Video-rate molecular imaging in vivo with stimulated raman scattering. *Science*, 330:1368, 2010.

[60] Thomas Hellerer, Annika M. K. Enejder, and Andreas Zumbusch. Characterization of the nonresonant background in coherent anti-stokes raman scattering. *Applied Physics Letters*, 85(25):25, 2004.

[61] Andreas Volkmer, Lewis D. Book, and X. Sunney Xie. Femtosecond coherent anti-stokes raman scattering microscopy. *Applied Physics Letters*, 80(9):1505, 2002.

[62] N. Dudovich, D. Oron, and Y. Silberberg. Femtosecond resonant coherent anti-stokes raman scattering in solution. *Nature*, 418:512, 2002.

[63] Keisuke Isobe, Akira Suda, Masahiro Tanaka, Hiroshi Hashimoto, Fumihiko Kannari, Hiroyuki Kawano, Hideaki Mizuno, Atsushi Miyawaki, and Katsumi Midorikawa. Single-pulse coherent anti-stokes raman scattering microscopy employing an octave spanning pulse. *Opt. Express*, 17(14):11259–11266, 2009.

[64] Wolfgang Langbein, Israel Rocha-Mendoza, and Paola Borri. Single source coherent anti-stokes raman microspectroscopy using spectral focusing. *Applied Physics Letters*, 95(8):081109, 2009.

[65] Tak W. Kee and Marcus T. Cicerone. Simple approach to one-laser, broadband coherent anti-stokes raman scattering microscopy. *Opt. Lett.*, 29(23):2701–2703, 2004.

[66] Jingjiang Xu, Baoshan Guo, Kenneth K. Y. Wong, and Kevin K. Tsia. Broadband hyperspectral coherent anti-stokes raman scattering microscopy for stain-free histological imaging with principal component analysis. In *Multiphoton Microscopy in the Biomedical Sciences XIV*, volume 8948, page 89480R. International Society for Optics and Photonics, 2014.

[67] Takuro Ideguchi, Simon Holzner, Birgitta Bernhardt, Guy Guelachvili, Nathalie Picqué, and Theodor W. Hänsch. Coherent raman spectro-imaging with laser frequency combs. *Nature*, 502(7471):355–358, 2013.

[68] Kazuki Hashimoto, Megumi Takahashi, Takuro Ideguchi, and Keisuke Goda. Broadband coherent raman spectroscopy running at 24,000 spectra per second. *Scientific Reports*, 6(1):21036, 2016.

[69] Miu Tamamitsu, Yusuke Sakaki, Tasuku Nakamura, G. Krishna Podagatlapalli, Takuro Ideguchi, and Keisuke Goda. Ultrafast broadband fourier-transform CARS spectroscopy at 50,000 spectra/s enabled by a scanning fourier-domain delay line. *Vibrational Spectroscopy*, 91:163–169, 2017.

[70] Charles H. Camp Jr, Young Jong Lee, John M. Heddleston, Christopher M. Hartshorn, Angela R. Hight Walker, Jeremy N. Rich, Justin D. Lathia, and Marcus T. Cicerone. High-speed coherent raman fingerprint imaging of biological tissues. *Nature Photonics*, 8(8):627–634, Aug 2014.

[71] Hiroaki Yoneyama, Kazuhiro Sudo, Philippe Leproux, Vincent Couderc, Akihito Inoko, and Hideaki Kano. CARS molecular fingerprinting using sub-100-ps microchip laser source with fiber amplifier. *APL Photonics*, 3(9):092408, 2018.

[72] F. Vernuccio, R. Vanna, C. Ceconello, A. Bresci, F. Manetti, S. Sorrentino, S. Ghislanzoni, F. Lambertucci, O. Motiño, I. Martins, G. Kroemer, I. Bongarzone, G. Cerullo, and D. Polli. Full-spectrum CARS microscopy of cells and tissues with ultrashort white-light continuum pulses. *J. Phys. Chem. B*, 127:4733–4745, 2023.

[73] F. Vernuccio, A. Bresci, B. Talone, A. de la Cadena, C. Ceconello, S. Mantero, C. Sobacchi, R. Vanna, G. Cerullo, and D. Polli. Fingerprint multiplex CARS at high speed based on supercontinuum generation in bulk media and deep learning spectral denoising. *Optics Express*, 30(17):30135, August 2022.

[74] Ji-Xin Cheng, Andreas Volkmer, Lewis D. Book, and X. Sunney Xie. An epi-detected coherent anti-stokes raman scattering (e-CARS) microscope with high spectral resolution and high sensitivity. *The Journal of Physical Chemistry B*, 105(7):1277–1280, February 2001.

[75] Charles H Camp, Young Jong Lee, and Marcus T Cicerone. Quantitative, comparable coherent anti-stokes raman scattering (CARS) spectroscopy: correcting errors in phase retrieval. *J Raman Spectrosc*, 47(4):408–415, October 2015.

[76] MT Cicerone, YJ Lee, SH Parekh, and KA Aamer. Photonic crystal fiber-based broadband CARS microscopy. In Ji-Xin Cheng and X Sunney Xie, editors, *Coherent Raman Scattering Microscopy*, chapter 15, pages 329–352. CRC Press, Boca Raton, FL, 2012.

[77] M Makitalo and A Foi. Optimal inversion of the anscombe transformation in low-count poisson image denoising. *IEEE Trans Image Process*, 20(1):99–109, January 2011.

[78] Charles H Camp Jr, John S Bender, and Young Jong Lee. Real-time and high-throughput raman signal extraction and processing in CARS hyperspectral imaging. *Opt Express*, 28(14):20422, June 2020.

[79] Charles H Camp Jr, Young Jong Lee, John M Heddleston, Christopher M Hartshorn, Angela R Hight Walker, Jeremy N Rich, Justin D Lathia, and Marcus T Cicerone. High-speed coherent raman fingerprint imaging of biological tissues. *Nat Photonics*, 8:627–634, 2014.

[80] Young Jong Lee, Daesung Moon, Kalman B Migler, and Marcus T Cicerone. Quan-

titative image analysis of broadband CARS hyperspectral images of polymer blends. *Anal Chem*, 83:2733–2739, 2011.

[81] Erik M Vartiainen. Phase retrieval approach for coherent anti-stokes raman scattering spectrum analysis. *J Opt Soc Am B*, 9:1209–1214, 1992.

[82] Yong Liu, Young Jong Lee, and Marcus T Cicerone. Broadband CARS spectral phase retrieval using a time-domain kramers-kronig transform. *Opt Lett*, 34:1363–1365, 2009.

[83] Marcus T Cicerone, Khalid A Aamer, Young Jong Lee, and Erik M Vartiainen. Maximum entropy and time-domain kramers-kronig phase retrieval approaches are functionally equivalent for CARS microspectroscopy. *J Raman Spectrosc*, 43:637–643, 2012.

[84] Young Jong Lee, Daesung Moon, Kalman B Migler, and Marcus T Cicerone. Quantitative image analysis of broadband CARS hyperspectral images of polymer blends. *Anal Chem*, 83:2733–2739, 2011.

[85] Tommaso Baldacchini, Mateusz Zimmerley, Chia-Hua Kuo, Eric O Potma, and Ruben Zadoyan. Characterization of microstructures fabricated by two-photon polymerization using coherent anti-stokes raman scattering microscopy. *J Phys Chem B*, 113:12663–12668, 2009.

[86] H A Rinia, Mischa Bonn, Martina Muller, and Erik M Vartiainen. Quantitative CARS spectroscopy using the maximum entropy method: the main lipid phase transition. *Chemphyschem*, 8:279–287, 2007.

[87] Sapun H Parekh, Young Jong Lee, Khalid A Aamer, and Marcus T Cicerone. Label-free cellular imaging by broadband coherent anti-stokes raman scattering microscopy. *Biophys J*, 99:2695–2704, 2010.

[88] WM Tolles, JW Nibler, JR Mcdonald, and AB Harvey. A review of the theory and application of coherent anti-stokes raman spectroscopy (CARS). *Appl Spectrosc*, 31:253–271, 1977.

[89] I. T. Jolliffe and C. Jorge. Principal component analysis: A review and recent developments. *Philosophical Trans. R. Soc. A Math. Phys. Eng. Sci.*, 374 (2065), 2016.

[90] Rasmus Bro and Age K. Smilde. Principal component analysis. *Analytical Methods*, 6(9):2812–2831, 2014.

[91] Michael E. Winter. A proof of the n-findr algorithm for the automated detection of endmembers in a hyperspectral image. *In Sylvia S. Shen and Paul E. Lewis, editors, SPIE Proceedings.*, August 2004.

[92] Ya-Juan Liu, Michelle Kyne, Cheng Wang, and Xi-Yong Yu. Data mining in raman imaging in a cellular biological system. *Computational and Structural Biotechnology Journal*, 18:2920–2930, 2020.

[93] Miloš Miljkovic, Tatyana Chernenko, Melissa J. Romeo, Benjamin Bird, Christian Matthäus, and Max Diem. Label-free imaging of human cells: algorithms for image reconstruction of raman hyperspectral datasets. *The Analyst*, 135(8):2002, 2010.

[94] Oliver F. W. James and Christopher P. Day. Non-alcoholic steatohepatitis (nash): A disease of emerging identity and importance. *Journal of Hepatology*, 29:495–501, 1998.

[95] Abdul M. Oseini and Arun J. Sanyal. Therapies in non-alcoholic steatohepatitis (nash). *Liver International*, 37(Suppl 1):97–103, 2017.

[96] Águeda González-Rodríguez, Rafael Mayoral, Noelia Agra, M Pilar Valdecantos, Virginia Pardo, María Eugenia Miquilena-Colina, Javier Vargas-Castrillón, Olga Lo Iacono, Marco Corazzari, Gian Maria Fimia, et al. Impaired autophagic flux is associated with increased endoplasmic reticulum stress during the development of nafld. *Cell Death & Disease*, 5(4):e1179, 2014.

[97] Zobair M. Younossi, Sandra Page, Nila Rafiq, Aybike Birerdinc, Maria Stepanova, Noreen Hossain, Arian Afendy, Zahra Younoszai, Zachary Goodman, and Ancha Baranova. A biomarker panel for non-alcoholic steatohepatitis (nash) and nash-related fibrosis. *Obesity Surgery*, 21(3):431–439, 2011.

[98] Emel Ahishali, Kadir Demir, Bulent Ahishali, Filiz Akyuz, Binnur Pinarbasi, Sule Poturoglu, Duygu Ibrisim, Mine Gulluoglu, Sadakat Ozdil, Fatih Besisik, and Sabahattin Kaymakoglu. Electron microscopic findings in non-alcoholic fatty liver disease: Is there a difference between hepatosteatosis and steatohepatitis? *Journal of Gastroenterology and Hepatology*, 25(4):794–801, 2010.

[99] Mark Bydder, Taylor Chavez, Jennifer Lam, William Henderson, Nicole Pinto, Rebeca Chavarria, Albert D Pham, Rohit Loomba, Jeffrey Schwimmer, Claude Sirlin, and Gavin Hamilton. Triglyceride saturation in patients at risk of nash and nafld: A cross-sectional study. *Biophysica*, 2(1):8–15, 2021.

[100] Yuichiro Kawano and David E Cohen. Mechanisms of hepatic triglyceride accumula-

tion in non-alcoholic fatty liver disease. *Journal of gastroenterology*, 48(4):434–441, 2013.

[101] Benoit Rivière, Audrey Jaussent, Violaine Macioce, Sylvaine Faure, Nicolas Builles, Pierre Lefebvre, Pierre Géraud, Marie-Christine Picot, Stéphane Rebuffat, Eric Renard, Valérie Paradis, Marie-Dominique Servais, Nicolas de Préville, David Nocca, Anne-Dominique Lajoix, Georges-Philippe Pageaux, and Florence Galtier. The triglycerides and glucose (tyg) index: A new marker associated with nonalcoholic steatohepatitis (nash) in obese patients. *Diabetes & metabolism*, 48(4):101345, 2022.

[102] Ivana Semova and Sudha Bhattacharya Biddinger. Triglycerides in nonalcoholic fatty liver disease: Guilty until proven innocent. *Trends in pharmacological sciences*, 42(3):183–190, 2021.

[103] Barbara S. Monsees. Evaluation of breast microcalcifications. *Radiologic Clinics of North America*, 33(6):1109–1121, November 1995.

[104] Woo Kyung Moon, Jung-Gi Im, Young Hwan Koh, Dong-Young Noh, and In Ae Park. Us of mammographically detected clustered microcalcifications. *Radiology*, 217(3), December 2000.

[105] Georgi I. Petrov, Rajan Arora, and Vladoslav V. Yakovlev. Coherent anti-stokes raman scattering imaging of microcalcifications associated with breast cancer. *Analyst*, (4), 2021.

[106] Marcus Cicerone. Molecular imaging with CARS micro-spectroscopy. *Current Opinion in Chemical Biology*, 34:165–170, 2016.

[107] Hanglin Ye, Rahul, Uwe Kruger, Tianmeng Wang, Sufei Shi, Jack Norfeet, and Suvranu De. Burn-related collagen conformational changes in ex vivo porcine skin using raman spectroscopy. *Scientific Reports*, 9(1):19138, 2019.

A | The SRS process

The SRS is another technique that utilizes the third-order non-linearity phenomenon by resonantly exciting the Raman transition at frequency Ω with two synchronized trains of laser pulses at frequency ω_s (Stokes) and ω_p (pump). When these two laser beams interact coherently with the sample, they result in stimulated emission from a virtual state to the vibrational state of interest. This leads to the amplification of the Stokes beam intensity (known as Stimulated Raman Gain or SRG) and a simultaneous reduction of the pump beam intensity (Stimulated Raman Loss or SRL). Figure A.1 illustrates the SRS process.

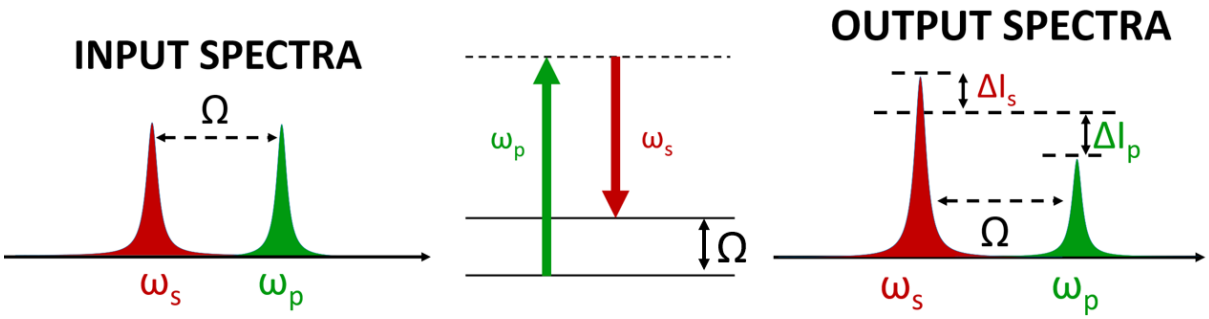

Figure A.1: Jablonsky diagram of the SRS process and the representation of the Stokes and Pump pulses before and after the SRS process.

In order to measure small signals on top of a large background and achieve high sensitivity in SRS measurements, a modulation transfer technique is necessary. To achieve this, detection with a lock-in is employed. This technique involves modulating the signal at high frequencies greater than 1 MHz. By modulating the signal in this way, consecutive laser pulses that generate a signal on top of the background will be highly correlated. This is because the laser does not have enough time to change significantly between the two pulses, resulting in a noise that is very similar. By using lock-in detection, it is possible to observe the changes induced by the signal rather than the noise. Specifically, the pump can be modulated and the gain in the Stokes beam can be measured, or the Stokes beam can be modulated and the pump loss can be measured. This modulation

transfer technique allows for accurate measurement of small signals in the presence of a large background, enabling high-sensitivity SRS measurements.
Starting from equation (1.137), we can obtain the mathematical expression for the amplitude of SRG and SRL using a four-wave mixing approach. To do this, we impose $\omega_1 = \omega_4 = \omega_p$ and $\omega_2 = \omega_3 = \omega_s$, taking into account that $\omega_1 - \omega_2 + \omega_3 = \omega_4$ and the resonant condition is $\omega_1 - \omega_2 = \Omega$. It is worth noting that the SRS process is always phase-matched because $\Delta k = k_p - k_p + k_s - k_s = 0$.
Thus, equation (1.137) can be simplified to:

$$\begin{cases} \dfrac{\partial A_p}{\partial z} = -i\alpha_p \chi^{(3)} |A_s|^2 A_p & \text{(A.1a)} \\ \dfrac{\partial A_s}{\partial z} = -i\alpha_s \chi^{(3)} |A_p|^2 A_s & \text{(A.1b)} \end{cases}$$

Next, let's consider the SRL signal and assume small signals, which implies no depletion of the pump (or Stokes) for SRL (or SRG). Therefore, equation (A.1a) can be integrated over the distance as follows:

$$A_p(L) = A_p(0) e^{-i\alpha_p \chi^{(3)} |A_s|^2 L} \tag{A.2}$$

In the case of small signals, we can expand the exponential function using the Taylor series:

$$A_p(L) \approx A_p(0) - iA_p(0)\alpha_p \chi^{(3)} |A_s|^2 L \tag{A.3}$$

We can define the quantity $\Delta A_p \triangleq A_p(0)\alpha_p \chi^{(3)} |A_s|^2 L$. The intensity, that we measure at the detector, is:

$$I_p(L) \propto |A_p(L)|^2 = |A_p(0)|^2 - |\Delta A_p|^2 + 2\mathbb{R}e\Big[A_p^*(0)\Delta A_p\Big] \tag{A.4}$$

Under the assumption of small signal the second term $|\Delta A_p|^2$ can be negleted since $|\Delta A_p| << |A_p(0)|$. So the intensity of the pump at the detector is:

$$I_p(L) \propto |A_p(L)|^2 = |A_p(0)|^2 + 2\mathbb{R}e\Big[A_p^*(0)\Delta A_p\Big] \tag{A.5}$$

Then, we finally get:

$$I_p(L) \propto |A_p(L)|^2 = |A_p(0)|^2 + 2\mathbb{R}e\Big[\alpha_p \chi_R^{(3)} |A_s|^2 |A_p(0)|^2 L\Big] \tag{A.6}$$

The first term on the right-hand side represents the intensity of the pump beam, which we assume to be virtually unattenuated during the nonlinear process. The second term

represents the interference between the incident Stokes field and the stimulated Raman field at the detector. If $\chi^{(3)}$ is purely real, the interference term disappears. However, close to resonance, $\mathbb{R}e\left\{\chi_R^{(3)}\right\} \neq 0$ and the interference term is non-vanishing. To isolate this interference term from the other terms, modulation transfer techniques are used. One beam is modulated at a high frequency (>1 MHz, where laser noise reaches its minimum values), and the modulation transfer on the other beam is detected using a lock-in amplifier that essentially demodulates the signal acquired with a photodiode. In an SRL experiment, the detected quantity is the change in intensity of the pump beam when the Stokes beam is modulated:

$$\Delta I_p = I_p(L) - I_p(0) \approx \mathbb{I}m\left\{\alpha_p \chi_R^{(3)} |A_p(0)|^2 |A_s|^2 L\right\} \tag{A.7}$$

SRL is finally:

$$SRL = \frac{\Delta I_p}{I_p(0)} = \alpha_p I_s L \mathbb{I}m\left\{\chi_R^{(3)}\right\} \tag{A.8}$$

To obtain the SRG signal, one can follow the same procedure as for the SRL signal:

$$SRG = \frac{\Delta I_s}{I_s(0)} = \alpha_s I_p L \mathbb{I}m\left\{\chi_R^{(3)}\right\} \tag{A.9}$$

From the equations above we can identify some characteristics of the SRS process:

- The SRS process is inherently phase-matched.
- The measured signal is directly related to the imaginary part of $\chi_R^{(3)}$, and as a result, the non-resonant background (NRB) is effectively suppressed. This means that the measurement is not affected by any dispersion of the lineshape, and only the resonant part of the signal is detected.
- Since As $\chi_R^{(3)}$ is proportional to the number of oscillators N in the focal volume, the signal generated by the SRG technique scales linearly with the number of oscillators. Therefore, this method is capable of detecting species that are present in smaller quantities.
- The process exhibits self-heterodyne amplification as the small signal, ΔI_s, is amplified by the stokes intensity, I_s.
- To detect the small signal ΔI_s generated by SRS, modulation and demodulation techniques are necessary along with lock-in detection. This is because the signal is buried under a high background I_s (stokes itself) and modulation at a high frequency (>1 MHz) helps to isolate the signal from the noise and the background. The

modulated signal is then detected using a lock-in amplifier which demodulates the signal and enhances the sensitivity of the measurement.

List of Figures